MAPPING THE EVOLUTION OF POROSITY IN SINTERED COPPER TO ENABLE THE NUMERICAL SIMULATION OF SINTERING

A Thesis

by

YESENIA SALAZAR

Submitted to the Graduate and Professional School of
Texas A&M University
in partial fulfillment of the requirements for the degree of

MASTER OF SCIENCE

Chair of Committee,	Sean M. McDeavitt
Committee Members,	Delia Perez-Nunez
	Patrick J. Shamberger
Head of Department,	Michael Nastasi

December 2021

Major Subject: Nuclear Engineering

ABSTRACT

The sintering evolution of copper spheres was characterized as part of a larger project with the objective to numerically simulate the sintering of uranium and its alloys to enable the development of sintering models. The larger project is a multi-task activity supported by the U.S. Department of Energy Office of Nuclear Energy where individual tasks included 1) the numerical simulation of sintering in uranium, 2) fundamental atomistic modeling of uranium-zirconium alloys, 3) mapping the actual porosity evolution in sintered uranium-10 wt.% zirconium alloys, and 4) mapping the actual porosity evolution in sintered copper powder pellets. The sintering of copper is a well understood phenomenon, relevant for this project due to its relative metallurgical simplicity as an intermediate modeling challenge. Uranium and U-10Zr exhibit multiple complex phase structures that complicate the ultimate objectives of atomistic and phase field modeling that must eventually be mastered. On the path toward that mastery, copper represents a simple, single-phase face-centered cubic (FCC) structure with a melting point like that of metallic uranium. The high temperature phases for U and U-10Zr are body-centered cubic (BCC), which make this material more challenging to cut and polish for porosity analysis. For this reason, Cu powder was used to prepare microstructure data for mapping porosity evolution during sintering and provide a simpler validation point for numerical simulations of the porosity evolution in two-phase U-10Zr.

The work presented here describes the experimental methods developed for the generation of sintered, porous copper metal pellets and the volumetric porosity distribution for set temperature. This involved the evaluation and determination of production parameters for palletization such as pressure, lubrication, sintering temperature, and dwell time. An initial series of sintering tests were performed to establish pressing and sintering parameters; sintering of

pressed pellets and packed powder-bed pellets was evaluated. Eventually, a systematic set of samples was created by sintering samples at 1065°C. The sintered pellets were characterized to map the evolution of density and porosity during sintering. a porosity gradient formed within the pellet. The sintered structures exhibited a 2-region characteristic where the outer region exhibited minimal densification with some with particle bonding while the interior region exhibited high levels of densification. The evolution of this two-region structure was evaluated.

DEDICATION

I dedicate this work to everyone that continuously showed interest in the progress of my studies, and to anyone that majoring in math who is wondering if nuclear engineering is a possible path in their career.

ACKNOWLEDGEMENTS

The completion of this work could not have been accomplished without some of the best advisors and mentors that TAMU had to offer. Dr. Mcdeavitt, Dr. Perez-Nunez and Dr. Ortega who never hesitated to answer my questions, guide me through concepts that were new to me, listen to my draft thesis presentations, and have an incredible amount of patience to see me accomplish my academic goals, despite several setbacks. The NUEN department and staff who assisted me in the initial stages of applying to a summer internship a year prior to being admitted as a grad student, and later guided me through grad courses. My acknowledgements go out to Dr. Shamberger as well who as a member of my committee has helped me understand a higher scope of my results outside of the nuclear topic. And all the friends I got to make through coursework and laboratory interactions, who really helped understand that we all come across similar struggles as graduate students and it has been amazing seeing all of them flourish in their careers and personal lives.

This work could only be completed as well thanks to my family who always respected my academic decisions and supported me in any way they could without hesitation, especially my parents, Artemio, and Maria, and brother, Oziel. And to my friends outside of the nuclear realm of academics who never diminished their efforts to root me on through the years. Thank you all for every piece of advice, for listening when I just wanted to vent, and for helping me hold my head up high when it seemed too draining to do so.

CONTRIBUTORS AND FUNDING SOURCES

This work was supported by a thesis committee consisting of Professor Sean M. McDeavitt [advisor] and Delia Perez-Nunez of the Department of Nuclear Engineering, and Professor Patrick J. Shamberger of the Department of Materials Science and Engineering.

The data depicted in Chapter 2, Section 2 was conducted and provided by Cliff Hart of the Department of Nuclear Engineering and was published in 2019 in thesis format. The data depicted in Chapter 2, Section 3 was conducted and provided by Bruce Barry of the Department of Mechanical Engineering from the University of Arkansas and was published in 2017 in thesis format.

All other work conducted for the thesis was completed by the student independently.

This Graduate study was partially supported by Texas A&M University and DOE-NE Nuclear Energy University Programs (NEUP), Project NO. 14-6472.

NOMENCLATURE

A	Area
AIMD	Archimedes' Immersion Method Density
BCC	Body Centered Cubic
Cu	Copper
D	Density
DCR	Dense Center Region
FCC	Face Centered Cubic
GGD	Geometric Green Density
HCP	Hexagonal Close Packing
P	Porosity
Mo	Molybdenum
MOOSE	Multiphysics Object Oriented Simulation Environment
MPa	Megapascal
OC-S	Overall Cross-Section
PR	Porous Rim
SGD	Sintered Geometric Density
SEM	Scanning Electron Microscope
Ta	Tantalum
T.D.	Theoretical Density
U-10Zr	90% by weight Uranium with 10% by weight Zirconium
$\chi(\%)$	Percentage Ratio of Small Pores to Total Amount of Pores

TABLE OF CONTENTS

Page

LIST OF FIGURES

Page

LIST OF TABLES

CHAPTER 1

INTRODUCTION

The sintering behavior of pelletized spherical copper was characterized as part of a larger project with the objective to numerically simulate the sintering of uranium and its alloys to enable the development of sintering models. The overall project is composed of experimental multi-task components supported by the U.S. Department of Energy Office of Nuclear Energy where individual tasks included 1) the numerical simulation of sintering in uranium [11]; 2) fundamental atomistic modeling of uranium-zirconium alloys [30]; 3) mapping the actual porosity evolution in sintered uranium-10 wt.% zirconium alloys (U-10Zr) [20]; and 4) mapping the actual porosity evolution in sintered copper. The sintering of copper is an established phenomenon, but it is relevant for this project due to its relative metallurgical simplicity as an intermediate modeling challenge. Uranium and U-10Zr exhibit multiple complex phase structures that complicate the ultimate objectives of atomistic and phase field modeling that must eventually be mastered. On the path toward that mastery, copper represents a simple, single-phase face-centered cubic (FCC) structure with a similar melting point to metallic uranium; the high temperature γ phases for U and U-10Zr are FCC as well.

As nuclear fuel is burned to produce energy, the fundamental materials structure is altered by the transformation of uranium atoms into fission products, which is accompanied by significant microstructural damage as the fission products impact the microstructure, produce cascades of damage, induce recombination, precipitation, and lattice disruptions that affect the properties of the fuel. One important phenomenon that emerges in the midst of this extreme environment is the evolution of fission-gas filled porosity and swelling of the fuel structure. As fission progresses over time, swelling induces the interconnection of gas-filled bubbles, releasing the fission gas and

reducing the internal pressure in the remnant porosity. The remnant porosity without internal gas pressure proceeds to resinter and there is a need to develop model for fuel performance simulations that predict nuclear fuel behavior as burnup proceeds.

Burnup is a term used to define the rate of fuel atoms are used, or burned, in the reactor to produce energy [4, 6]. Burnup is denoted in units of gigawatt-days (accumulated power produced times the effective "days" in the reactor) per metric ton of initial fuel, in most cases being Uranium (GWd/MTU). With higher burnup values, the fuel becomes more efficient since more power is generated from the same amount of fuel [22]. Since the first reactor built in 1942, reactor fuel and components have been improved to obtain higher burnup values. From 1970 to 2005 nearly all types of reactors had increased their burnup values by at least a factor of 2 GWd/MTU (Fig. 1), except for Magnox and WWER reactors which remained relatively constant in burnup values along the time lapse of 35 years as these were not altered but replaced by new types of reactors. Most of the information in Figure 1 from commercial reactors represents the performance of oxide nuclear fuel. Fission gas swelling, gas release, and resintering has been evaluated by other researchers [2, 7, 26, 27, 26, 28]. Alloy nuclear fuels are emerging as candidates for fast reactors with much higher burnup goals and less performance data available.

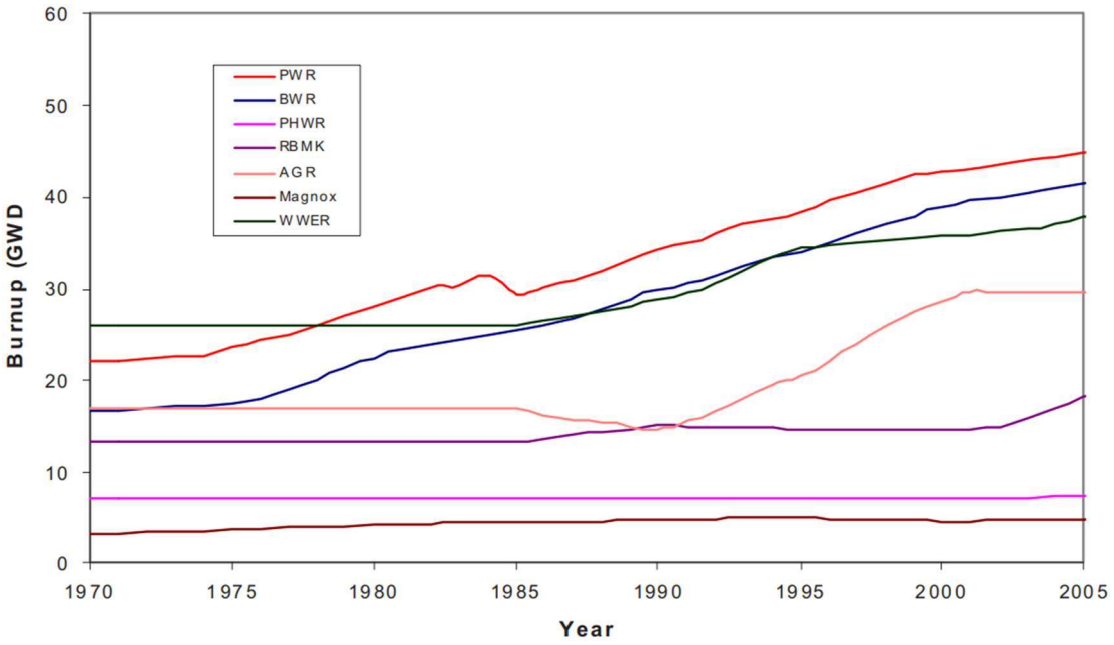

Figure 1: Fuel burnup trends for reactors from 1970 to 2005 [1].

Increasing fuel burnup is accomplished by including a higher content of fissile atoms (e.g., U-235) in the initial fuel. The extended reactor residence time and higher production of fission products increase the impact performance-limiting behaviors such as swelling, gas release, and resintering even as the extended burnup improves energy production efficiency. For commercial oxide-fueled reactors, burnups tend to be on the order of 50 to 55 GWd/MTU, but metal fueled fast reactors are seeking burnup achievements 4 to 10 times higher than that, exacerbating the performance limiting behavior and obviating the need for high-fidelity modeling and performance data. Fuel is normally removed from a reactor after a combination of parameters are exceeded within a fuel loading: 1) the initial U-235 content is depleted, 2) fission products accumulation (such as fission gases) causes fuel performance and reactivity challenges, and 3) non-fuel structural materials reach performance limiting thresholds. Fission products are produced during fission chain reactions and accumulate over time.

It is in this context that the sintering of copper is being used as a surrogate for uranium alloys. The performance limitations introduced by fission gas swelling, gas release and resintering

in metal fuel are being modeled by others [28]. The modeling of these phenomena in oxide nuclear fuel is relatively mature and the context of oxide fuel swelling is typically confined to relatively low burnup [1]. However, metallic fuel alloys such as U-10Zr are being developed for very high burnup where the swelling-to-resintering scenario plays a critical role in fuel performance. Therefore, an effective model for the restructuring of metal fuel porosity during operation is the chief objective and the experiments performed with copper are useful for simplifying the model system to validate methods before considering U-10Zr structures. Copper exists as a single-phase FCC metal that melts at ~1085°C, depending on copper purity [5]. The U-10Zr alloy may exist in multiple phase structures from the low temperature $\alpha+\delta$ phase to the high temperature γ phase [20]. The $\alpha+\delta$ phase has a dual-structured phase boundary where the α phase is orthorhombic and the δ phase is hexagonal whereas the γ phase has a single-phase FCC structure like copper. The point here is that the sintered copper structures prepared here may be used as a simplified baseline structure for modeling γ phase U-10Zr.

The remaining content of this thesis is experiment-driven and exclusively focused on the sintering of copper metal. The goal was to prepare porous copper samples using common processing conditions and to quantify the evolution of the volumetric porosity distribution and pore morphologies as a function of time. At the onset, various sample production parameters for were considered such as pressure, lubrication, sintering temperature and dwell time. An initial series of tests were performed under varying processing methods to establish the final pressing and sintering parameters [29, 31]. The sintered result of pressed pellets and packed powder-bed pellets was evaluated, and it was observed that unpressed powder most-closely produced the desired porosity morphologies. Eventually, a systematic set of sintered samples was created by sintering copper powder at 1065°C, which is 20°C below the melting point of copper.

The sintered pellets were characterized to map the evolution of density and pore morphology during sintering. One interesting observation is that the sintering did not proceed in a homogeneous, uniform manner and a porosity gradient formed within the pellet. More specifically, the sintered structures exhibited a 2-region characteristic where the outer region exhibited minimal densification with some with particle bonding while the interior region exhibited high levels of densification. In addition, at longer sintering times, the boundary between these two regions appeared to progress toward the pellet surface (i.e., the volume fraction of the dense internal region appeared to increase with sintering time). While this behavior would likely be undesirable if sintered copper was the desired application, the resulting structures provide multiple opportunities for future modelers to consider the surface energy and diffusion behavior on display in these results.

The evolution of the two-region sintered copper structure was characterized using image analysis methods. Image analysis was conducted on all the sintered pellets through their respective axial and radial cross-sections. Radial cross-sections showed only the approximate half of the pellet sample due to the process of cutting the samples. This factor influenced the results of the porosity analysis, and thus the image analysis results showed to be more accurate for the axial cross-sections. The dense central region was already present after a sintering dwell time of 1 h but became more visually evident from 2 h of dwell time and on. Post-sintering caliper measurements resulted in an average of 59.07% T.D. from, these values increased to an average of 70.30% T.D., after 12 hours. Average axial image analysis showed a decrease in overall porosity, starting from 9.50% porosity at 1 h to 4.99% at 12 h of sintering.

The following chapters are exclusively dedicated to copper sintering. Chapter 2 presents the relevant background information regarding the fundamentals of copper metal sintering.

Chapter 3 describes the materials, methods, and equipment to consider the development of the final procedure used to produce sintered samples. Chapter four describes results with the first section chronicling the evolution of and lessons learned from the experimental methods considered and the second section presenting the systematic results from the powder-bed sintering samples prepared at 1065°C. Chapter 5 presents a discussion of the results from the systematic study including the characterization of how the structures evolved with time.

CHAPTER 02

BACKGROUND

Different metals have individual properties which determine what will be the effect from a change in structure, and exposure to temperature or pressure. This chapter covers the sintering behavior of Cu based on results from different research studies that focused on similar parameters as this study. In section 2.1 the properties of the Cu used in this experiment are introduced and are later referenced in comparison to similar experiments by other studies reviewed. These previous findings helped improve and narrow the focus of specific parameters needed to obtain the theorized optimal homogenous porosity profile in the volume of Cu pellets for this research. Some information included in this section also shows how other theories, experiments and metal characteristics on powder metallurgy can affect the porosity and densification of sintered pressed powder Cu pellets [10, 12, 14]. Section 2.2 reviews studies conducted by project partners with one having studied similar sintering parameters on zircalloy spheres and the other on conducting modeling parameters to simulate sintering results in pellets. Hart studied and conducted pellet production and sinterization on U-10Zr powder. This zircalloy and the copper used for this study had similar thermal properties at the sintering temperatures experimented with. Pellet production and sintering results were compared to observe porosity and morphology. The results from these two studies were shared with Barry along the progression sintering and porosity results in the pellets, and these allowed for the computational model of pellet sintering to increase in accuracy over time.

2.1 Copper Metal Sintering

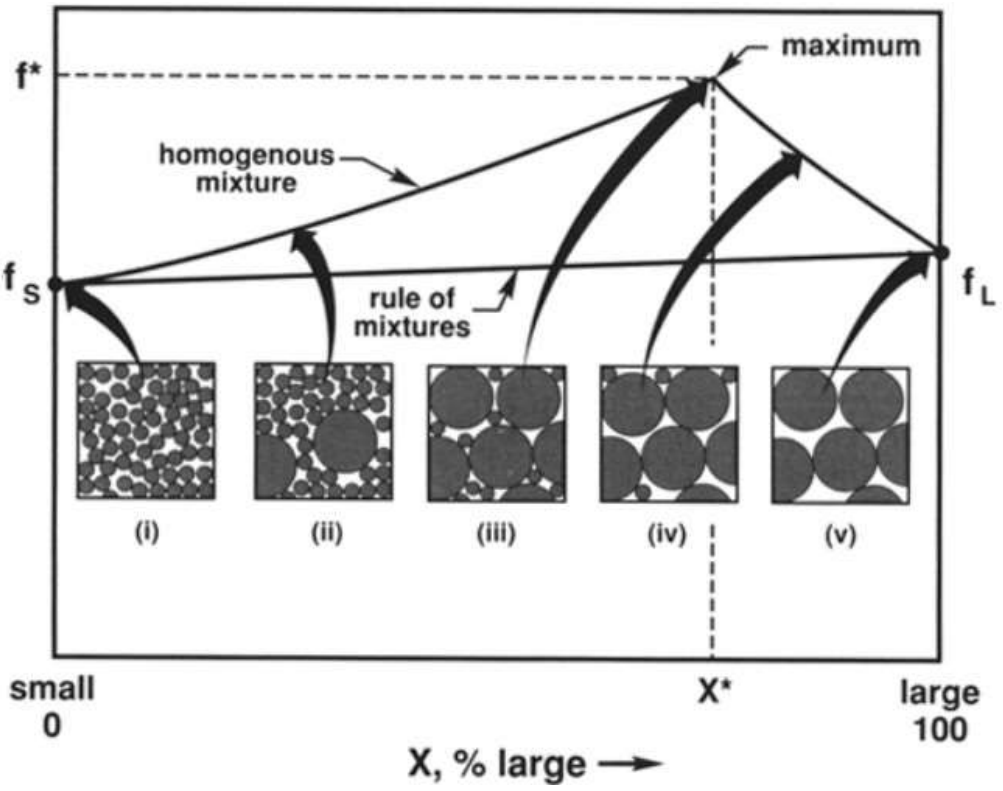

Figure 2: Packing density of spherical powders represented with according structure diagrams from 100 pct small particles to 100 pct large particles [19].

Packing and pressing a powder bulk composed of primarily large or small particles will have similar results and require a large amount of force applied to create a stable pressed pellet [15, 16, 21, 25]. However, too much force will cause excessive deformation and morphing within the volume of the pressed structure and spheres, especially in metals with high ductility such as Cu [17]. This subsequently leads to a higher amount of green density, which further increases during sintering. A large range of particle sizes in the bulk powder is also not ideal for homogenous volumetric porosity as there will be open voids of all sizes between the larger powder spheres, but there will also be corresponding smaller particles to fill a large portion of them, again creating a pellet with a high green density [23]. Taking this into consideration, the ideal particle size range

for the bulk powder in this project was found between diagrams (ii) and (iii) of figure 2. The bulk powder particle size range used to be pressed and sintered exhibited a stable pressed green pellet, with a degree of density low enough to increase with sintering time increments at a set temperature.

The technique of sintering is used to densify and morph a metal structure through exposure to a specific temperature for a set time range without reaching its melting point. Every metal has a different melting point and thermal properties which makes the sintering process unique for each, depending on the desired densification outcome. Most metals require a sintering temperature one third below its melting point to cause significant morphology. Sintering powdered metals at a temperature lower than that of one third below its melting point will not cause any significant changes in spheres and there will be no change in the density of the pressed structure, even with a long period of dwell time. The temperature rate at which powdered metals are sintered also causes a variation in results as this affects the materials around the material being sintered, and in the case of this study, a rapid sintering temperature rate could lead the surrounding materials to break and cause leaks. When combining the process of sintering and powder metallurgy, any combination of temperature, temperature rate and dwell time will produce different density values for the sample being exposed to these procedures. Sintering loose metal powder or a pressed powder structure at a temperature high enough and a sufficient dwell time to generate morphology will enable the following three stages within the structure: initial (a), intermediate (b), and final (c) (Figure 3). In the initial stage a, the spheres in the metallurgic powder start to morph with neighboring spheres around the closest surfaces. In the intermediate stage (b), the spheres start to deform and morphing into a shape with higher density and stability. This stage is also considered to be made up of open porosity since most pores are connected to other pores and create tunnels of porosity within the sample. By the final stage (c),

most spheres have diffused almost entirely, leaving behind a trace of pores from spherical surfaces which were too far apart to morph together, and required a higher temperature or longer dwell time to densify. When porosity is desired after sintering, the result will look like that of stage c. The pores in this stage are isolated from other pores or conglomerations of pores, this type of porosity is considered closed porosity.

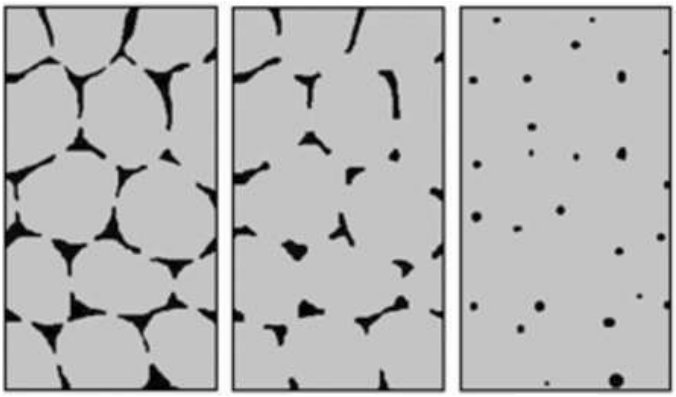

Figure 3: The three stages of sintering metallurgic powders. [6].

Cu has the characteristic of high ductility. This allows the metal to be dimensionally flexible and manipulated even at room temperature. Other metals such as Mo and Ta are not as ductile and require more force, time, and higher temperatures to be cut or morphed into a different shape. Ductility in metals is a correlation of its atomic bond. A strong metal implies a strong atom boding, but ductility defines the bonding between atoms referred as crystalline structure. Crystalline structure amongst metals displays how the atom bonds are organized. Some of the most common atom bond patterns include the hexagonal close packing (HCP), face-centered cubic (FCC) and body centered cubic (BCC) [3]. Assuming atoms are represented as spheres in 3D, HCP is the organization of a crystalline structure in which the second layer (layer B) of atoms is arranged so that atoms try to fill in empty surfaces between atoms in the base layer (layer A). Assuming the exact organization of these two layers is repeated and layered, labeled bottom to top ABABA…,

then the pattern is defined as HCP. If the pattern includes a new third layer (layer C) of atoms organized in a different manner as the previous layers A and B, the atomic crystalline pattern is defined as FCC or Cubic Closed Packed CCP.

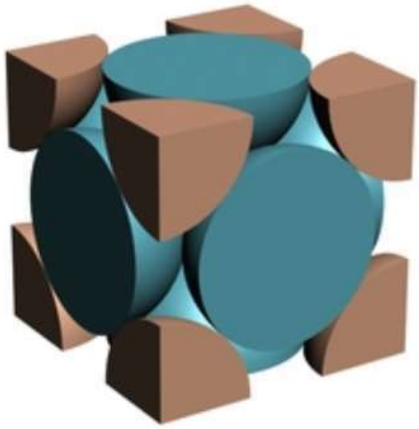

Figure 4: Visual representation of the atomic layer arrangement in an FCC crystalline structure [13].

Copper atoms are organized in the FCC crystalline structure, with an atomic radius of 0.1278 nm. The FCC structure in copper provides the atoms with small space for corrugation along the three layers of its crystalline structure. This allows the atoms to move while also keeping the same crystalline pattern during plastic deformation [2]. With plastic deformation, motion of a large number of dislocations of atom latices occur and this leads to a slip along the plane of movement. The process of dislocation of atom latices varies in levels of ease with each crystalline structure. There are specific directions along certain planes though which a slip system occurs and leads to dislocations. Some crystalline structures have several slip systems enabling the material's ductility. In the case for FCC, there are 12 slip systems. BCC structures can have 12 or 24 slip systems depending on the slip plane, and HCP can have 3 or 6 slip systems under the same considerations [13]. The higher number of slip systems in BCC and HCP can be attained only at higher temperatures. Copper maintains FCC structure at low and high temperatures, and thus providing

more control over results in this project. Copper crystalline structure consistency can also be seen in figure 5, when compared to other metals with HCP and BCC at low temperatures. This was an important characteristic since Cu pellet in this study were cut and polished at room temperature and a metal with brittle characteristics would not have allowed the proper progression on these techniques.

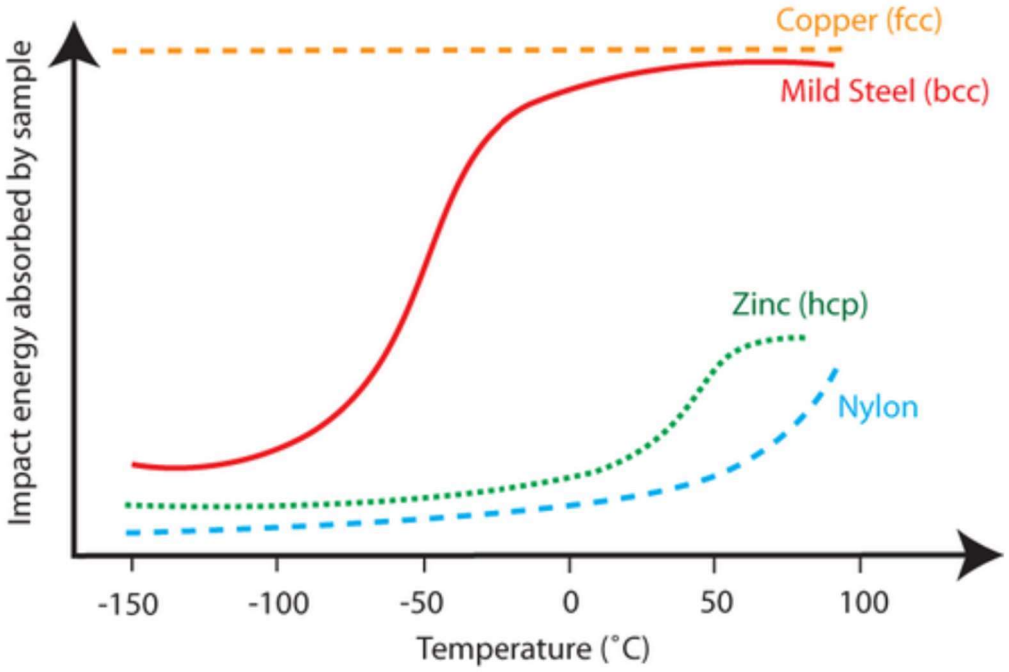

Figure 5: Impact energy abosrbency as a function of temperature for metals with FCC, BCC, and HCP crystaline structure.[32].

When heat is applied to metals, atoms start to vibrate and create more distance between each other. The atom planes can shift in different directions and cause the material itself to expand and morph into a different shape than what it was at room temperature. The extent to the deformation of Cu depends on the temperature it is exposed to. The melting point of the Cu powder used in this research is 1084°C.

A study was referenced in this study in which Cu wires with the same diameter thickness of 0.0128 cm were arranged into stacks of rows and cut before sintering to trace the 2D behavior

of spheres and pore morphology of the cross-section [8]. Experiments showed neck formation between the wires started at a lower dwell time for temperatures 95% of the melting point or above of Cu, between 1050°C - 1070°C. Temperatures below 1050°C took longer dwell time for wires to show signs of morphing. The next set of images show the cross-sectional view at different magnifications for set of dwell times at varying temperatures. Each image is labelled with different dwell times in h, with the top right image showing the time required at the sintering temperature for initial neck formation along grain boundaries of the wires.

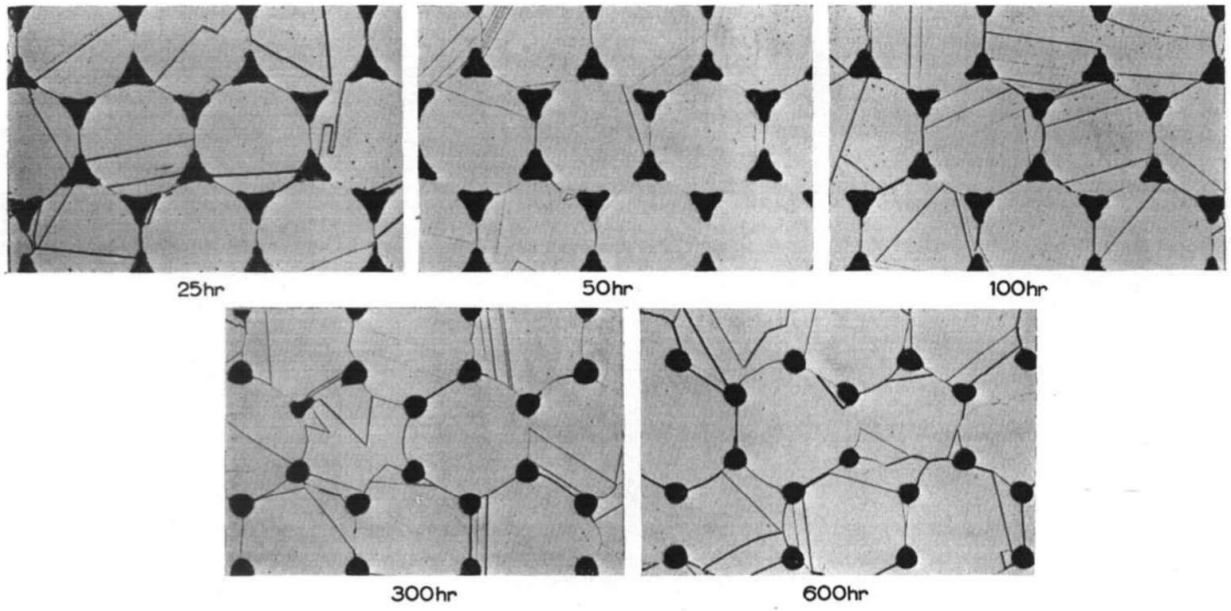

Figure 6: Cross-section of sintered wires at 900°C for dwell times of 25, 50, 100, 300, and 600 h (200x) [8].

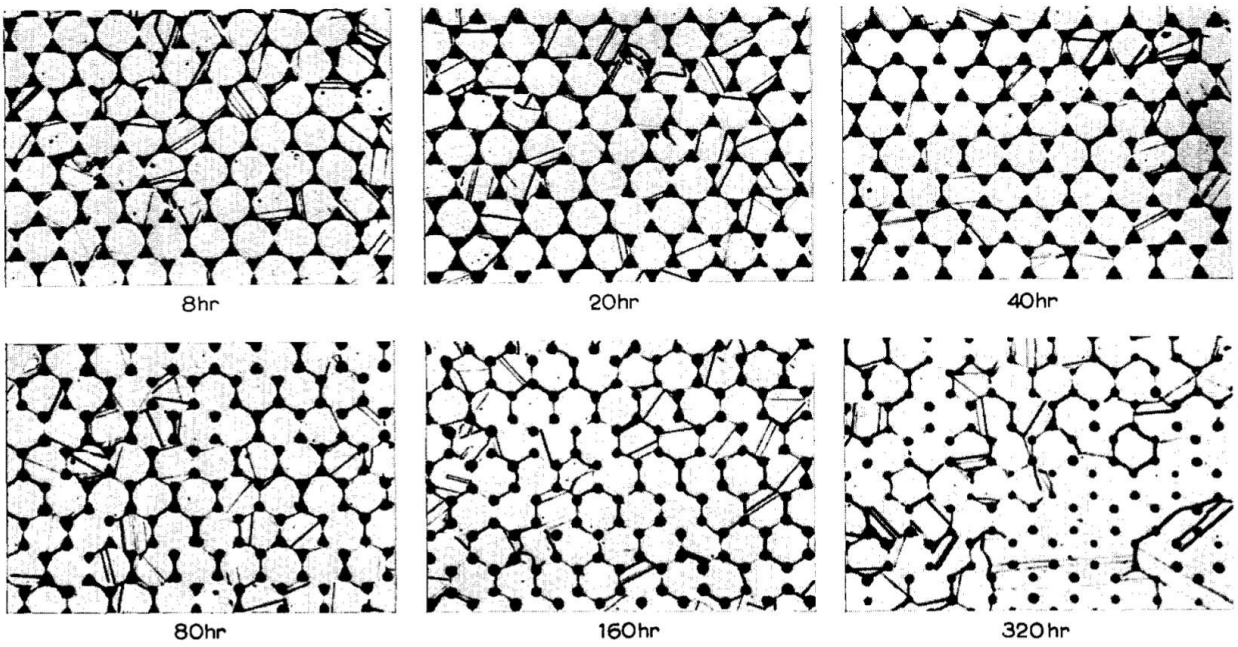

Figure 7: Cross-section of sintered wires at 1000°C for dwell times of 8, 20, 40, 80, 160, and 320 h (50x) [8].

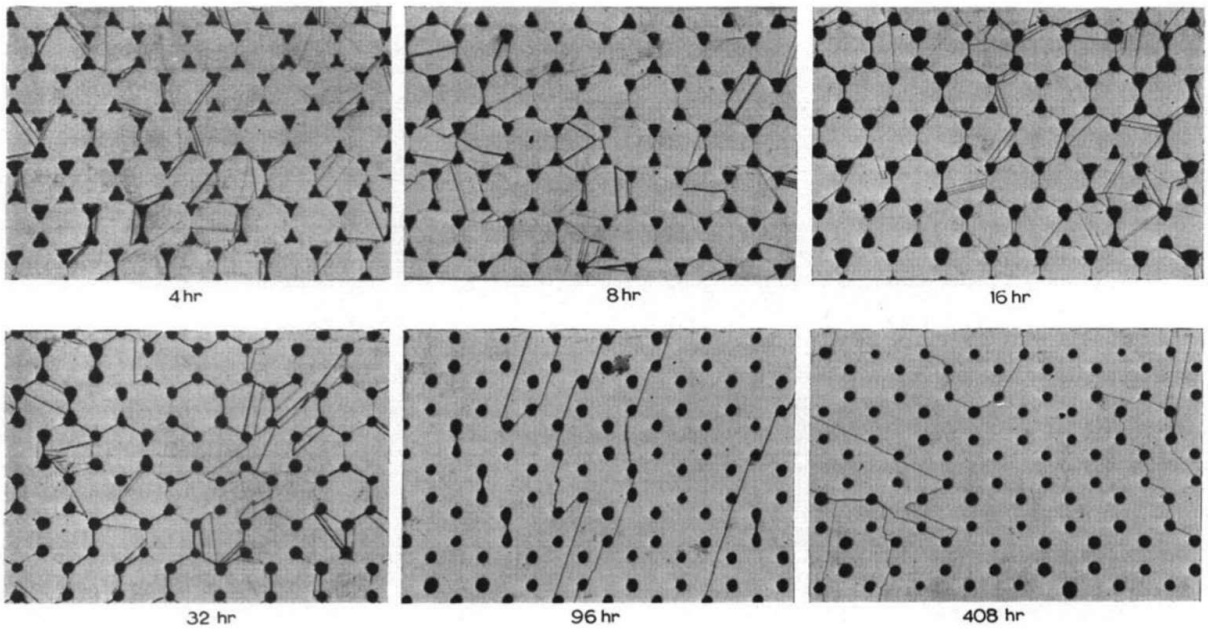

Figure 8: Cross-section of sintered wires at 1075°C for dwell times of 4, 8, 16, 32, 96, and 408 h (50x) [8].

As the sintering temperature approaches the melting point of Cu, the wire cross-sections in all the sintering temperatures iterations required less amount of time to start neck formation along

the wire boundaries. This was also the case for the wire spherical boundaries, which after several hours only leave behind pores instead of the wire intersections at the initial stage of sintering. Figure 9 shows the relationship between the density of Cu density and its dependence on temperature and dwell times. Higher temperatures require shorter dwell times to obtain the same density as lower temperatures at longer dwell times. When sintering at higher temperatures, closer to the melting point of the metal, dwell times for a specific density percentage can be a variable of minutes, instead of hours or days required for a low sintering temperature.

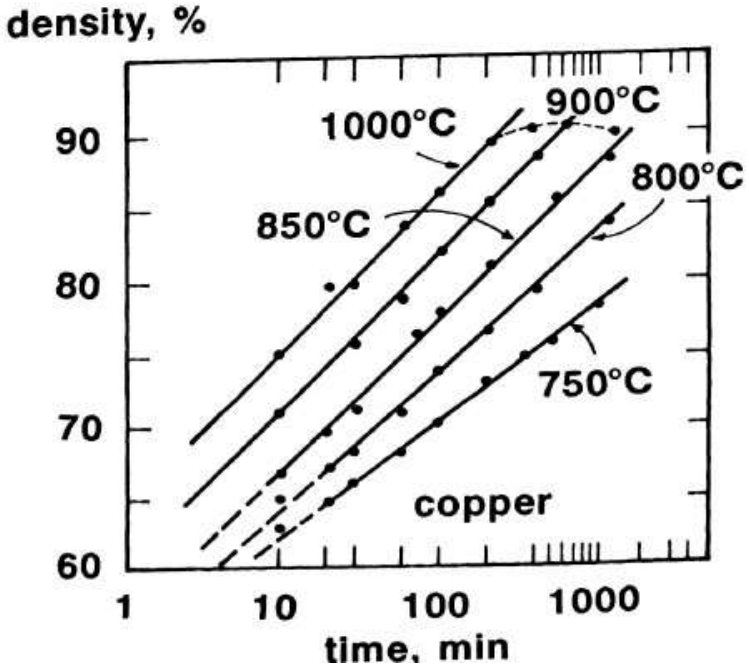

Figure 9: Density dependence of Cu on dwell time at sintering temperatures of 750°C 800°C, 850°C, 900°C, and 1000°C [19].

Considering the neck formation in a 2-dimensional cross-section from figures 6 through 8, sintering results change upon the addition of other variables in 3D cells such as pellets produced from pressed spheres with a set range of sizes. In the use of monomodal spheres, sintered pellet cross-section results can look like those of Alexander and Balluffi depending on the green pellet applied pressure and size range of the spheres.

The relationship between particle size and bulk porosity is shown in Figure 10. This is the porosity of the bulk of powder spheres prior to pressing. For the range of diameter used in this study, the graph shows bulk density between ~40% to ~50% of Cu. The amount of pressure required for a stable pellet then depended on the ductility of Cu, the amount of powder in the die and the pressure gradient along the volumetric range of the pellet.

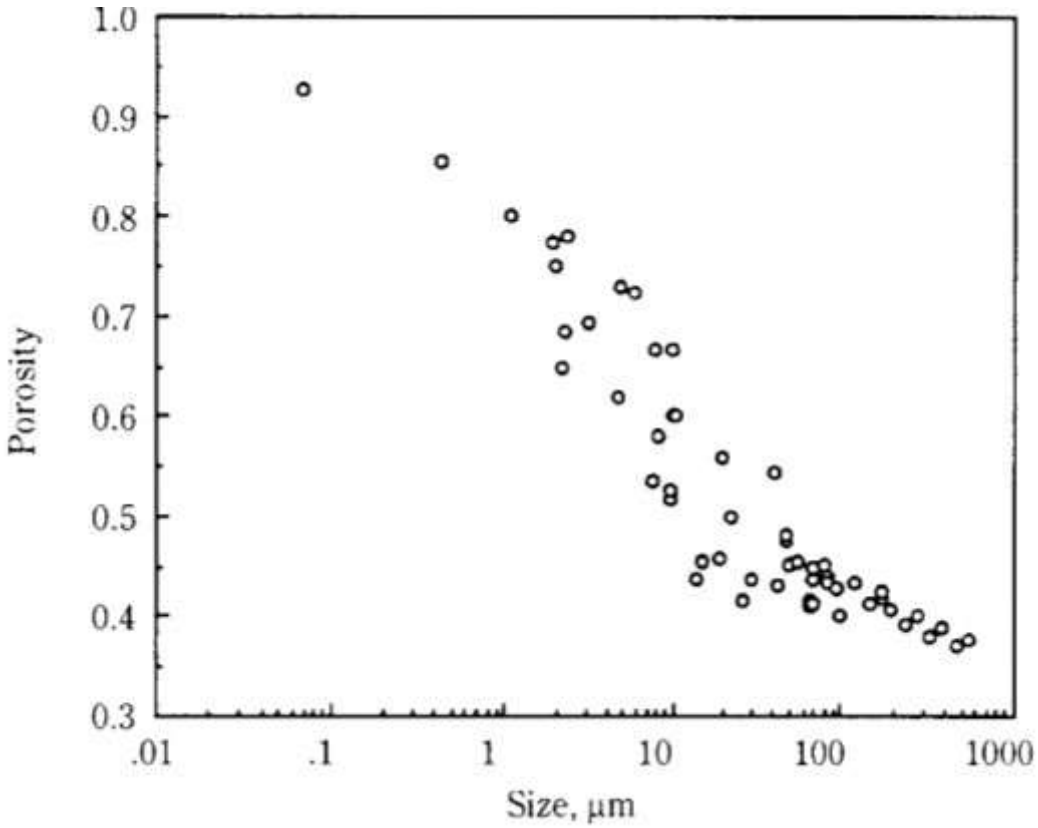

Figure 10: Graphical representation of porosity vs. particle size of Cu microspheres [18].

Different sizes of spheres also have different temperatures at which they begin to soften and morph into neighboring spheres, without melting. When smaller spheres make up the majority or entirety of the bulk powder, spheres will morph at a lower temperature and shorter time than a bulk with a mixture of larger spheres. This increases the density of the bulk or pressed volume with varying temperature and dwell time depending on the diameter range in the powder. Cu spheres with a diameter of 127μm can increase in density in a bulk from 60% to 67% after 300 h

at a sintering temperature of 1020°C, while spheres with a diameter of 9μm increase from 70% to 94% dense after 1 h dwell time at 900°C [19]. When a bulk of powder has a range of spheres with different sizes, the smaller ones will morph and densify at a shorter time than larger spheres. It was necessary to conduct several experiments to determine which temperature and dwell time works best for the desired results.

Experiments conducted showed that un-pressed Cu metal powder starts the process of deformation at a temperature close to 1050°C and a dwell time above 60 min, which can be seen from sintering time progression in Figure 11 [24]. The spherical diameter range used for these results was between 85 and 125 μm. In the first 45 mins of sintering dwell time at 1050°C there is no significant change in the Cu spheres. The first instance of deformation of the Cu spheres is noted between 45 - 120 mins of sintering dwell time at 1050°C. Neck formation is evident in nearly all spheres that were in contact at room temperature. At a dwell time between 120 – 220 mins, nearly all spheres have lost their original shape and have morphed to leave behind pores between the longest distances and vacancies of spheres' initial arrangement at room temperatures. As spheres are morphing together with increasing time, vacancies between spheres are shrinking and solidifying the bulk Cu powder to create a structure of connected particles and increasing in density.

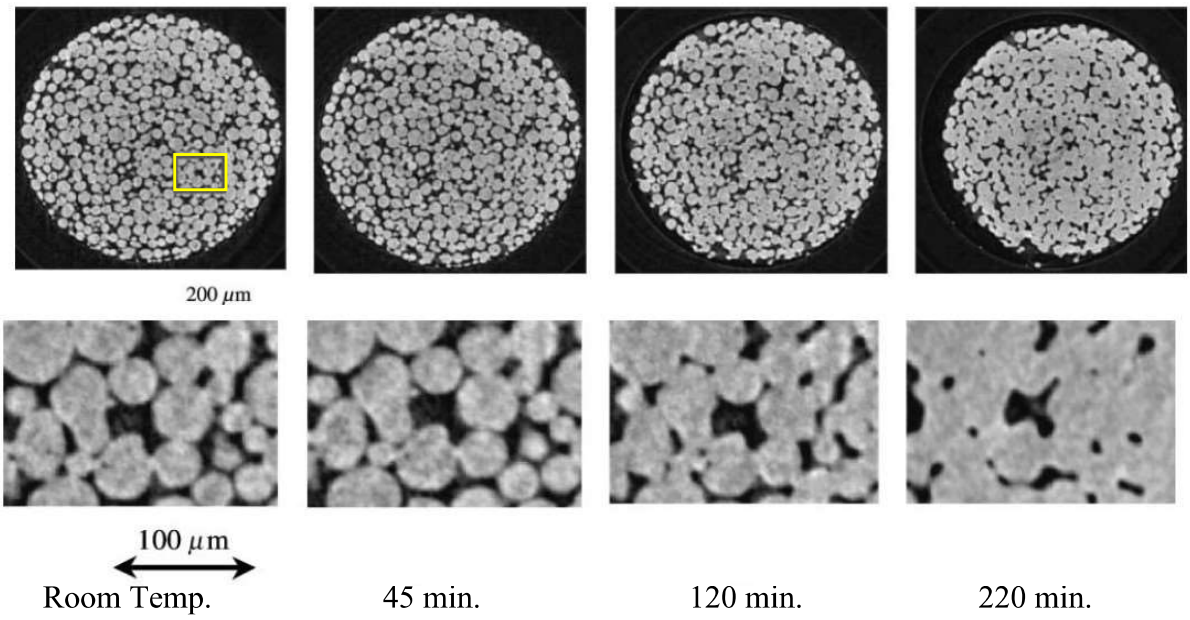

Figure 11: Progression of un-pressed Cu powder in increasing sintering dwell times. The yellow square representing the area of focus at a higher magnification [24].

2.2 Using Cu to Model Single Phase Sintering and U-10Zr for Double Phase Sintering

Cu is a single-phase metal, which does not change in crystalline structure at high temperatures. U-10Zr is 2-phase alloy which has an FCC crystalline atomic structure at high temperatures close to its melting point. This made the conduction of Cu pelletization and sintering trial results ideal for comparison to those conducted for U-10Zr spherical powder. The results from Cu palletization and sintering would then be compared and adjusted for those of U-10Zr to determine the conditions needed to produce and sinter a pellet that would contain a uniformly porous volume [20]. These sintering densification results were evaluated and replicated using a modeling program by Barry at the University of Arkansas. The sintering results obtained in this research with single phase Cu served as a guide towards a more accurate modeling program for U-10Zr simulations.

Pelletization and sintering results from Hart included the production of pellets with a diameter 0.6 cm and 314.7 MPa, using U powder spheres with a diameter range between 45µ-180µ, and >44µ of ^{10}Zr. U^{10}Zr pellets were pressed with a pressure between 8,000 and 12,000 lbs. pressure was held for 60 s to prevent immediate swelling of the pressed structure after production. Production and sintering of pellets were conducted in a glovebox to control the atmospheric oxygen and minimize oxidation of pellets from the U spheres. Data collected from green pressed pellets was recorded (Table 1).

Table 1: Pellet pressing results for U-10Zr microspheres done by Hart [20].

Sample	Pressure	Time	Mass	Volume	Density	% TD
	lbf	sec	g	cc	g/cc	
1	12,000	60	1.86	*	*	*
2	12,000	60	1.72	0.109	15.71	88.0
3	10,000	60	1.02	0.083	12.30	68.9
4	8,000	60	1.10	0.072	15.32	85.8
5	8,000	60	1.13	0.086	12.96	72.6
6	8,000	60	0.98	0.073	13.39	75.1
7	8,000	60	0.75	0.069	10.90	61.1
8	8,000	60	0.82	0.069	11.90	66.7
9	8,000	60	0.96	0.064	15.02	84.2
10	8,000	60	0.92	0.073	12.67	71.0

*Pellet was too fragile and sintered without measuring

Pellets were sintered at a temperature of 900°C with ultra-high purity argon for separate dwell times of 2, 4, 6, 8, 10 and 12 h. U10Zr pellet production, sintering and post-sintering preparation was like that of Cu pellets, with differences accounted for due to thermal and radioactive properties. Some varying post-sintering results in U^{10}Zr pellets were expected due to

the varying oxygen levels, which although kept low, still affected oxidation in pellets. Overall pellet trial samples considered for observation were numbered and analyzed to determine if they were suitable for further analysis. This data can be seen in table 2 where green and sintered values are denoted for each sample. Samples 1, 2, 3 and 4 were discarded due to failures in stability post sintering, or contamination from unexpected gases. Samples 5 through 10 were analyzed further and theoretical density was calculated pre- and post-sintering to denote the trend in dimensions dependent on sintering time (table 3).

Table 2: Densification trend in U-10Zr sintered pellets [20].

Sample	Mass_g	Mass_s	Trend	Vol_gr	Vol_snt	Trend	Dens_g	Dens_s	Trend
	g	g		cc	cc		g/cc	g/cc	
1	1.86	1.85	-0.01	*	0.133	N/A	*	13.92	N/A
2	1.72	*	N/A	0.109	*	N/A	15.71	*	N/A
3	1.02	*	N/A	0.083	*	N/A	12.30	*	N/A
4	1.10	1.08	-0.02	0.072	0.079	0.007	15.32	13.67	-1.63
5	1.13	1.13	0.00	0.086	0.085	-0.002	12.96	13.27	0.31
6	0.98	0.98	-0.01	0.073	0.072	-0.001	13.39	13.48	0.09
7	0.75	0.75	0.00	0.069	0.066	-0.003	10.90	11.38	0.48
8	0.82	0.81	-0.01	0.069	0.068	-0.001	11.90	12.04	0.14
9	0.96	0.95	-0.01	0.064	0.068	0.004	15.02	14.10	-0.92
10	0.92	0.92	0.00	0.073	0.072	-0.001	12.67	12.82	0.15

*sample not taken

Table 3: Theoretical density data for pellets considered for observation [20].

Hours sintered	% TD_gr	%TD_sntr	Trend	Sample
12	71.01	79.43	8.42	10
10	72.65	81.68	9.03	5
8	75.06	82.33	7.28	6
6	61.10	68.82	7.73	7
4	66.70	71.95	5.24	8
2	84.19	82.89	-1.31	9

Theoretical density data showed pellet dimensions to increase slightly (-1.31%) in the first two hours of sintering dwell time, a result expected due to spheres starting to migrate to begin morphing. After this, pellets showed to decrease steadily in density, with the exception between 6

h and 8 h, likely due to oxygen contamination. The highest difference in green and sintered trend occurred at a sintering dwell time of 10 h, with the dwell time of 12 h being slightly lower.

Images of the earlier sintered and polished cross-section of two separate $U^{10}Zr$ pellets were provided from a dwell time of 4 h and 6 h. Morphology in the zircalloy pellets differed to Cu due to the less ductile characteristic of the metal composition. U overall is not a metal that is easily manipulated, even the polishing stage. The axial and radial cross-sections were polished and afterwards analyzed through SEM imaging. Images for both sintering trials are shown in figure 12.

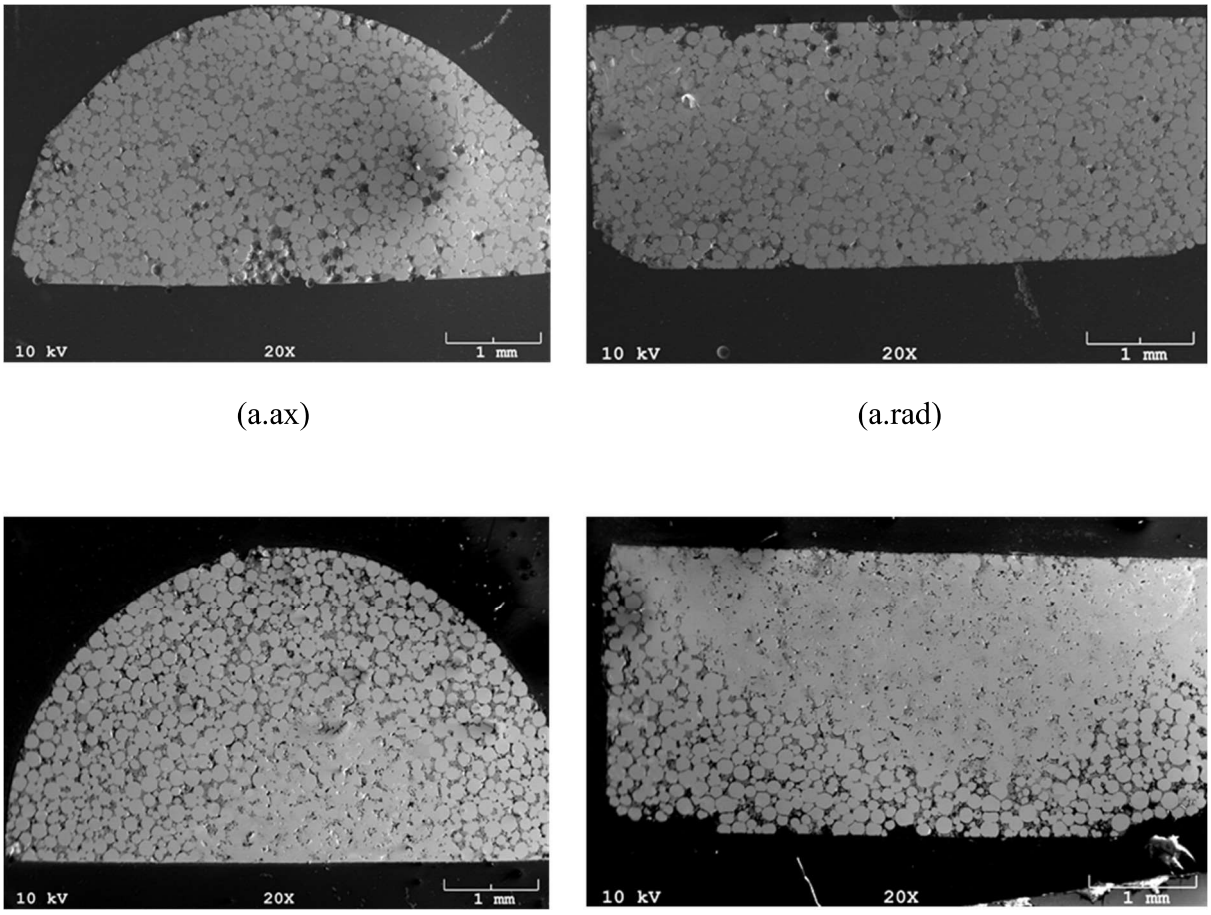

(a.ax) (a.rad)

(b.ax) (b.rad)

Figure 12: U-10Zr pellet cross-section sintering results obtained from Hart. (a.ax) and (a.rad) are the axial and radial cross-section of the pellet sintered for 4 h, (b.ax) and (b.rad) is sintered for 6 h [20].

2.3 Numerical Modeling of Sintering

Porosity and densification computer modeling simulations were conducted by Barry using MOOSE (Multiphysics Object Oriented Simulation Environment) Software and the implementation of Cahn-Hilliard equations. Simulations conducted in this study were restricted to a 2D field on fuel pins, to analyze results in a more simplistic manner and accounting for the initial complexity of variables prior to moving forward with the 3D simulations. Research focused on programing the behavior of various pore sizes and compositions in a 2D metallic circular structure through various sintering trials and a range of density in the metal. The metallic parameters assumed covered a range of theoretical densities and the ratio of small pores to total pores in the metallic space. The Cahn-Hilliard equations were implemented in this study to account for the representation of the phases of the metal at any point in the sintering process. This was particularly useful to more accurately simulate porous morphology relative to temperature and dwell time in multi-phase metals such as U-10Zr. Only axial cross-sections were programmed and simulated in this study.

Initial parameters for the 2D green fuel pin sintering simulations were conducted on U-10Zr material, with a percentage theoretical density (T.D.(%)) range of 92, 94, 96, as these densities have been shown to be accurate in previously in-lab produced U-10Zr green pellets. The percentage ratio of small pores to total amount of pores was denoted by χ(%) had a range of values of 0, 20, 40, 60, 80 and 100. Pores were randomly placed in the circular fuel pin for combinations of both T.D.(%) and χ(%) in varying simulations. A stochastic method was applied for the placement of the pores in the circular fuel pin.

Pre-sintering fuel pin simulations were programmed such that pores were not overlapped. The porosity profile and density in green fuel pin was compared to actual porosity values for

already produced pellets by Hart and were adjusted accordingly to obtain porosity quantities as close as possible in comparison. Density calculations were conducted by drawing a line across the porous cross-section and summing the program units accounted for the color set for the fuel, and dismissing the color accounted for the pores. Figure 13 shows the porosity configuration for the cross-sectional fuel pin with T.D.(%) = 92 and the complete χ(%) range. Error values between the simulated fuel pin and the actual pellets showed to be less than or equal to 3%.

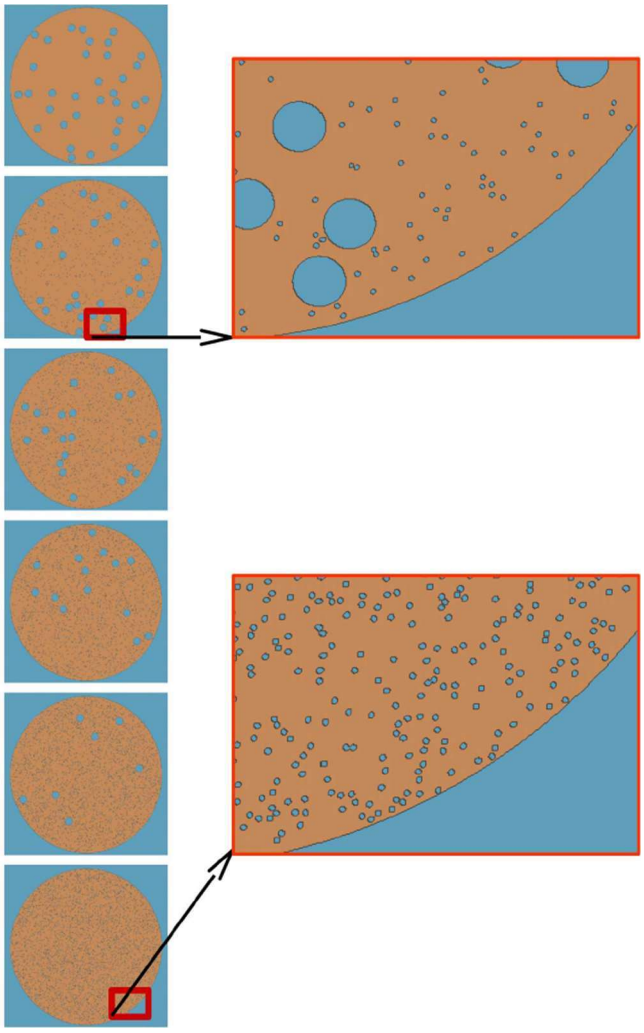

Figure 13: Visual porous configurations generated for a fuel pin with TD (%) = 92, and magnified portions of χ(%) = 20 and χ(%) = 100, to highlight the difference in porosity sizes [11].

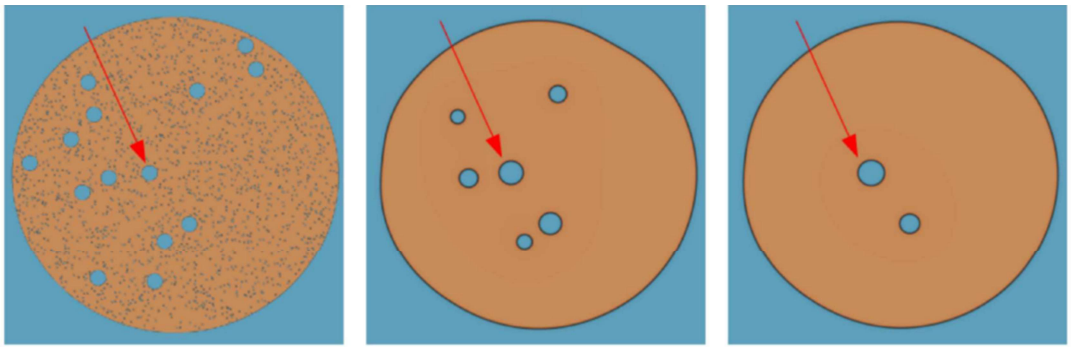

T=0 T=60 T=100

Figure 14: Large porous voids in a metallic surface becoming larger from smaller vacancies in the structure [11].

MOOSE simulations showed the diffusion of small pores into larger pores and sintering time increased through codebase time spaces denoted by nodes and the variable T (figure 14). T did not have any units. Densification occurred as the migration of pores from the center of the fuel pin to the surface. This was concluded from structures with bimodal spheres. MOOSE densification results correlated with densification seen in U-10Zr and Cu pellets. Pellet densification results were arranged in a series of graphs for the initial parameters previously mentioned for each T.D. variable dependent on χ. Data was tabulated for the cross-sectional over all area after sintering for a series of time steps, as the cross-sectional area decreased with increasing sintering time. These graphs are shown in figures 15, 16 and 17.

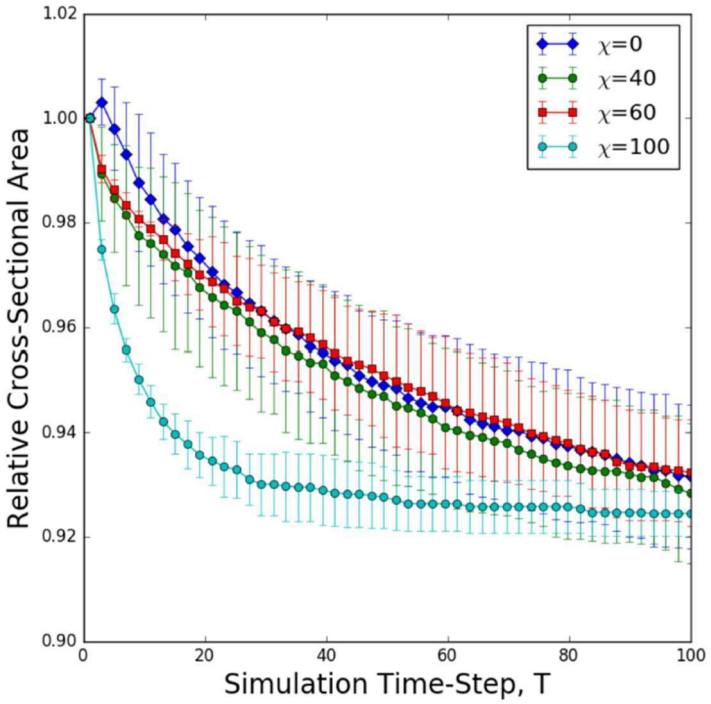

Figure 15: Relative cross-sectional area for T.D. = 92% [11].

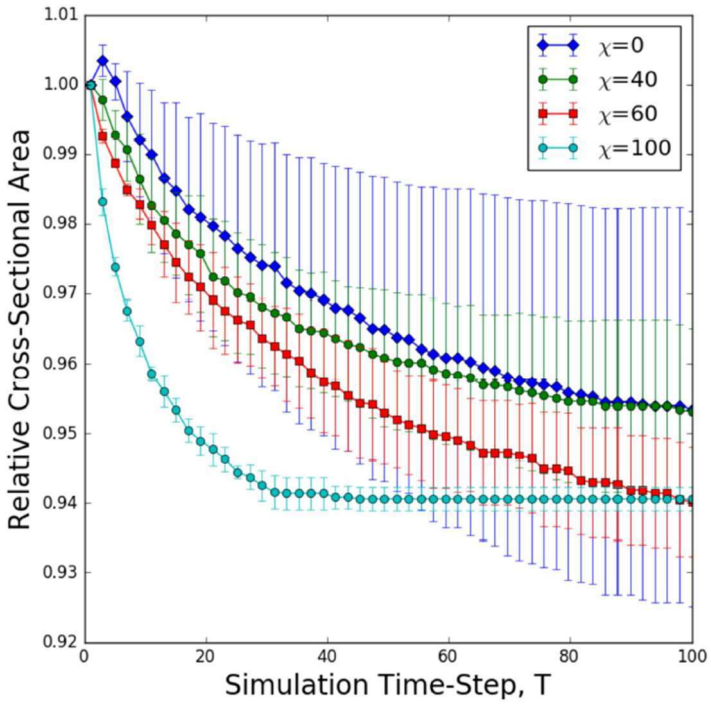

Figure 16: Relative cross-sectional area for T.D. = 94% [11].

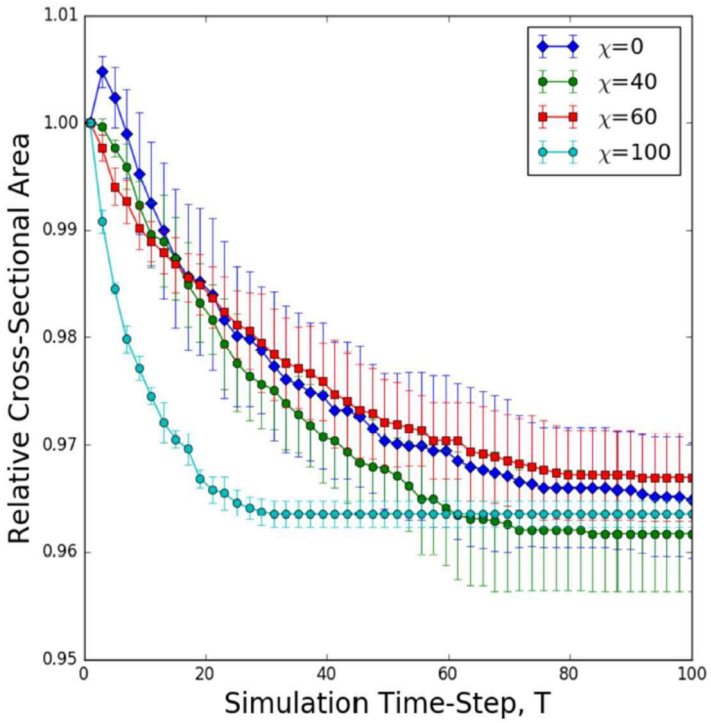

Figure 17: Relative cross-sectional area for T.D. = 96% [11].

The cases of T.D. (%), χ (%) = 100 showed the faster and larger loss in cross-sectional area, with the most significant decrease occurring between time-steps 0 and 20. T.D. = 92% had the most decrease in cross-sectional area compared to the other theoretical densities for χ(%) = 100. Bimodal cases for χ(%) = 40 and χ (%) = 60 in all T.D. (%) configurations showed a steady loss of cross-sectional area over a longer period of time, with T.D.= 96% showing χ(%) = 40 losing more porosity compared to χ (%) = 100. T.D.= 92% contained all χ (%) variables in a similar decreasing trend, while this was not the case for higher T.D.s. T.D.s ≥ 94% showed a plateau trend after T = 60 for all χ(%) except χ(%) = 100, which plateaus in the earlier stages of the time steps.

Vacancy concentration within the sintered fuel pin simulations was also analyzed in this study. This focus was intended to show how the size of pores and time steps affected the diffusion between pores and solid metal. Results showed that systems with monomodal large

pores took longer to transfer to the surface of the fuel pin, and monomodal small pores morphed together to form larger pores. Bimodal pore sized in the intermediate χ(%) values showed a longer diffusion time to be completely morphed out of the fuel pin. In bimodal cases, pores either morphed together or, if close enough to the surface, simply migrated out of such. Figures 18, 19 and 20 show the details of these results.

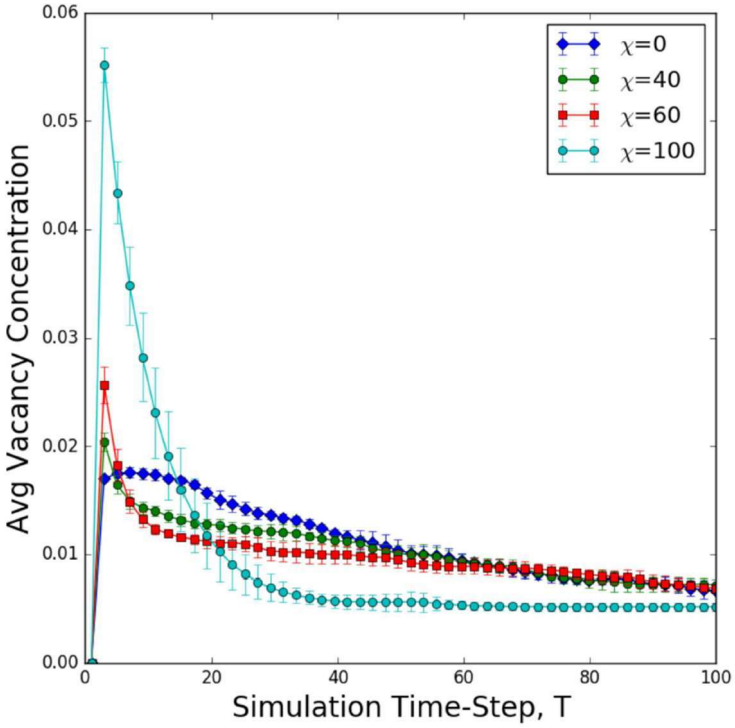

Figure 18: Average vacancy concentration for T.D. = 92% [11].

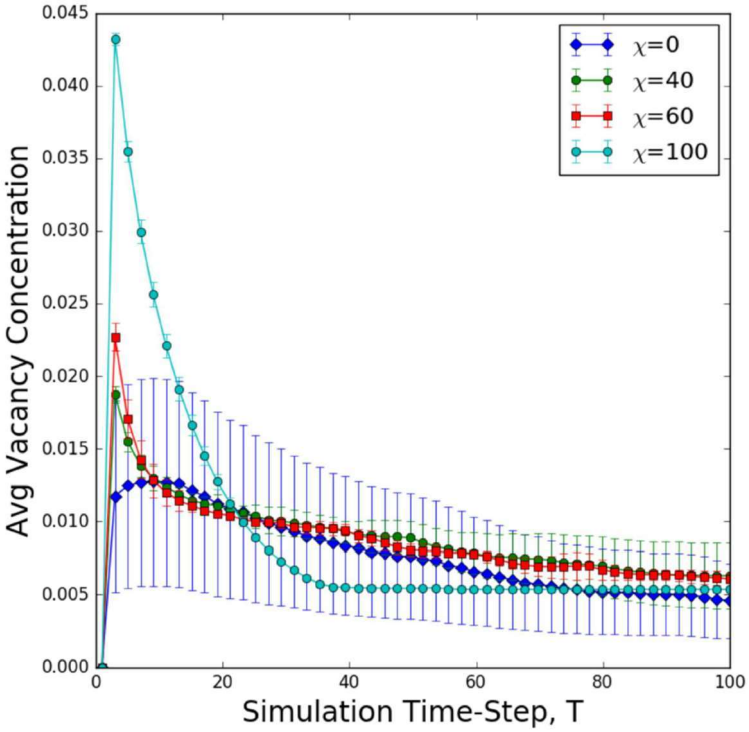

Figure 19: Average vacancy concentration for T.D. = 94% [11].

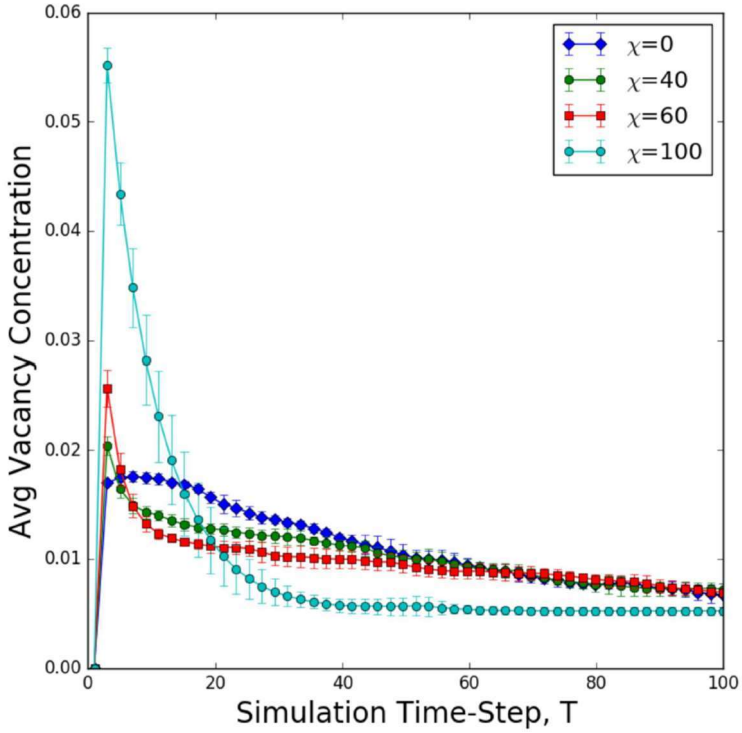

Figure 20: Average vacancy concentration for T.D. = 96% [11].

Initial data showed a short-lived spike in the average vacancy concentration in the early time-steps for all T.D. cases, followed by a decrease in all χ values, except for χ (%) = 0 which increased slightly. The largest overall decrease in average vacancy concentration seen for T.D. = 94%. Results comply with pore behavior seen in physical experiments conducted on U-10Zr and Cu.

CHAPTER 03
EXPERIMENTAL

This chapter describes the specifications of materials used and experimental procedures developed for pellet production, experiment preparation, sintering, and porosity measurement/analysis. Section 3.1 presents the copper materials used in this project as well as powder preparation and pelletization methods used to produce the sintered pellets. Section 3.2 covers the sintering system established in the laboratory and the sintering procedures. Sample characterization and image analysis is described in section 3.3, with descriptions of representative images and methods used to calculate porosity through theoretical and measured values using an immersion method. Section 3.4 outlines the image analysis procedures used to quantify and compare porosity data to those of section 3.3.

3.1 Copper Materials Used in this Work

The Cu powder used here was spherical, with spheres ranging in diameter between 44μm - 149μm, manufactured by Alfa Aesar. This was selected, in part, to provide a consistent starting geometry for the modeling activities [3] but also to use a flowable powder and facilitate repeatable starting conditions for the measurements. The product data sheet indicated that the powder also contained some microscopic flakes of copper. Microscopic analysis showed these flakes to fall within the diameter size range of the spheres and appeared as bundles of morphed spheres with the combination of two or more spheres. The sieving process allowed for a large quantity of these particles to be discarded, and the bulk of the powder contained a minimal portion of these morphed sphere bundles, as seen in figure 25.

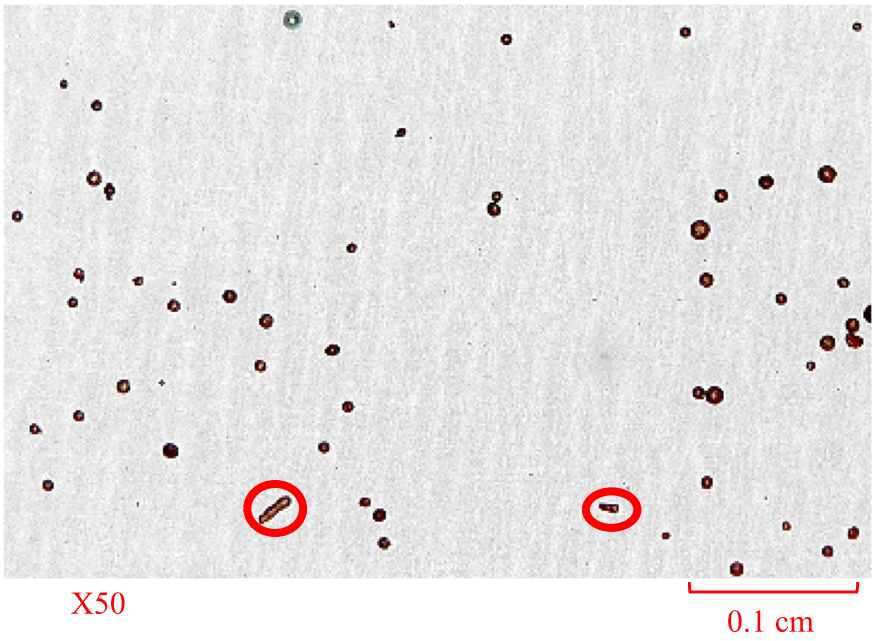

Figure 21: Magnified image (X50) of Cu microspheres under a Hyrox microscope, including two highlighted flakes/ morphed spheres.

The copper powder had a purity of 99.9%, a density of 8.94 g/cm^3, and a melting point of 1083 °C. The powder impurities for the two batches of Cu bulk powder used included Ag, Fe, Pb, Zn, Al, Ni, and Si at 30 ppm and 40 ppm, Sn between less than 20 ppm, C at 40 ppm and 20 ppm, and O_2 at 4950 ppm and 3457 (included in the online certificate of analysis of batches used, see appendix A). The purity of the Cu enabled well controlled, repeatable behavior during pellet production and sintering.

The microsphere powder was classified using two sieves to separate the spheres in diameter size ranges. The smaller size range contained spheres with diameters smaller than 45µm, followed by powder with spheres between greater than 45µm and smaller than 106µm, and spheres greater than 106µm. A bulk of 147.8g of Cu powder was meshed and each of the three separate size ranges were weighed to compare mass percentages. The diameter size distribution of the microspheres was estimated using images of the powder spheres with a Hyrox microscope and analyzed with

FIJI (ImageJ) to assure the size of interest was accurate. Table 1 shows the percentages calculated from the bulk of each diameter range.

Table 4: Percentage of diameter size range in bulk powder.

Diameter size range	Percentage of bulk (%)
Cu < 45μ	14.4
45μ < Cu < 106μ	64.2
Cu > 106μ	21.4

Particles smaller than 45μm were removed before pellet production because fine particles tended to stick to surfaces along the production process, thus the removal of which allowed for better control of pellet production and consistent sintering results. It was also noted in early trials that green pellets with a minimum of 10% or more of fine particles produced results with higher density and less porosity after sintering due to smaller spheres reaching a higher surface temperature and initiating morphology with other neighboring particles before larger spheres during sintering.

The range of mass percentages in the Cu bulk powder measured were compared with spherical diameter densities calculated through ImageJ from a total of 5325 particles. Figure 24 shows a histogram of the spherical diameter densities where the densest diameter size is between the range of ~45μm - 106μm, with 64.2% of the 5325 particles in this range, 14.4% below 45μm, and 21.4% above 106μm. Particles with a diameter bellow 45μm are particles that did not mesh out of the bulk. The calibration set to the microscope scale above the actual size by 3μm. Figure 24 represents a histogram of the microsphere diameter size distributions calculated, with size range in units of μm in open and closed brackets. Open brackets indicating the diameter size greater than the number to the right, and the closed bracket indicating the inclusion of the diameter size and anything smaller than the number to the left. A total of 3 spheres resulted with a diameter in the

(177µm, 209µm] range, a size too large for the range provided by the manufacturer label. This could be due to a large sphere entering the bulk by mistake from the manufacturer. There were few sphere dimeters above the 149µm limit specified by Alfa Aesar, a number small enough to not disrupt future results. The majority of spheres had a diameter in the range of (51,83], with the second and third largest diameters in the diameter size range of (83,114] and (114,146], respectfully. This showed that microsphere diameters provided by Alfa Aesar were mostly within the size range specified, with roughly 4.75% of the spheres having a diameter bellow 49µ. A portion of percentage could be attributed to error on measurement

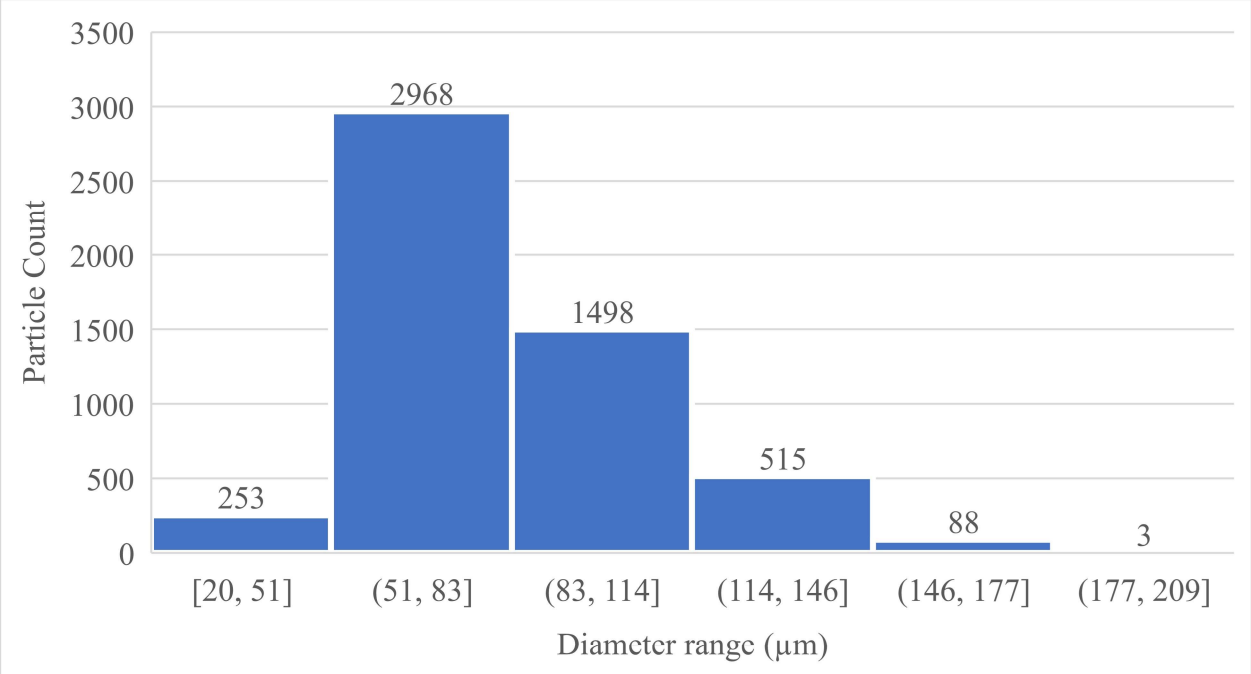

Figure 22: Histogram representation of diameter size ranges of spheres in Cu bulk.

Sintered powder pellets were prepared by using a closed-end alumina cylinder with an inner diameter of 1.48 cm; the tube height was customized by was cut to be shortened and enable the thermocouple to calculate the sintering temperature no more than 1.5 cm above the surface of the packed powder.

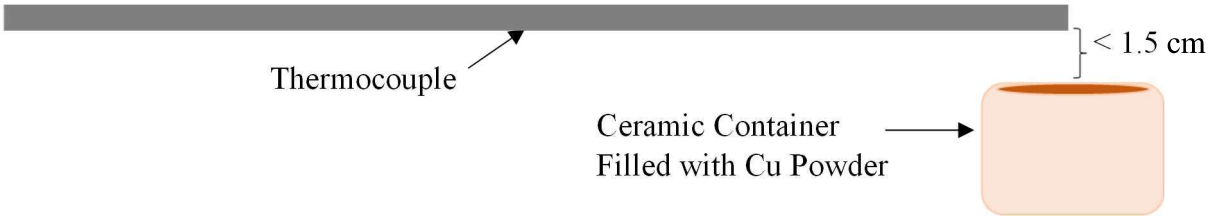

Figure 23: Sketch of thermocouple placement above unpacked powder containment.

The measured height of the loaded powder in the ceramic container was an average of 0.66 cm. The nominal measured geometric density of the pre-sintered powder in the cylindrical component was 4.80 g/cm^3 (58% of solid Cu). Early experiments performed to develop the sintering procedure revealed that proper, repeatable thermocouple placement was vital to avoid systematic errors exceeding ±10°C. The final sintering equipment configuration is presented in section 3.2.

3.2 Sintering

Figure 24 Shows the sintering furnace setup used for pellet sintering.

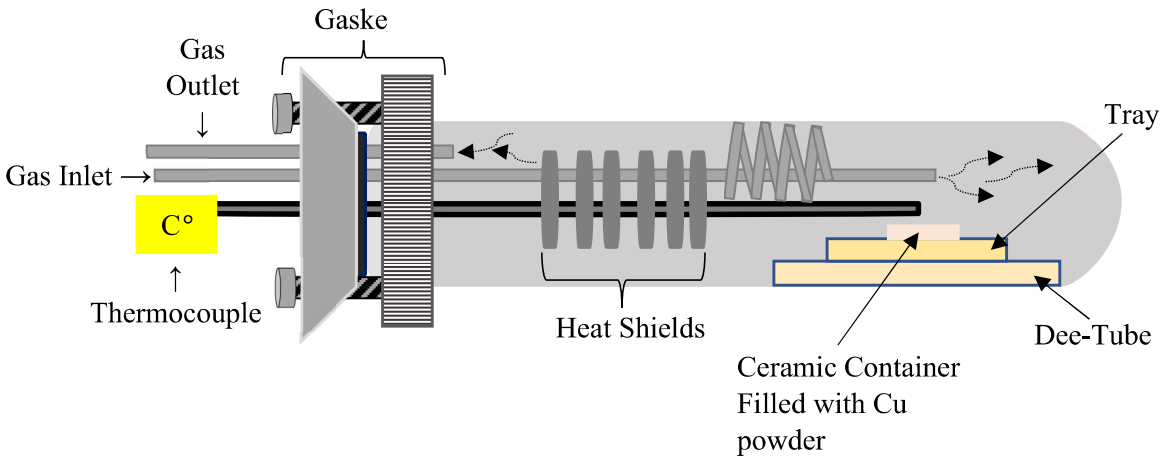

Figure 24: Sintering tube arrangement sketch represented as a cross-section of the setup including components of temperature reading, containment, proper seal, gas circulation, heat shielding and sample arrangement.

Sintering of the Cu pellets was performed in a controlled atmosphere enclosure within a tube furnace. The hot-zone portion of the furnace insert comprised alumina ceramic hardware and

metal tubing that were compatible with the operating conditions. The system hardware included a 21100 Thermolyne tube furnace placed in a horizontal arrangement. The sintering tube was held in place using ceramic fiber insulation.

Inside of the tube, an aluminum oxide (AD-998) dee-tube and tray were placed inside the alumina tube to support the Cu pellets during sintering. These ceramic components were rated for use up to 1750°C, far above the need for sintering trials. The sintering temperatures never exceeded1065°C.

A metal gasket seal was used to seal the open-end of the alumina tube with a built-in gas inlet/outlet for gas flow and arranged metal heat shields. Internal heat shields were used to protect the gasket material and components to prevent gas leaks during operation.

The gas selected for the inlet and outlet flow was 95% argon combined with 5% hydrogen. The main purpose of using the combined argon and hydrogen atmosphere during sintering was to prevent the Cu powder from oxidizing and allow for the enhancement of the metallic contact between powder particles. Additionally, the argon gas served to reduce the temperature gradient in the pellet as argon has a thermal conductivity of 0.0172 W/m°C. The inlet gas tube was twisted and bent as a coil with three loops along mid-end length to allow the gas to heat up before reaching the sintering atmosphere in the ceramic tube.

Upon preparing the powder for unpacked Cu powder sintering, the mass and average dimensional measurements were recorded to calculate a green bulk density. It was determined in early pellet trials that this value had a higher uncertainty for the green pressed pellets than the loose powder sintered pellets, as the loose powder was always poured into the cylindrical container up to the same height and the diameter was constant as the same container was used every time. The

marked set height for the loose powder was set to 0.3 cm below the top of the alumina cylinder. The sample tray was tied to a set measured position along the dee-tube with tungsten wire to keep the samples from moving too much through the tray along the dee-tube for every sintering trial (Figure 25). The sample was placed on the middle of the tray, and the dee-tube was placed at the end of the alumina tube. The gasket was sealed with the tip of the thermocouple placement fixed to be <1.5 cm above the top of the pellet's center.

Figure 15: Sample tray placed on set location on top of the dee-tube, held in place by tungsten wire to prevent shifting of lose packed powder during handling or sintering.

The cover gas for the sintering tests was an argon-95% hydrogen-5% mixture and the gas flowrate were set to a minimal flowrate. The Furnace temperature rate was set to automatically increase at a temperature rate of 30°C per minute, and manually operated to dwell at selected

temperature steps prior to reaching the sintering set temperature. The alumina sintering tube was placed in the furnace such that the sample was positioned at the center of the furnace. Both ends of the tube furnace were covered accordingly with insulation to minimize heat loss and high temperature gradients. The rest of the alumina tube was placed on top of insulation bricks to keep the sample leveled and prevent the sample from moving around due to imbalance.

Figure 26 shows the described furnace and alumina tube setup.

Figure 26: Furnace and sintering tube setup, with the sintering tube and all components inserted in the furnace horizontally, including insulation, bricks for placement stability and gas outlet/inlet.

Temperature dwell steps were implemented at the same temperatures for each sintering trial to increase control of the temperature displayed by the furnace compared to the actual temperature recorded by the thermocouple, as there was always an observed gradient difference in both temperatures, with the thermocouple in the sintering tube reading higher. Sintering temperature was set through the furnace manual control then compared to the thermocouple recording, with this procedure being repeated after every temperature increase until reaching the set sintering temperature in the thermocouple. A slow stepwise approach was implemented during every sintering trial at 550°C and 965°C for 15 min until the thermocouple reading on top of the Cu sample read 1065°C. Temperature recorded from the thermocouple was on average 21-28 °C

above the temperature marked by the furnace manual control. Upon reaching the set sintering temperature, the thermocouple was monitored for 15 min, as the temperature in the system would decrease by 1-2 degrees in the process of the atmosphere in the alumina tube came to a temperature balance.

The system was monitored routinely over the dwell time to make sure the sintering atmosphere continued to flow and that the temperature did not fluctuate. Pellet sintering was conducted with dwell times of 1, 2, 3 and 4, 6, and 12 hours. After sintering, the furnace was turned off and the system took over 5 h to cool while a flowing cover gas was maintained.

3.3 Sample Characterization

Figure 27 shows a simple setup sketch for the submerged Archimedes' measurement.

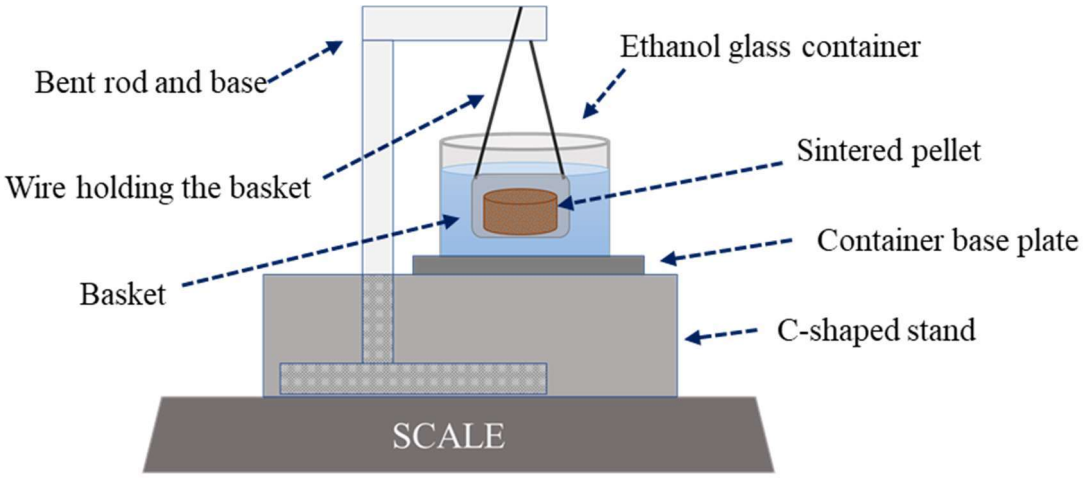

Figure 27: Scale setup sketch for submerged mass measurement of pellets including scale and, suspension, and containment components.

After sintering, dimensions and mass were recorded for each sample to compare the density and porosity before and after sintering. The theoretical density of the samples measured with calipers which nominally yield higher uncertainty as the pellets were considered solid cylinders. The measured radius and height produced the volume (eq. 1), and then the mass was recorded to

determine the density (eq. 2). The average of three recorded measurements for each dimension was used to calculate the average volume and density.

$$V = \pi r^2 h \quad (1)$$

$$\rho = m/V \quad (2)$$

Archimedes' principle for immersion method calculations required three mass measurements to more accurately measure the porosity in the entire volume of the porous makeup of each pellet estimate open and closed porosity. Ethanol was used as the immersion liquid, with a density of 0.79 g/cm^3 Three separate mass measurements from each sample were obtained to calculate the porosity of the sintered Cu pellets: the dry mass, the saturated mass, and the submerged mass.

The dry mass of the pellet samples accounted for the mass of the dense portion of its volume. Each pellet had to be completely dry to avoid errors in porosity calculations for this measurement. The submerged mass of the pellet considered the pores in the pellet volume to be filled with fluid and accounted for open porosity. Open porosity being the interconnected pores which were created from morphed surrounding spheres and became isolated from other neighboring pores. This measurement required the pellet to sit in ethanol for a few minutes prior to measuring to assure most pores were filled. This was noted by the air bubbles emitted from the submerged pellet in an ethanol filled container. Submerged mass measurements were conducted with the use of an in-lab constructed buoyancy scale setup. The setup had to consider only the mass of the sample and not the materials used.

A small cylindrical mesh container with large enough to fit sintered pellets and an open upper surface was used in the submerged mass scale setup. The basket was suspended by

malleable think wire on a hook attached to a bent rod. The rod was wrapped firmly around a flat circular base for support and stability. This rod and suspended basket were set at the center of the scale, while a semi-circular ring stand was placed just around the scale, while not adding to the mass components, surrounding the rod and its base. A base plate was placed across the stand to support a clear glass container filled with ethanol. The suspended mesh basket was placed inside the ethanol container, while the ethanol had to cover the basket completely and not to close to pour off. The basket and the wire used to suspend the pellet sample from the hook did not touch any side of the ethanol container.

The saturated mass of the pellet was measured by again submerging the pellet in a separate ethanol container to that of the saturation measurement setup until the pores were filled with the fluid. This measurement accounted for the mass of the pellet's Cu and the pores since these would be filled with ethanol. After the pellet was submerged, the sample was taken out of the fluid to remove the excess ethanol on the surface of the pellet with a damp cloth to obtain a more accurate saturation mass. A sealed empty container's mass was considered and cancelled on the scale to contain and attain the mass of the saturated pellet. The sealed container slowed the process of ethanol evaporation and fluctuation of saturated pellet mass.

Each Archimedes' mass measurements dry (M_D), submerged (M_{Sub}), and saturated (M_{Sat}) were measured three times and calculated into an average. Each average value was then implemented into several equations to calculate the open porosity ϕ (eq. 3), open porosity percentage $\phi_{\%}$ (eq. 4), pellet density/ Archimedes' density ρ_A(eq. 5), density percentage compared to solid copper $\rho_{A\%}$(eq. 6), where the density of copper is ρ_{Cu}= 8.94cm^3, and overall porosity P derived from the calculated density and density percentage (eq. 7) .

$$\phi = \frac{M_{Sat} - M_D}{M_{Sat} - M_{Sub}} \quad (3)$$

$$\phi_{\%} = \phi * 100 \quad (4)$$

$$\rho_A = \left(\frac{M_D}{M_{Sat} - M_{Sub}}\right) * \rho_{Ethanol} \quad (5)$$

$$\rho_{A\%} = \frac{\rho_A * 100}{\rho_{Cu}} \quad (6)$$

$$P = 100 - \rho_A \quad (7)$$

Uncertainty values in theoretical porosity measurements derived from the pellets not representing the exact shape of a cylinder as some pellets had small distortions along their surface area from porosity and particles which did not morph, or small portions of pressed powder which fell off pellets' edges after production. Theoretical density and porosity measurements were also not representative of the porosity inside the pellets' volume. These uncertainties were not present in the Archimedes' measurements, since that method does not consider the shape of the sample. Uncertainty values for theoretical and measured values were calculated individually by evaluating the standard deviation of each measured value and the standard deviation of the calipers and scales used.

3.4 Image Analysis

Radial and axial cross sections were cut from each sintered pellet after recording the theoretical and Archimedes' density measurements described in Section 3.3. A diamond saw was used to obtain the cross-sections. Each pellet was initially cut vertically near the center of the circular surface of the pellet and then one of the halves was cut horizontally along the center of the height of the pellet (Fig. 28). The arrangement of the pellets on the saw and the saw blade varied slightly between samples and this caused modest variations in cross-section dimensions and

overall cross-section area. The axial and radial cross-sections along the center of pellets was observed in earlier experiments to be the section where the most optimal porosity profile could be observed, and relative to the overall volumetric porosity of the pellet.

As noted in Chapter 4, the copper volume closer to the edges of the samples contained more porosity and the center section of each sample had a remarkably higher density in both axial and radial cross-sections. The radial and axial cross-sections from each pellet sample were arranged and hardened in epoxy for polishing

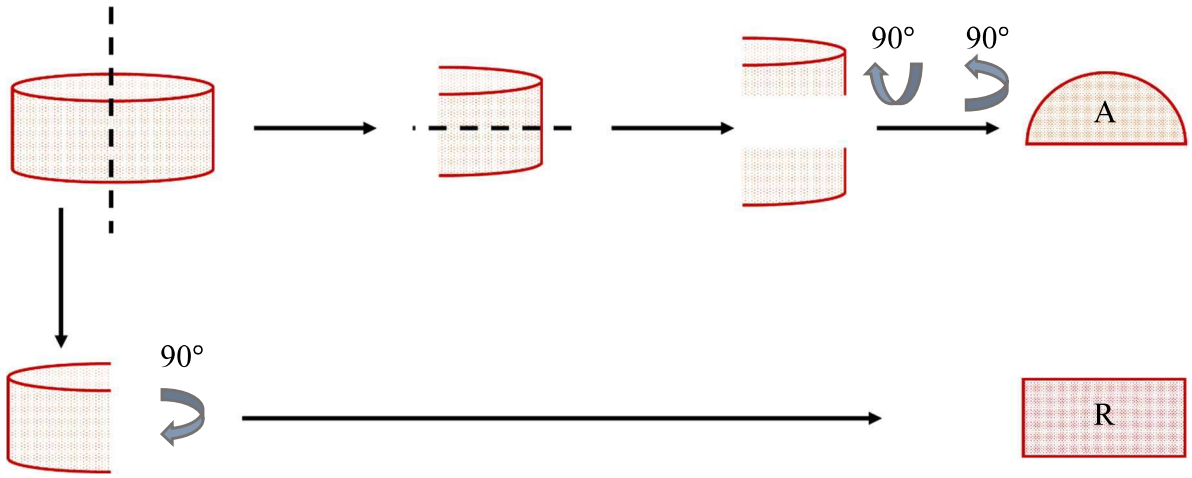

Figure 28: Sketch depiction of pellet cross-section slicing to obtain axial and radial cross-sections from each of the sintered Cu microspheres pellets.

The polished surfaces were prepared to obtain clear visualization for SEM images and porosity analysis. A megamet (Buehler, MetaServ 250) with water-based lubricant was used with a disc grinding speed between 250 and 350 rpm. Polishing SiC sheets were used in order of grit size from 120, 240, 320, 400, 600, 800 and 1200, using ethanol to clean the sample through sonication between polishing sheets. The epoxy hardened pellet cross-sections were held over the spinning megamet polishing sheets one at a time, with minimal pressure to keep the sample gripped in hand, but not so much pressure as to press the sample down on the sheet. Cu's malleability made the polishing easy and fast apart from loose unmorphed spheres which caused scratches on the

cross-section surface in the process of polishing. Applying too much pressure would cause more scratches to appear from pullout and wearing down of the cross-section. Sample sonication was conducted for less than one minute per sample in ethanol before moving onto the next consecutive polishing sheet to prevent the epoxy from softening. The samples were analyzed under an optical microscope after to detect major scratches on the polished cross-section. The cross-section was polished again at a 600-grit polishing sheet if any major scratches were still visible from the optical microscope, then polished through the rest of the polishing sheet sequence until minimal scratches were observed.

After final polishing and sonicating, all samples were placed (polished side up) in a vacuum chamber for at least 5 h to extract and minimize moisture in the pores. The clean polished surfaces were coated with carbon using a 108C Auto Carbon Coater (Ted Pella, Inc.). The samples were mounted for SEM imaging copper using tape along at least two sides of the pellet cross section to enable better image resolution. The sample holder was then placed inside the microscope chamber. The sample cross-section was analyzed upon reaching a low level of vacuum pressure in the chamber at or under $5x10^{-6}$ torr.

Pellet cross-sections were too large in areal dimensions to fit into one single image in the SEM at the lowest magnification of X10. Instead, several overlapped images were collected across the whole pellet cross-section and "stitched" together using ImageJ to enable porosity analysis. ImageJ's stitching feature allowed for two images to be stitched together after manually arranging them. However, SEM's magnetic setup feature caused images to have higher astigmatism effect around the edges and this distorted the shape of the cross-sections and its porosity at lower magnifications. With higher magnification, the distortion around the images would minimize, where a magnification of 5x0 showed no distortion and images were arranged and stitched together

on ImageJ with no issues. A magnification of 35x was arranged to be used for all images in this study to analyze the cross-sections' porosity, and image stitching was ruled out since a magnification of 50x was too complicated to use for reasons of time consumption and visual impediment with SEM monitors.

A magnification of 35x produced the least stigmatism effects along image edges, while monitoring the microscope lens through any specific location along the sample with more ease. Cross-section set of images were composed of meshed rows overlapped images (Figure 29). The results from these images are presented in Chapter 4, but Fig. 29 shows a representative set of images for this method. The overlap amongst the images assured that no sections would be omitted or overanalyzed during porosity analysis. Images from each sample were then compiled in MosaicJ to examine the points of overlap in each image and crop this portion out of individual images. Every cross-section's first captured image started at the lower left corner of radial and axial cross-sections, and the sequence of overlapped images continued to the left along the bottom row, with the sequence changing from left to right for images taken atop the bottom row. This process was repeated until images were captured from the whole cross-section of the pellet. Images were labelled through a number organized by row number (R) and image sequence number (S), R.S. Some cross-sections varied in the number of rows and image sequence numbers due to user error and cross-section sample size.

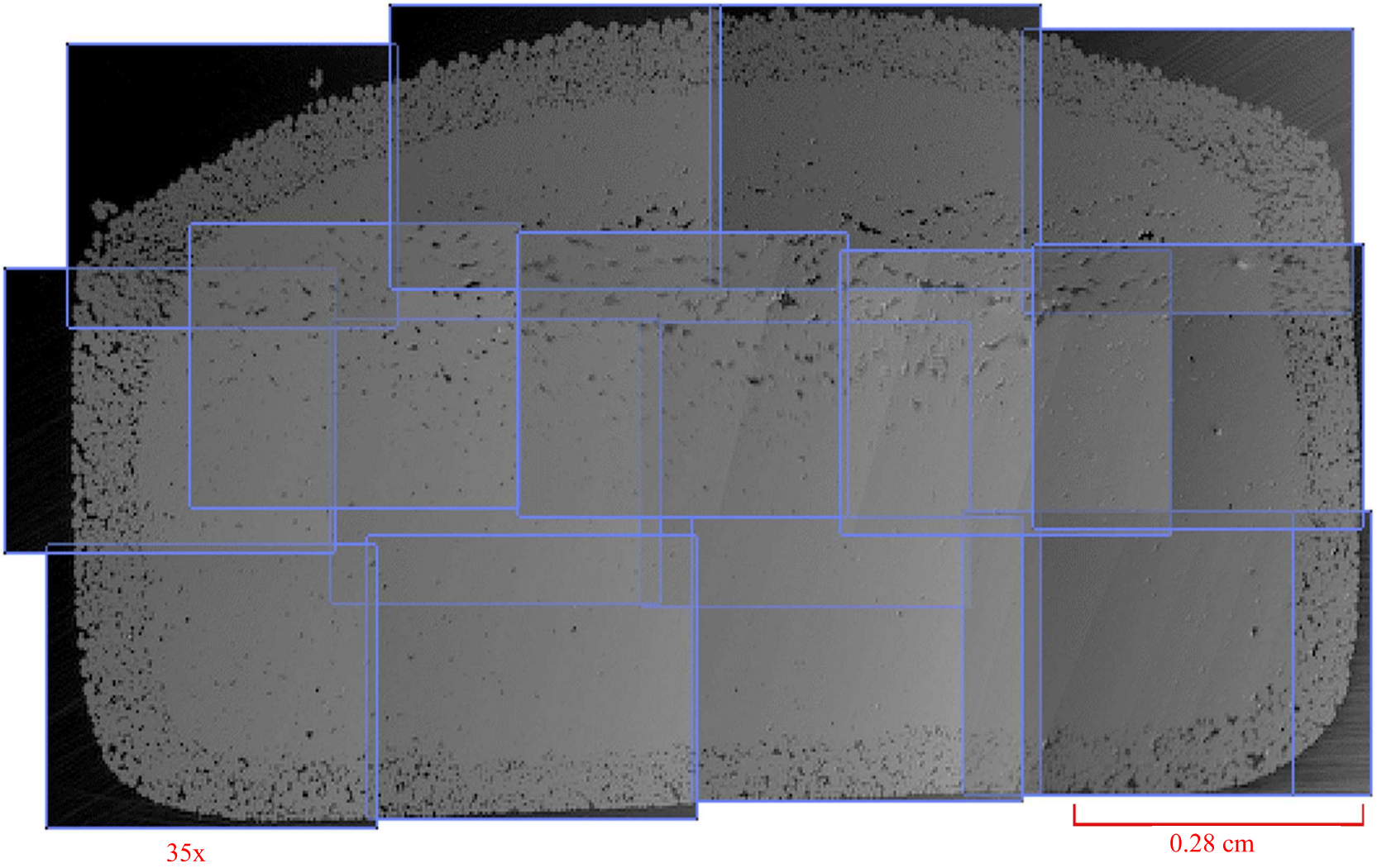

Figure 29: Axial cross-section image mesh compilations in mosaic, with each individual image computed with a magnification of 35x.

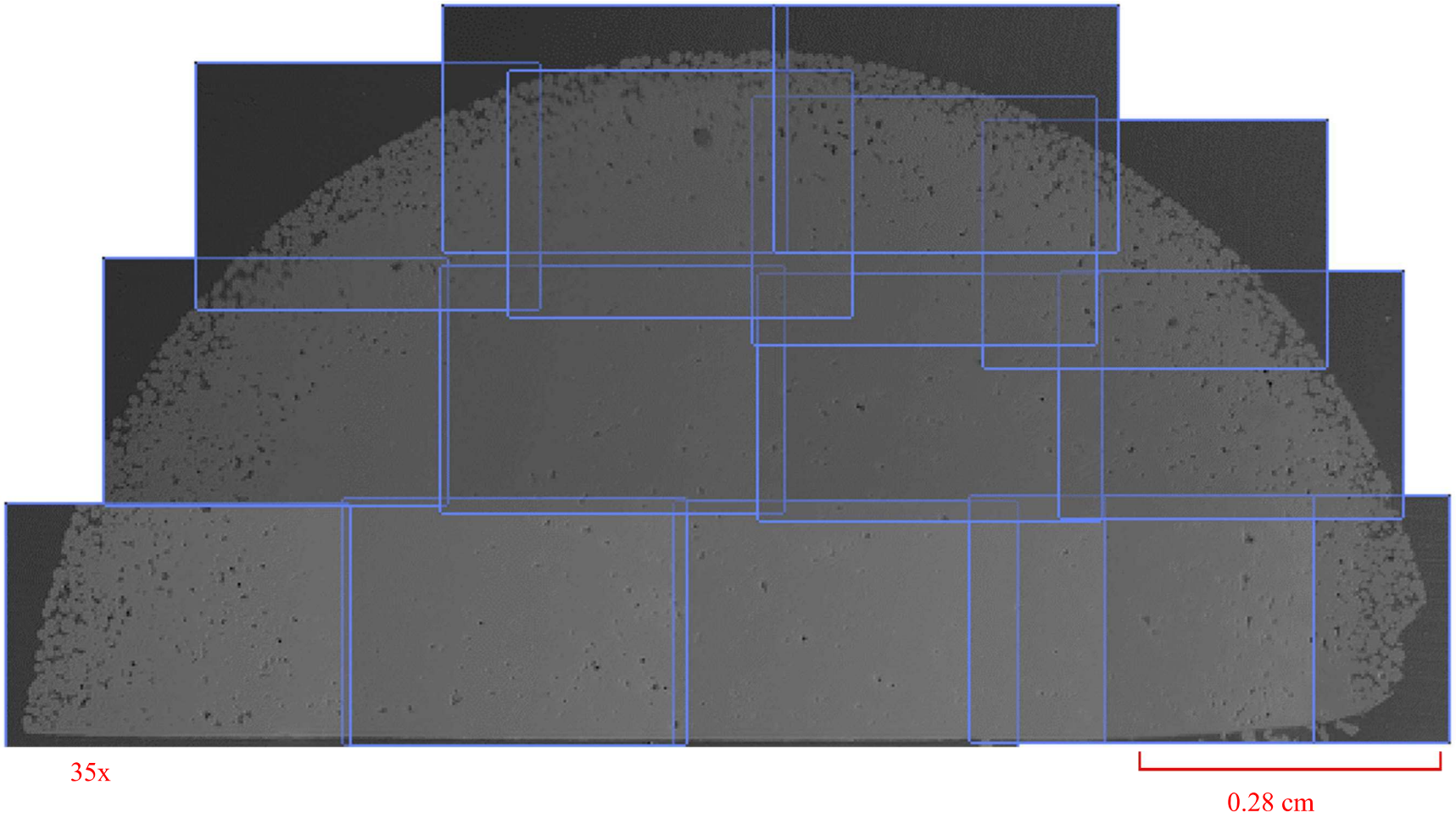

Figure 30: Radial cross-section image mesh compilations in mosaic, with each individual image computed with a magnification of 35x.

Figure XX shows the cropped selection v. cropped and highlighted porosity of the same image from a radial cross-section for comparison.

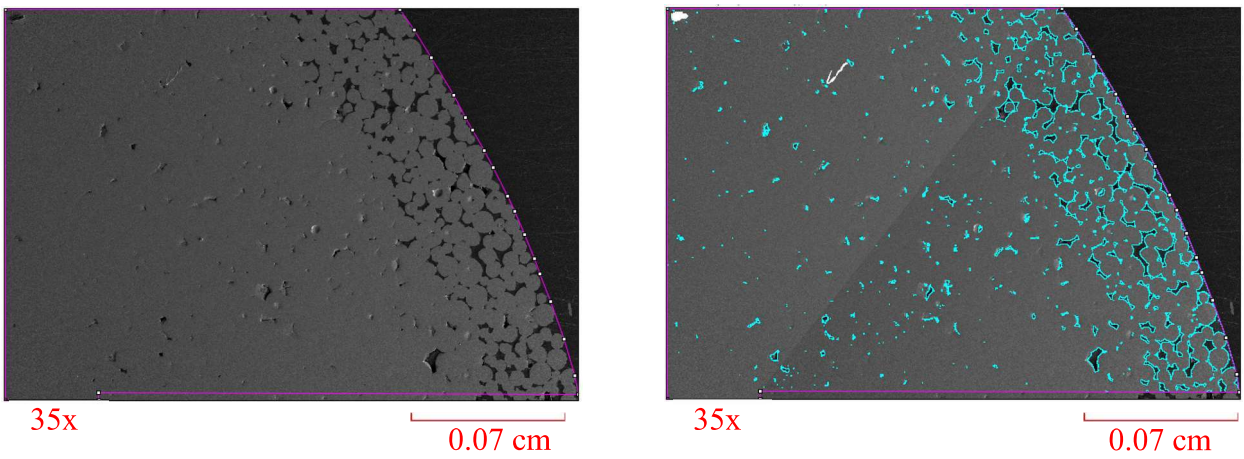

Figure 31: Cropped image excluding background selected in purple (left), the same image showing the selected measured area along with ImageJ computed porosity in blue (right).

The epoxy background outside of the boundaries of the cross-section of each image was cropped out of the area analyses to only include the copper and porosity within the cross-sectional area. Copper appeared in a light grey color on the images and porosity appeared in black or a dark shade of grey. Images were analyzed for porosity individually. After cropping each image, the surface area was calculated through the ImageJ scale set from pixels to cm. Any large scratches on the cross-section would appear dark and ImageJ considered these as porosity, which were redacted by shading in these scratches to blend with the copper threshold color and not be considered porosity.

One challenge that was overcome manually was the individual and effective editing of each image attributing to midplane cross-sections. Polished epoxy mounted pellet cross-sections were coated with carbon in a way that there could be as much of an even coat as possible. Carbon coating of pellet mounts was adjusted and improved, considering the uneven polished state of each epoxy sample. This resulted in SEM images with varying contrast and brightness. Some pores were observed to be more visually sharp than others in images due to the varying degree of depth and

size of pores, which contributed to the varying degree of carbon coating and SEM image resolution.

Pores analyzed and computed for area size through ImageJ consisted of conglomeration of connected pores along the cross-sectional surface area. ImageJ would dismiss singular spheres, or a conglomeration of spheres surrounded by porosity and included them as porosity. This was solved by creating a 2-bit white line connecting the Cu sphere conglomeration surrounded by porosity to the nearest morphed Cu conglomeration. Editing was also done when carbon coating debris appeared on the pellet surface during coating, the debris was edited out of the image so ImageJ would not consider it porosity. A separate command was arranged for ImageJ to trace the porosity detected and measured with a 1bit neon purple or neon blue line. This assisted in visualizing and assuring that the program was properly measuring all the visible porosity, and not including any copper in the measurements (Figure 31).

CHAPTER 04

RESULTS

Table 5. Copper Samples Produced at 1065°C using the Unpacked Bed Method

Table 5: Sintering results from unpacked Cu powder pellets including mass (g), green density (g/cm^3), sintered density (g/cm^3), open porosity (%) and open porosity error (%).

Sample ID	Sintering Time (h)	Mass (g)	Green Density (g/cm^3)	Sintered Density (g/cm^3)	Open Porosity (%)	Open Porosity Variation (%)
1.1	1	5.46	4.78	5.25	23.75	0.10
1.2	1	5.47	4.79	5.31	23.07	0.09
2.1	2	5.47	4.80	5.84	21.76	0.16
2.2	2	5.47	4.80	5.78	24.70	0.12
3.1	3	5.47	4.80	5.71	21.10	0.04
3.2	3	5.47	4.80	5.95	18.77	0.13
4.1	4	5.48	4.80	6.32	18.98	0.33
4.2	4	5.47	4.80	5.91	20.90	0.09
6.1	6	5.47	4.80	NA	20.06	0.06
6.2	6	5.47	4.80	5.79	14.39	5.81
12.1	12	5.47	4.80	6.42	16.17	0.07
12.2	12	5.46	4.79	6.15	15.38	0.17

Copper sintering was performed following the procedures outlined in Chapter 3. As noted, the objective was not to sinter fully-dense metal but to create a sequence of porous samples under well-defined conditions to facilitate model validation by other researchers. It was intended for the pre-sintering preparation and subsequent progression of sintering conditions to produce samples with changing porosity. In other words, the objective was to “sinter poorly” (not to 100% density) in a manner that would produce time-dependent changes.

Table 5 presents a summary of the final set of sintering tests performed using the unpacked sintering method developed here. The parameters and sintering conditions for each sample are presented. This chapter describes the results in further detail of this table, and conveys this data a average measurements per dwell time. Section 4.1 presents the sequence of discovery using conventional pressing and binders that eventually led to the development of the unpacked bed sintering approach. Section 4.2 presents the density and porosity results from the samples in table as an average of pellets dwelled for the same amount of time. Section 4.3 presents the images collected from the samples and the corresponding porosity values measured using ImageJ.

4.1 Summary of Sintering Method Development

Different experimental methods and techniques were applied with the progression of results in the first two phases of this study. The focus for obtaining sintered pellet structures with a more homogenous volumetric porosity was initially in the palletization process, while only adjusting temperature and dwell time in the sintering phase. Initial sintering trials were conducted on pellets varying in production pressure. Table 6 shows the pressure quantities used to produce various pellets and the ID number used as reference for each value. With progressing sintering trials with the varying pressure quantities applied, observations and pellets stability relied on pellets produced with 150.8 MPa. These pellets had the least amount of geometric green density, had enough structure stability to measure as well as handle accordingly for sintering, and morphology was simple to track post-sintering.

Table 6: Force applied during palletization process and the number assigned to each amount.

Pressure Force Applied (MPa)	ID
150.8	P1
164.2	P2
177.6	P3
191.0	P4
201.1	P5
217.8	P6

Porosity results from pelletization and sintering without the use of oil as a lubricant prior to compression were not reliable. These pellets had a higher initial density and higher amounts of pressure concentrated along certain pressure gradients which would later densify the sample further upon sintering. Sintered pellets showed a near complete densification along the center with porosity concentrating along a very strict boundary border around the edges. This could be seen in SEM images such as shown in Figure 31. Upon adding the oil to the center of the powder, porosity uniformity increased along both cross-sections of P1 pellets when sintering temperatures were between 1065°C and 1075°C for a dwell time over 1 h.

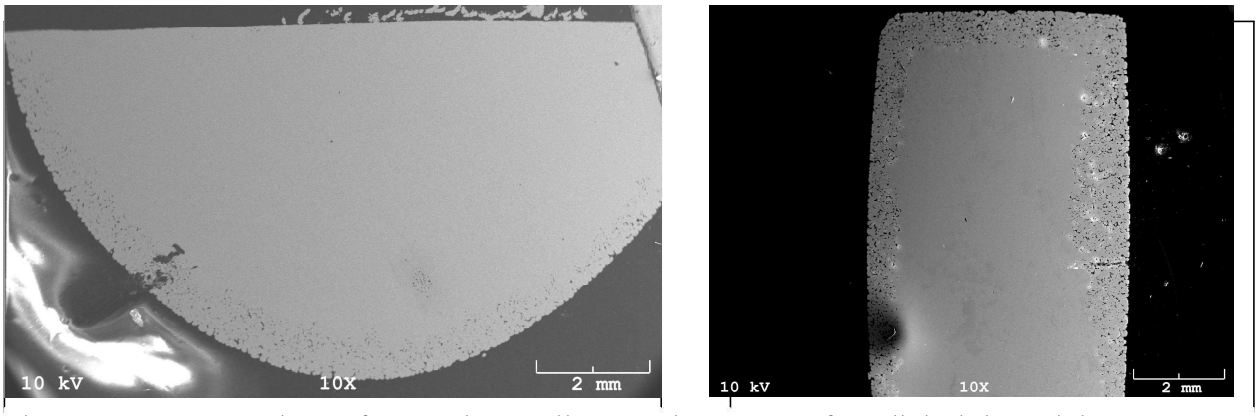

Figure 32: Cross-sections of pressed Cu pellet sample (10x). Left: radial, right: axial.

With the addition of oil in the spherical powder prior to sintering, Cu spheres compacted with less friction during the application of pressure, and the second phase of this study was initiated. The addition of oil in the center of the pellet altered sintering results, requiring the sintering samples to reach a higher temperature than previous trials, closer to the melting point of Cu to achieve a homogenous porosity profile. Before applying oil in the powder prior to palletization of P1 pelletization production, pellet samples showed signs of homogeneity at sintering temperatures between 890°C and 900°C for a dwell of 10 min. After adding oil in the powder, pellets resulted unstable after sintering at temperatures 925°C, 1025°C, 1065°C for a dwell time of 1 h. Pellets only started to stabilize at a temperature of 1075°C at a minimum dwell time of 1 h. Upon increasing dwell time, the pellets showed more stability. Figure 32 shows the progression pellet sintering trials from left to right according to sintering temperature and dwell time.

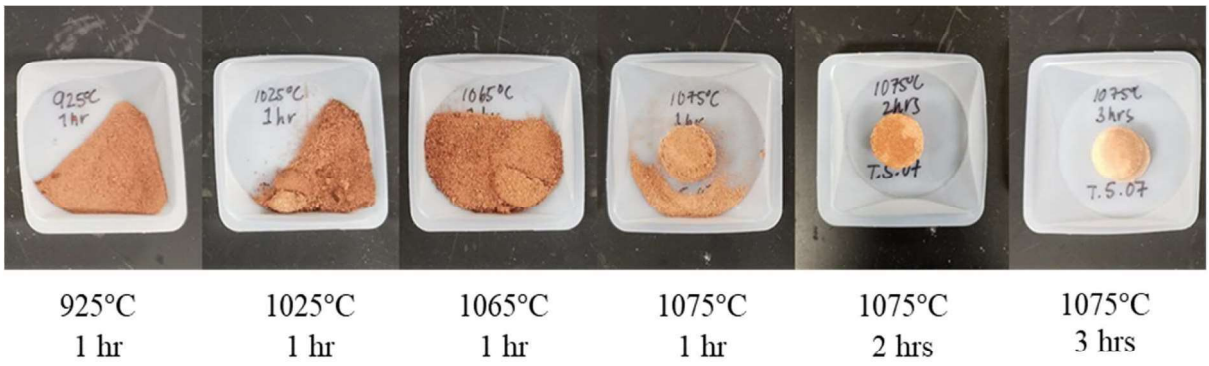

Figure 33: Progression of pellet stability from sintering results after implementing oil in Cu powder prior to palletization.

Figure 33 showed sintering temperatures of interest of 1065°C and 1075°C. Further sintering trials were conducted at these temperatures to compare densification. Densification comparisons were done with P1 pellets at temperatures 1075°C and 1065°C for dwell times of 1 h, 2 h, 3 h and 6 h. Density calculations were conducted of post sintered pellets through dimension measurements and Archimedes' immersion method. A sintering temperature of 1065°C was

optimal to analyze density and porosity with increasing dwell time. Pairs of pellets were produced and sintered with the same parameters. Sintered pellets that resulted in a fragile state, with spheres not having morphed and breaking off of the pellet structure were not reported on tabulated results. These pellets resulted in uncertain measurements due to the unstable volumetric structure.

4.2 Density and Porosity Measurements from Unpacked Copper Sintering at 1065°C

Pressed lubricated sintered pellet results showed stable results for dwell times of 3 h, 4 h, 6 h, and 12 h. Results for pellets sintered for a dwell time of 1 h and 2 h were not reported due to the unstable structure of the pellets after being sintered. The pressed lubricated pellet sintered for 1 h fell apart upon contact, and the pellet sintered for 2 h showed more stability post-sintering, but spheres continued to fall off the pellet structure while taking measurements. SEM images of the radial cross-section of the pellet sintered for 2 h is shown in Figure 34.

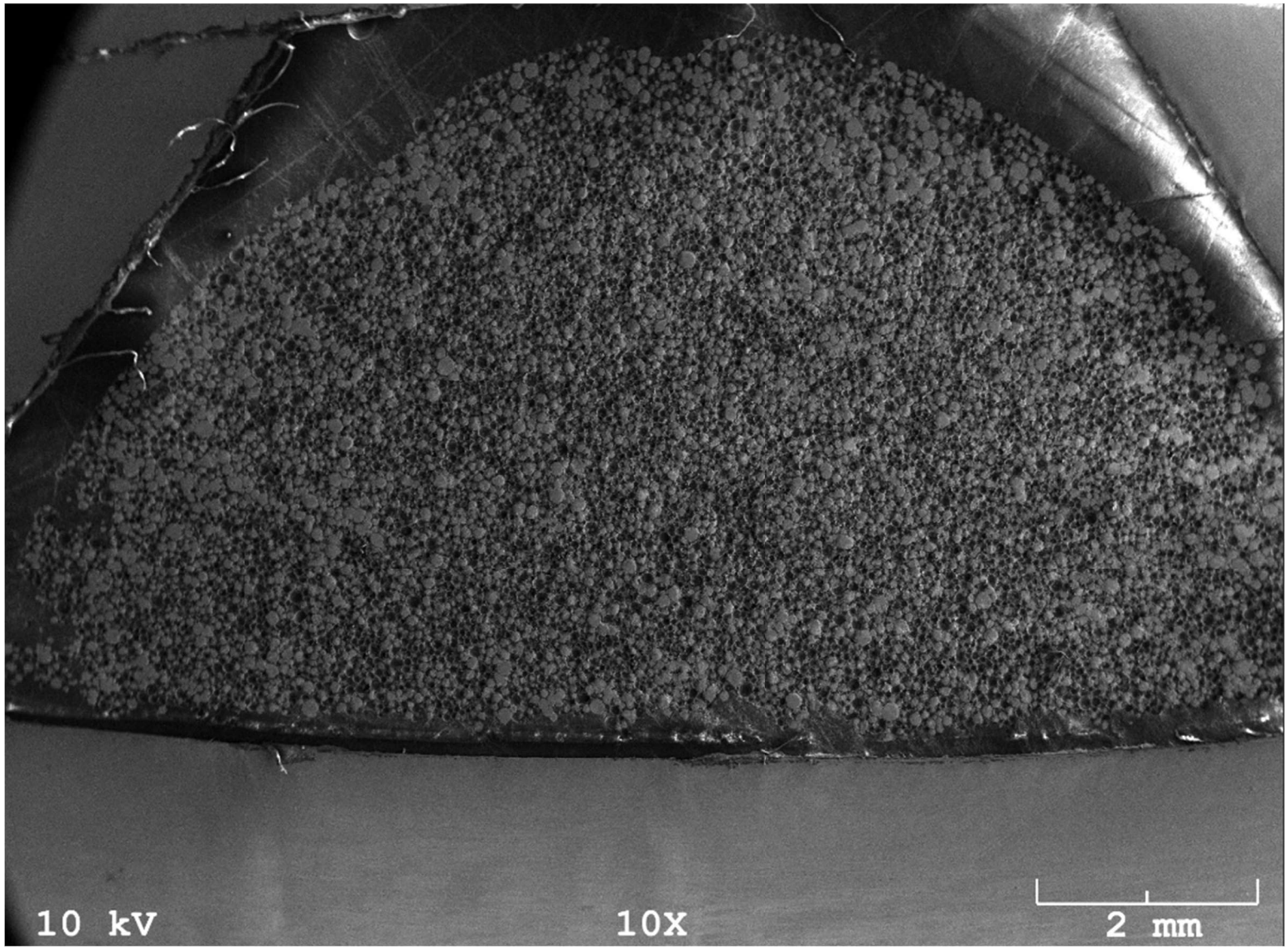

Figure 34: Radial cross-section of pressed lubricated pellet sintered for 2 h.

The average overall porosity measured in units of area by ImageJ was compared to the individual calculated size of pores in the image. Once this process was completed for each image in the mesh set of images captured for each cross-section, the porosity and surface area of all the images was added to compare and compute to the porosity of the entire cross-sectional surface area. These values were recorded in a table and compared to those of sintered geometrical and immersed density measurements. ImageJ executed the calculation of image porosity with a summary of calculations including porous area in cm^2 and porosity percentage compared to the image area. Additionally, porosity computational commands also produced a table to the area measurements of each pore analyzed.

Lose powder pellets required less time to prepare and showed more stability post-sintering. This allowed results to be obtained from pellets sintered for 1 h and 2 h, whereas pressed sintered pellets resulted too fragile for these dwell times and could not be measured properly since they would fall apart in the attempt. Lose powder pellets were expected to have a lower density value for pre and post- sintering stage calculations. More values were included in the following tables describing the porosity and density outcomes of sintered lose powder pellets as these incorporate the focus of this project. Additional values seen include density and uncertainty values in units of g/cm^3, and porosity percentage calculations for each density calculation method derived from respective density percentages and denoted by GGD%, SGD%, and IMD%. Graphs were tabulated from this information. Uncertainty values for GGD were not calculated since this step did not include enough data to derive such calculations for sintered lose powder pellets.

Table 7: Calculated density (GGD, SGD, AIMD) values, respective variation percentage, and theoretical density percentages of pellets sintered at varying hours relative to the density of Cu.

	Green			Sintered					
Pellet ID	**GGD (g/cm^3)**	**Sample Variation % (GGD)**	**GGD % T. D.**	**SGD (g/cm^3)**	**Sample Variation % (SGD)**	**SGD % T. D.**	**AIMD (g/cm^3)**	**Sample Variation % (AIMD)**	**AIMD % T. D.**
1.1	4.78	0.02	53.51	5.25	1.70	58.77	5.88	0.03	65.72
1.2	4.79	0.02	53.60	5.31	1.20	59.35	5.82	0.02	65.07
2.1	4.80	0.02	53.69	5.84	1.63	65.30	6.16	0.03	68.90
2.2	4.80	0.02	53.67	5.78	8.52	64.63	5.94	0.03	66.50
3.1	4.80	0.02	53.68	5.71	5.80	63.90	6.27	0.02	70.09
3.2	4.80	0.02	53.70	5.95	4.31	66.52	6.26	0.03	70.05
4.1	4.80	0.02	53.70	6.32	6.29	70.64	6.72	0.06	75.12
4.2	4.80	0.02	53.68	5.91	1.89	66.15	6.45	0.02	72.12
6.1	4.80	0.02	53.68	NA	NA	NA	6.44	0.02	72.00
6.2	4.80	0.02	53.66	5.79	0.51	64.71	6.67	1.05	74.66
12.1	4.80	0.02	53.66	6.42	1.95	71.77	6.80	0.02	76.04
12.2	4.79	0.02	53.59	6.15	8.23	68.83	6.71	0.04	75.06

Table 8: Average Sintering results form unpacked Cu powder pellets including mass (g), green density(g/cm^3), sintered density (g/cm^3), open porosity (%) and open porosity error (%)values per dwell time hour from table 7.

	Green			Sintered					
Time (h)	**GGD (g/cm^3)**	**Sample Variation % (GGD)**	**GGD % T. D.**	**SGD (g/cm^3)**	**Sample Variation % (SGD)**	**SGD % T. D.**	**AIMD (g/cm^3)**	**Sample Variation % (AIMD)**	**AIMD % T. D.**
1	4.79	0.02	53.55	5.28	1.45	59.06	5.85	0.02	65.39
2	4.80	0.02	53.68	5.81	5.07	64.97	6.05	0.03	67.70
3	4.80	0.02	53.69	5.83	5.06	65.21	6.26	0.02	70.07
4	4.80	0.02	53.69	6.11	4.09	68.40	6.58	0.04	73.62
6	4.80	0.02	53.67	5.79	0.51	64.71	6.56	0.53	73.33
12	4.79	0.02	53.63	6.29	5.09	70.30	6.75	0.03	75.55
		AVG ~0.02%			AVG ~3.54%			AVG ~0.11%	

Average GGD calculations in Table 8 indicated an estimated consistency, however, these values were a lose calculation of the actual result due to only having considered the mass of the powder and the dimensions occupied in the alumina cylindrical container. Subsequently, SGD and AIMD values also resulted in lower density percentages at all dwell times compared to pressed pellets. Lose powder pellets for every dwell time trial maintained a more consistent GGD% between 53.55% and 53.67%. SGD% and AIMD% average values showed an increasing density trend with each increasing dwell time, and higher differences at dwell times of 1 h and 6 h. At a dwell time of 6 h, SGD% values again decreased in values comparable to those calculated in dwell times of 3 h and 4 h. Density values calculated for the 12 h dwell time resulted in the highest values. SGD for pellets sintered for 12 h averaged a calculated value of 6.29 g/cm^3, and 70.30% dense compared to solid Cu. IMD calculations resulted in a density value higher to that measured to derive the SGD, at a value of 6.75 g/cm^3, 75.55% of solid Cu. These observations can be noted in Figure 35.

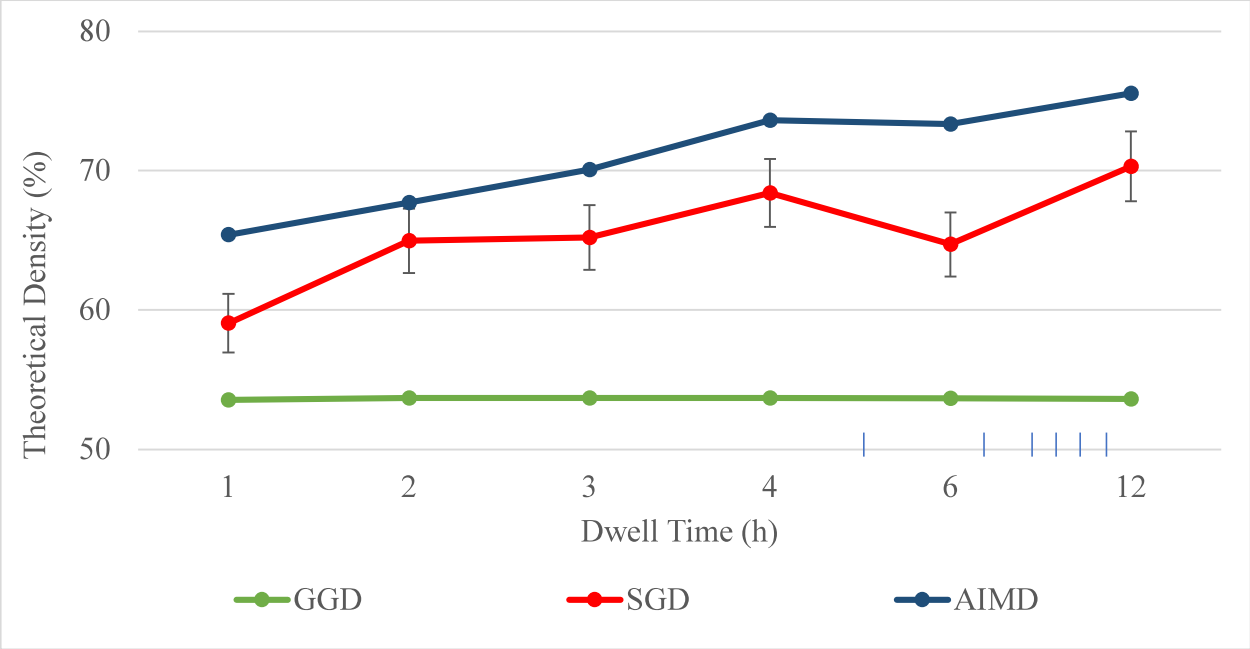

Figure 35: Average percentage values for green geometric density (GGD), sintered geometric density (SGD) and immersed method density (AIMD) as percent compared to Cu (8.94 g/cm^3).

The density measurements from lose powder sintered pellets showed the AIMD calculations to be more consistent and linear with increasing dwell time when compared to the calculations of the SGD. SGD was theorized to vary more due to the non-uniform porosity along the volume of the pellet structures. For all three phases of pellet production and sintering, the dwell time of 6hrs was observed to have a density that did not correlate to the expected increasing trend with increasing dwell time. ImageJ analysis was focused on the phase three sintered pellets due to the consistent density calculations reported in the previous graphs.

As the pellets densified with increasing temperatures, the porosity decreased, and pores became smaller in size. This pore densification progression resulted in interconnected and closed porosity within the volumetric space of the pellets. The measurements for closed porosity were calculated to have an understanding of how the pellets were densifying, in regard to the amount of open or closed porosity. A higher amount of open porosity would infer that the loose packed

Cu did not densify through the three stages of sintering but halted the densification process at the stages of neck formation and pore conglomeration. A higher amount of open porosity results in pellets with higher density, including isolated pores and more pellet stability. Open porosity data for average pellet dwell times is shown in table 9.

Table 9: Open porosity percent values for average pellet sintering dwell time, with respective variance percentage.

Time (h)	Open Porosity (%)	Variation (%)
1	23.41	0.09
2	23.23	0.14
3	19.93	0.09
4	19.94	0.21
6	17.22	2.93
12	15.78	0.12
		AVG ~0.60%

The results from open porosity calculations indicated that open porosity decreased with increasing dwell time, at an overall loss of 7.63%. The rest of the porosity in the sample was closed porosity. Figure 36 characterizes these results as a function of dwell time, and the corresponding function of linear open porosity loss rate of ~ -1.61% per average dwell time.

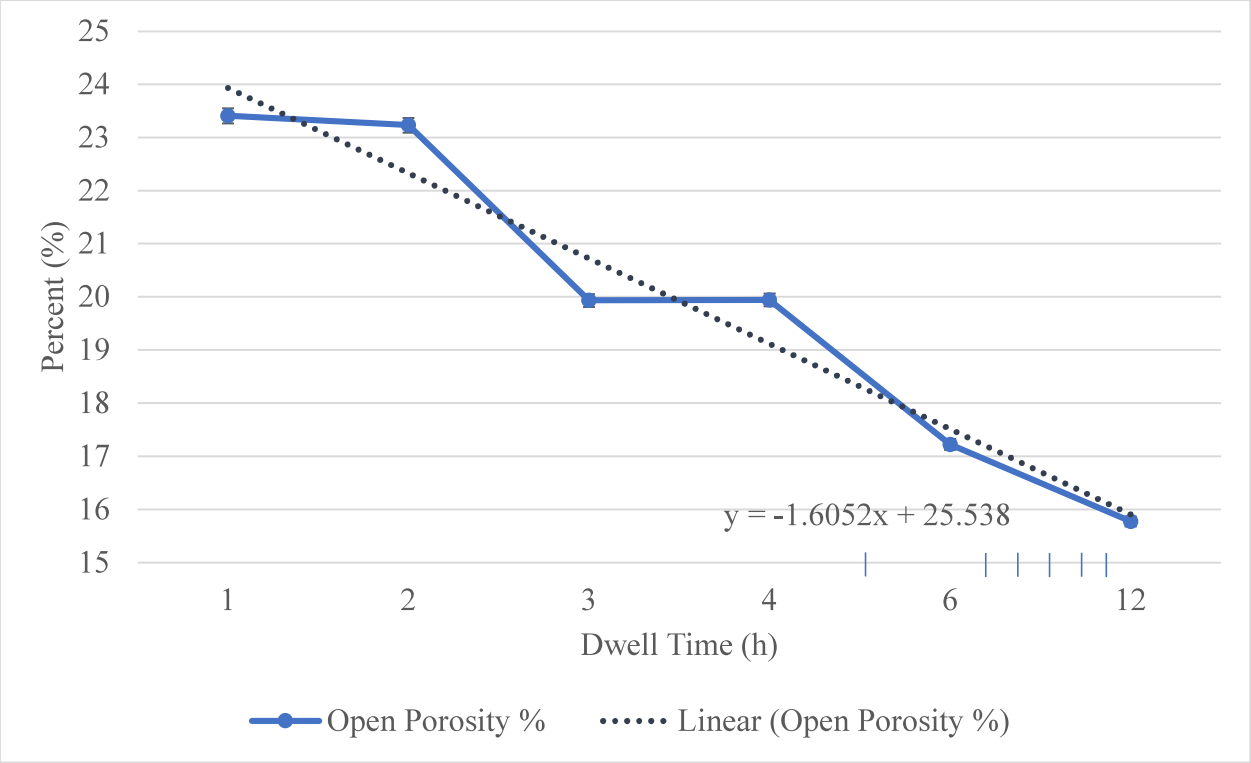

Figure 36: Open porosity percentage and linear open porosity percentage as a function of sintering dwell time.

It was projected from the open porosity percent in figure 36 that the porosity does not change significantly from dwell times of 1 h to 2 h. After this, open porosity decreased by ~3% at a dwell time of 3 h, and showed no significant change at a 4 h dwell. From 4 h to 12 h open porosity decreased in a near linear manner to a total of just under 16% open porosity.

4.3 Images and Porosity Area Fractions from Unpacked Copper Sintering at 1065°C

The following images (figures 37-58), show the resulting axial and radial cross-sections form the various sintering dwell times.

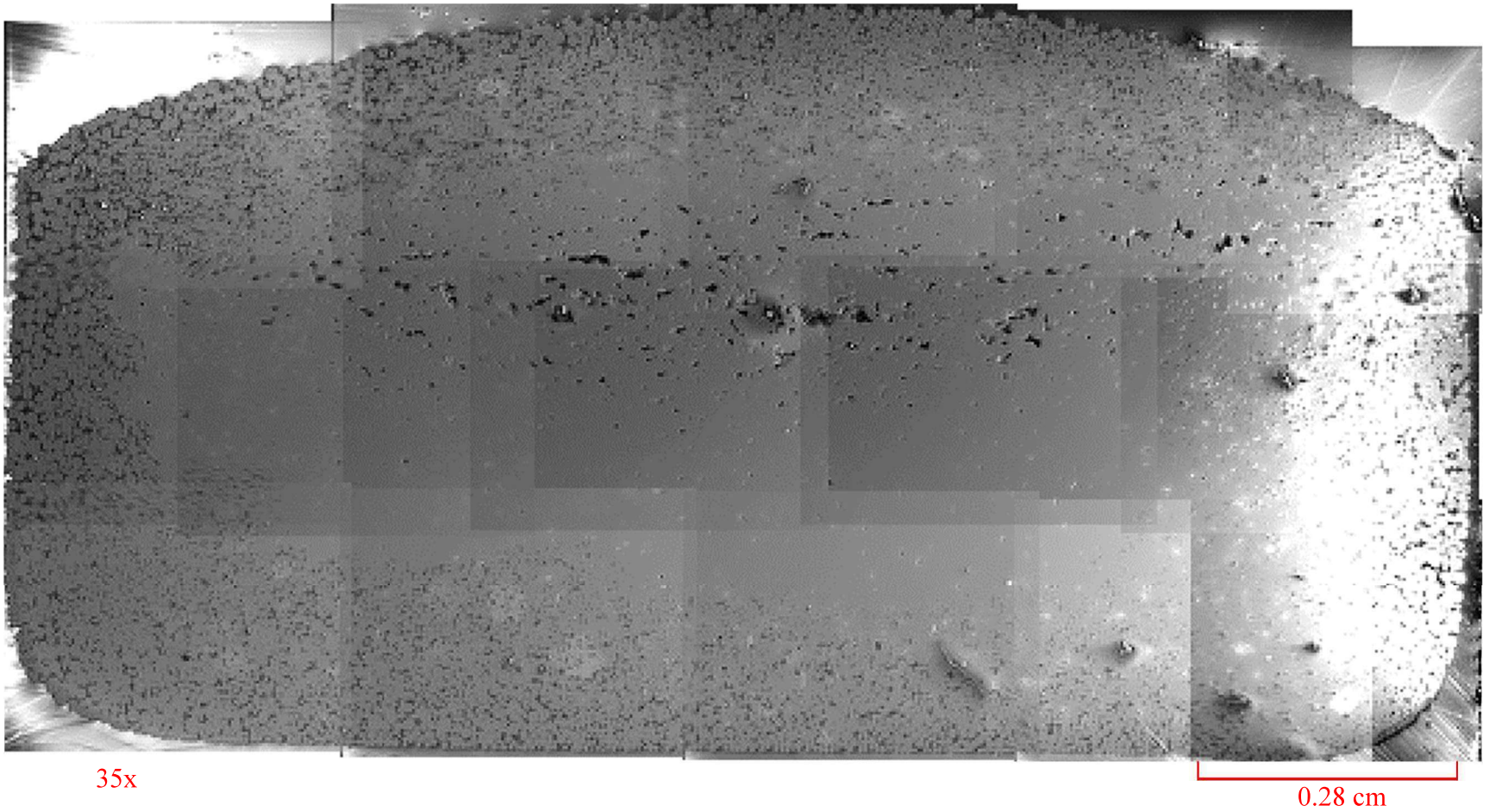

Figure 37: Pellet 1.1 Axial cross-section image mosaic sintered for 1 h.

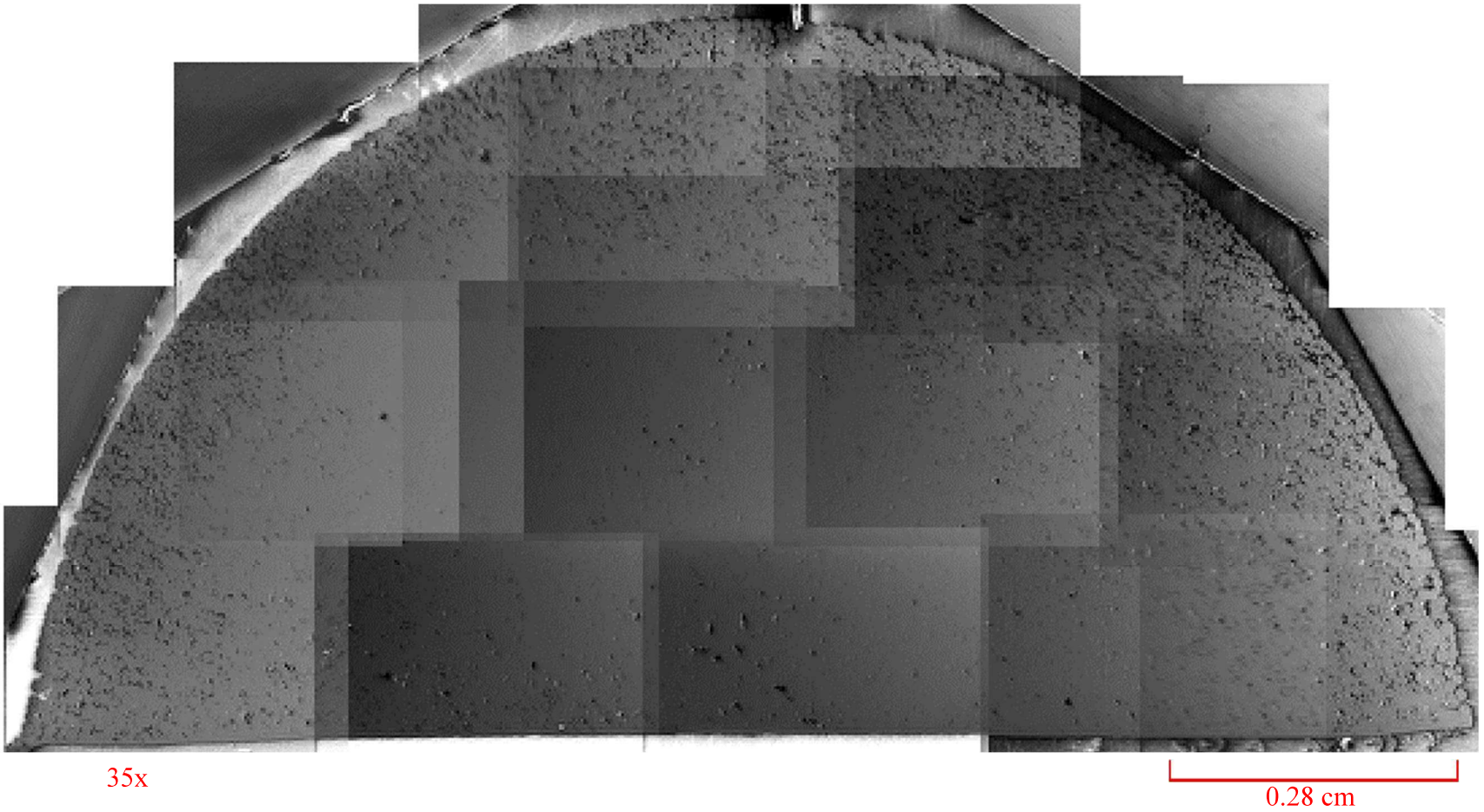

Figure 38: Pellet 1.1 radial cross-section image mosaic sintered for 1 h.

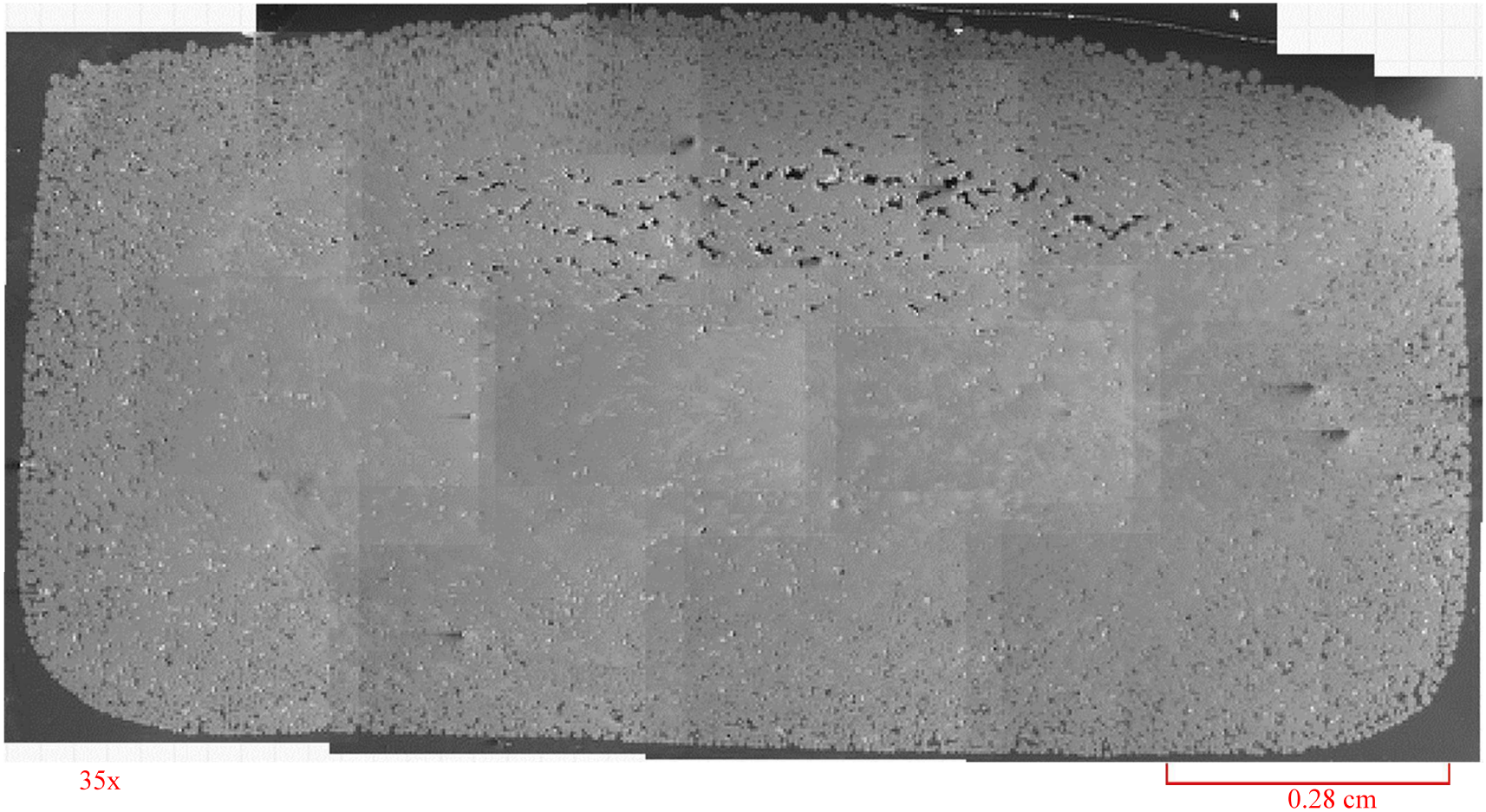

Figure 39: Pellet 1.2 Axial cross-section image mosaic sintered for 1 h.

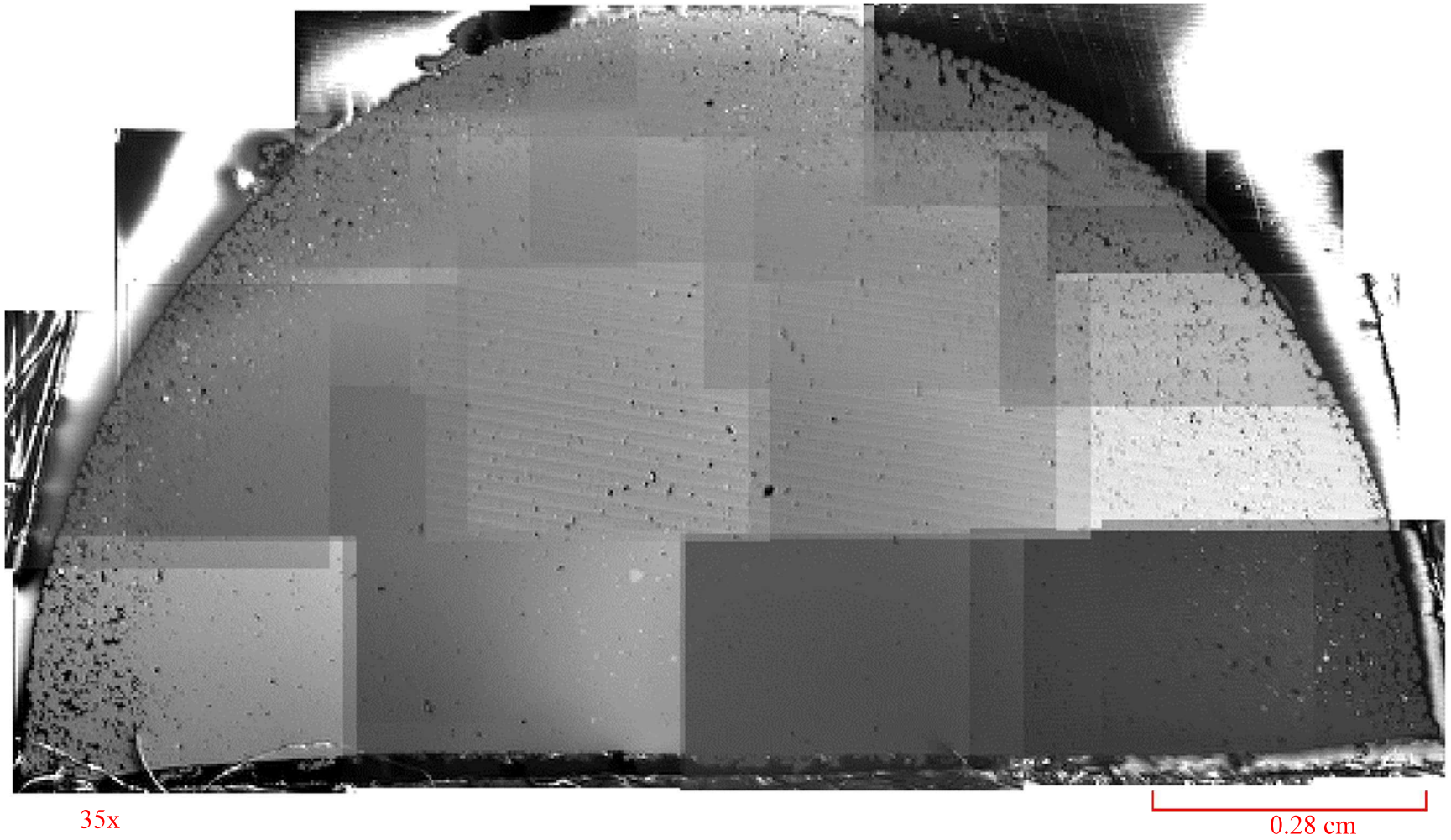

Figure 40: Pellet 1.2 Radial cross-section image mosaic sintered for 1 h.

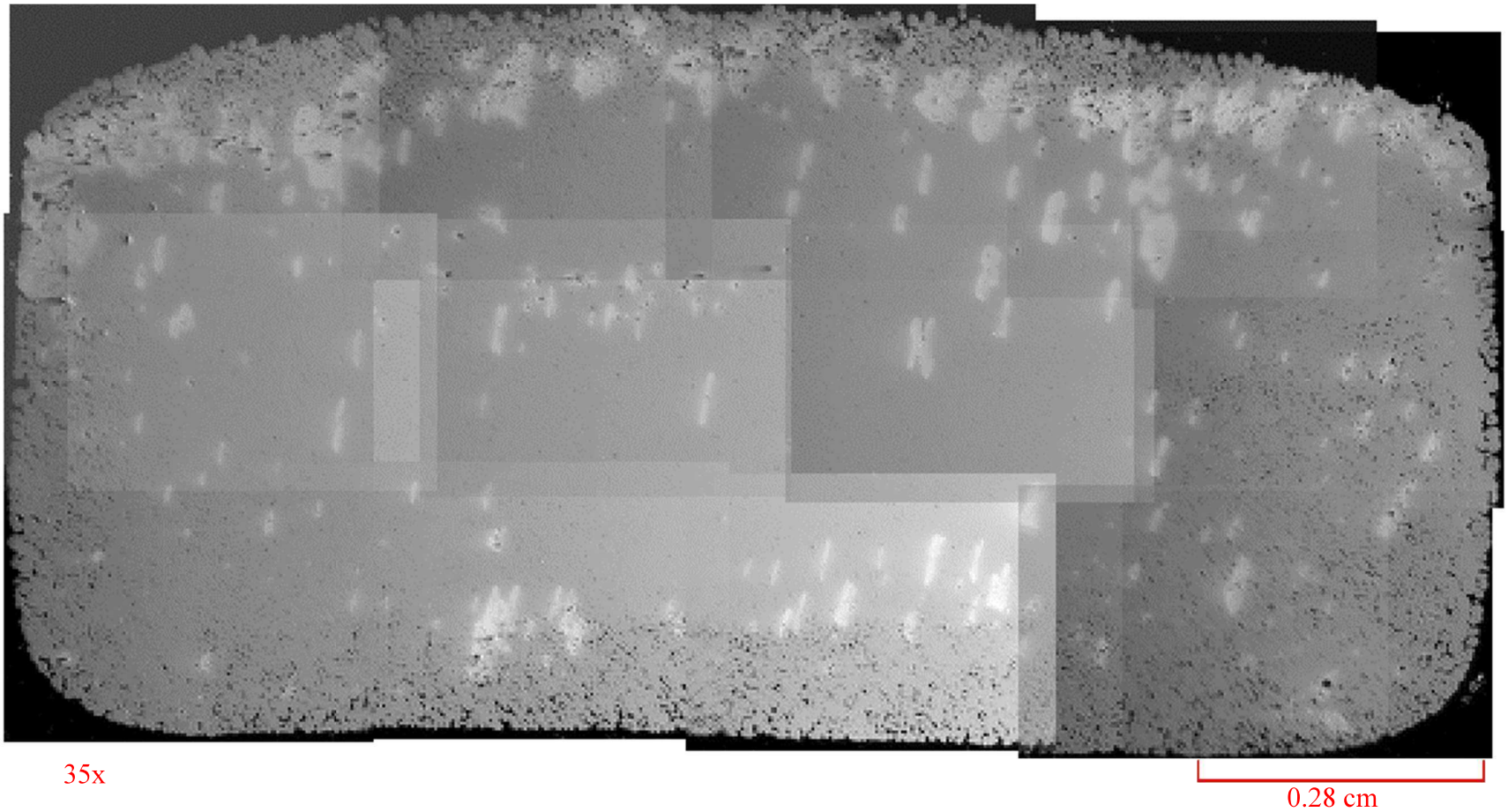

Figure 41: 2.1 Pellet 2.1 Axial cross-section image mosaic sintered for 2 h.

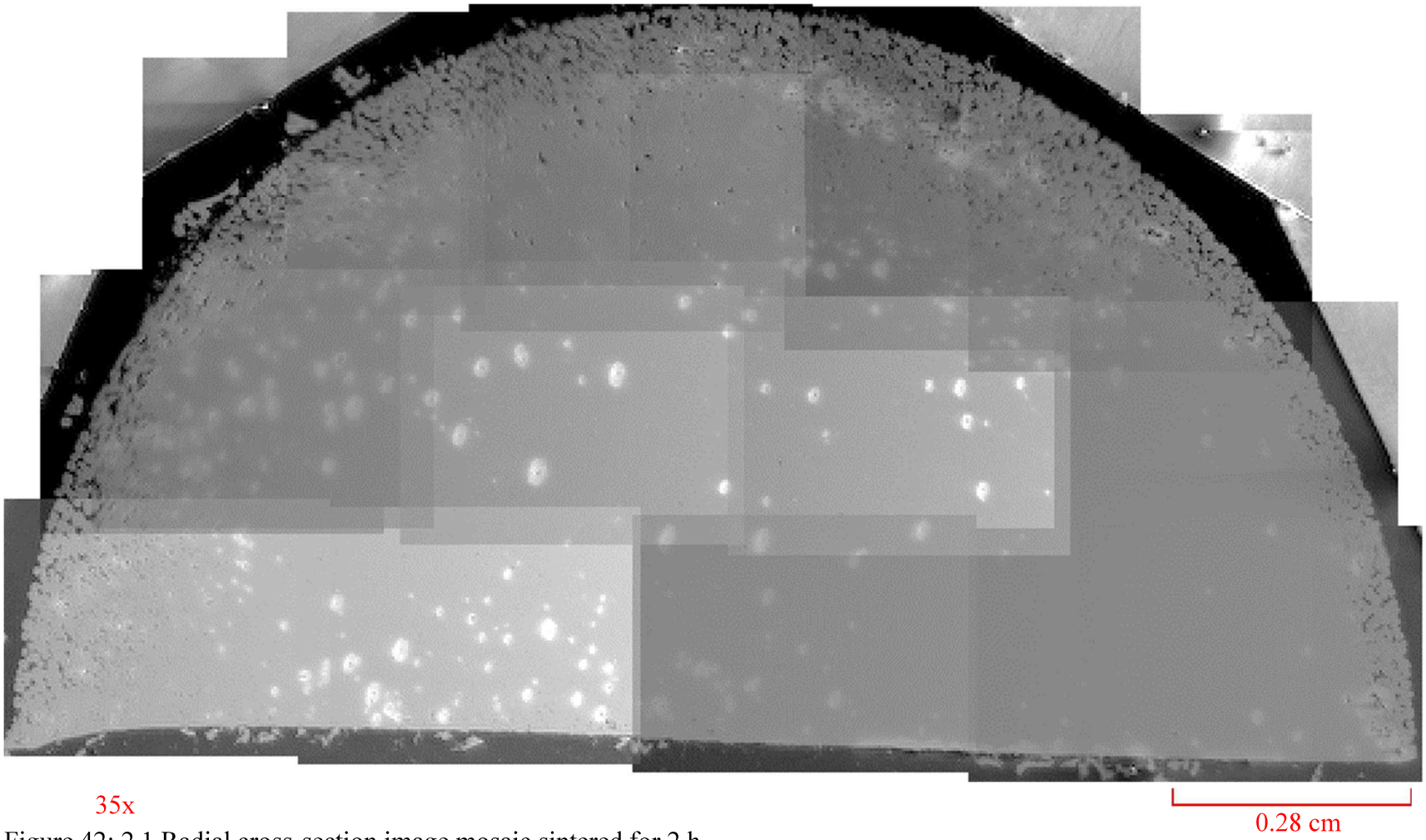

Figure 42: 2.1 Radial cross-section image mosaic sintered for 2 h.

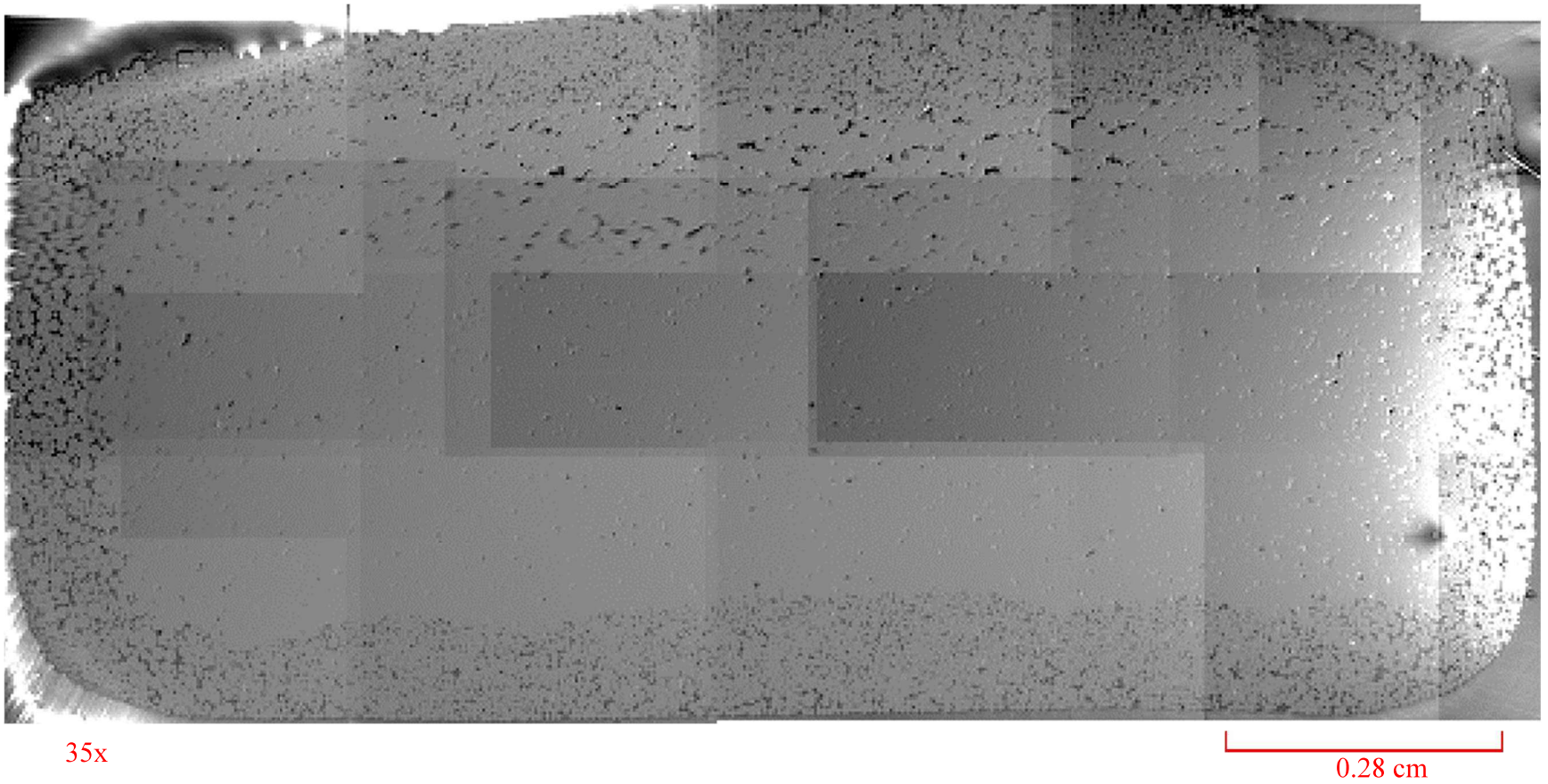

Figure 43: Pellet 2.2 Axial cross-section image mosaic sintered for 2 h.

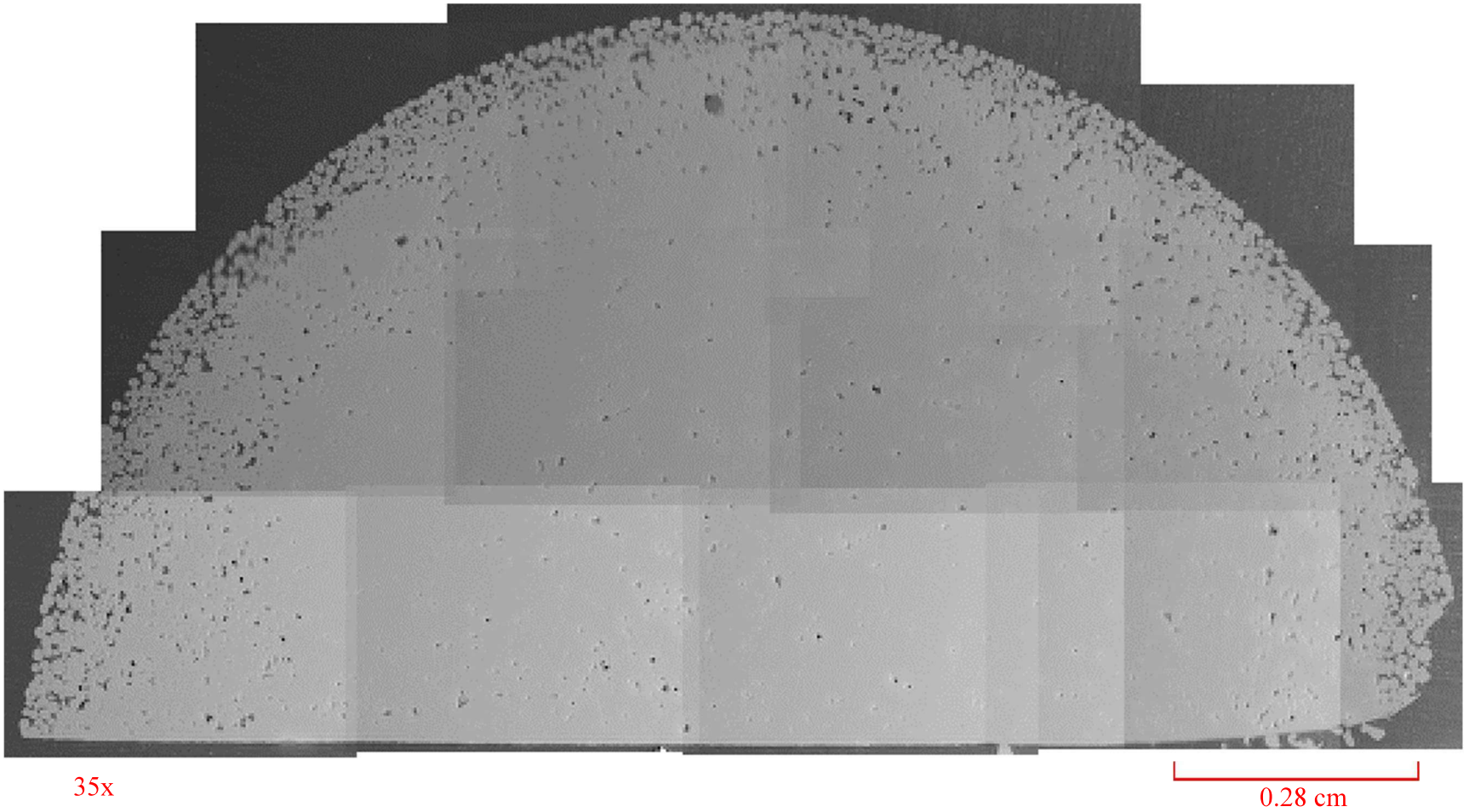

Figure 44: Pellet 2.2 Radial cross-section image mosaic sintered for 2 h.

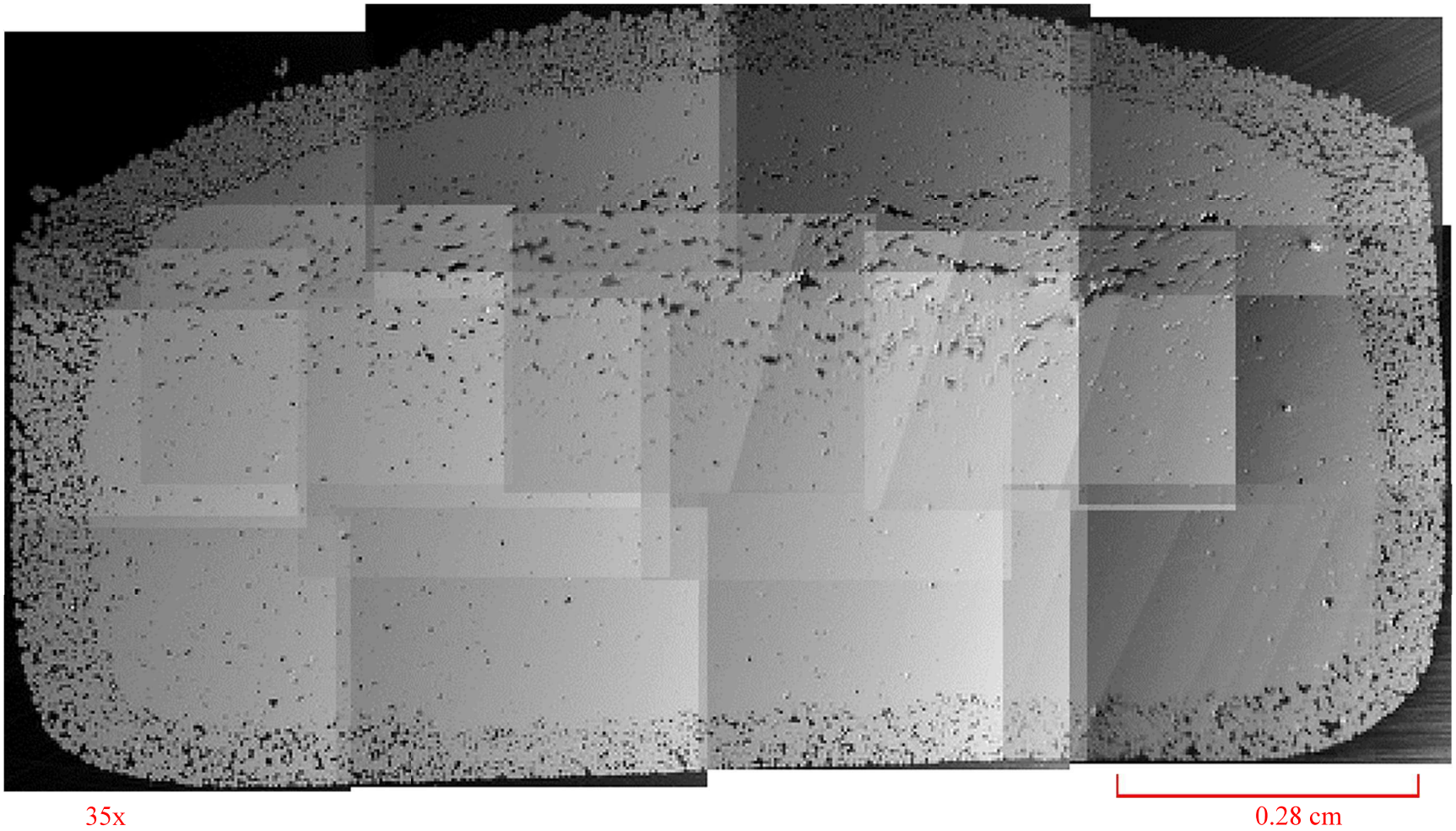

Figure 45: Pellet 3.1 Axial cross-section image mosaic sintered for 3 h.

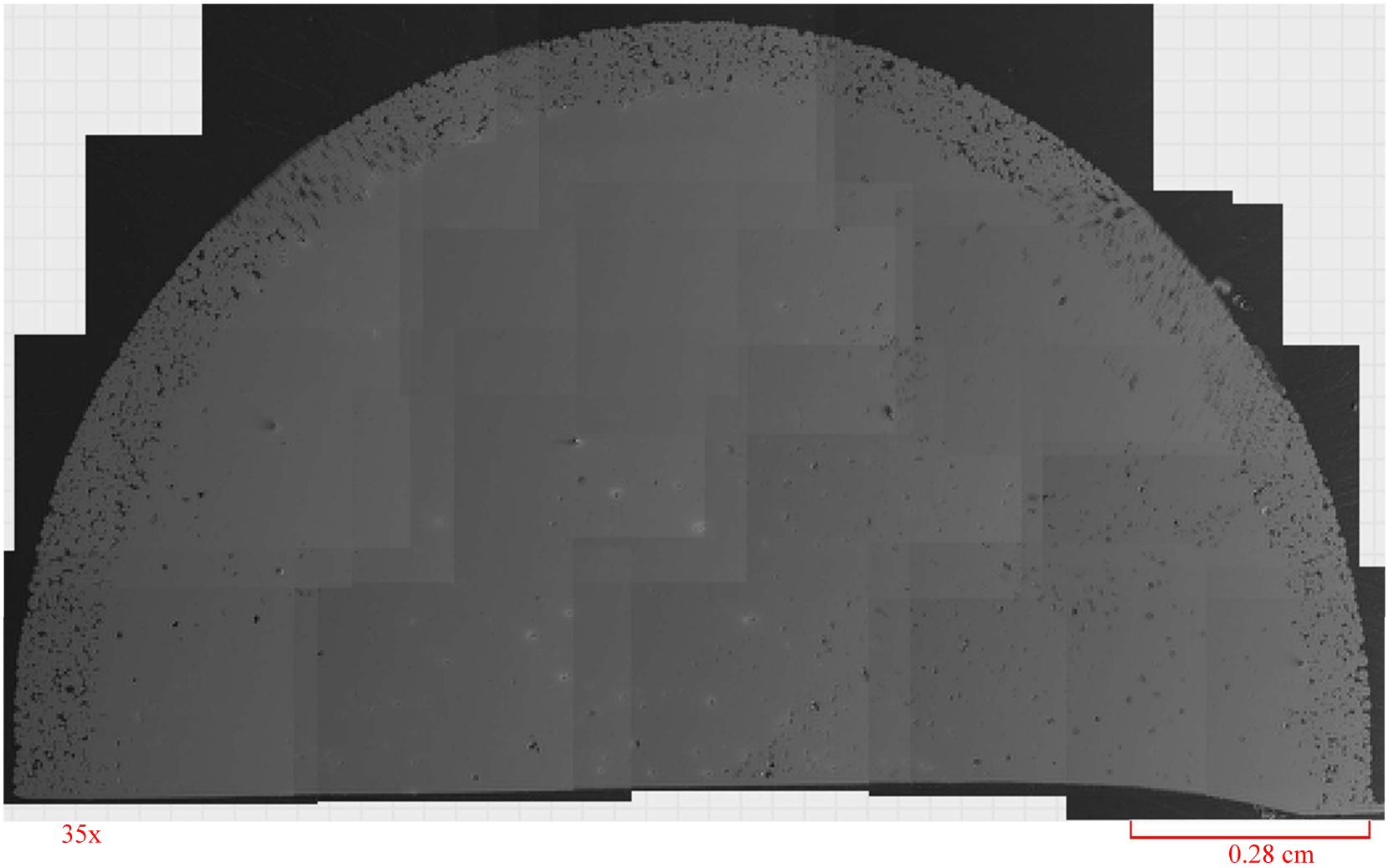

Figure 46: Pellet 3.1 Radial cross-section image mosaic sintered for 3 h.

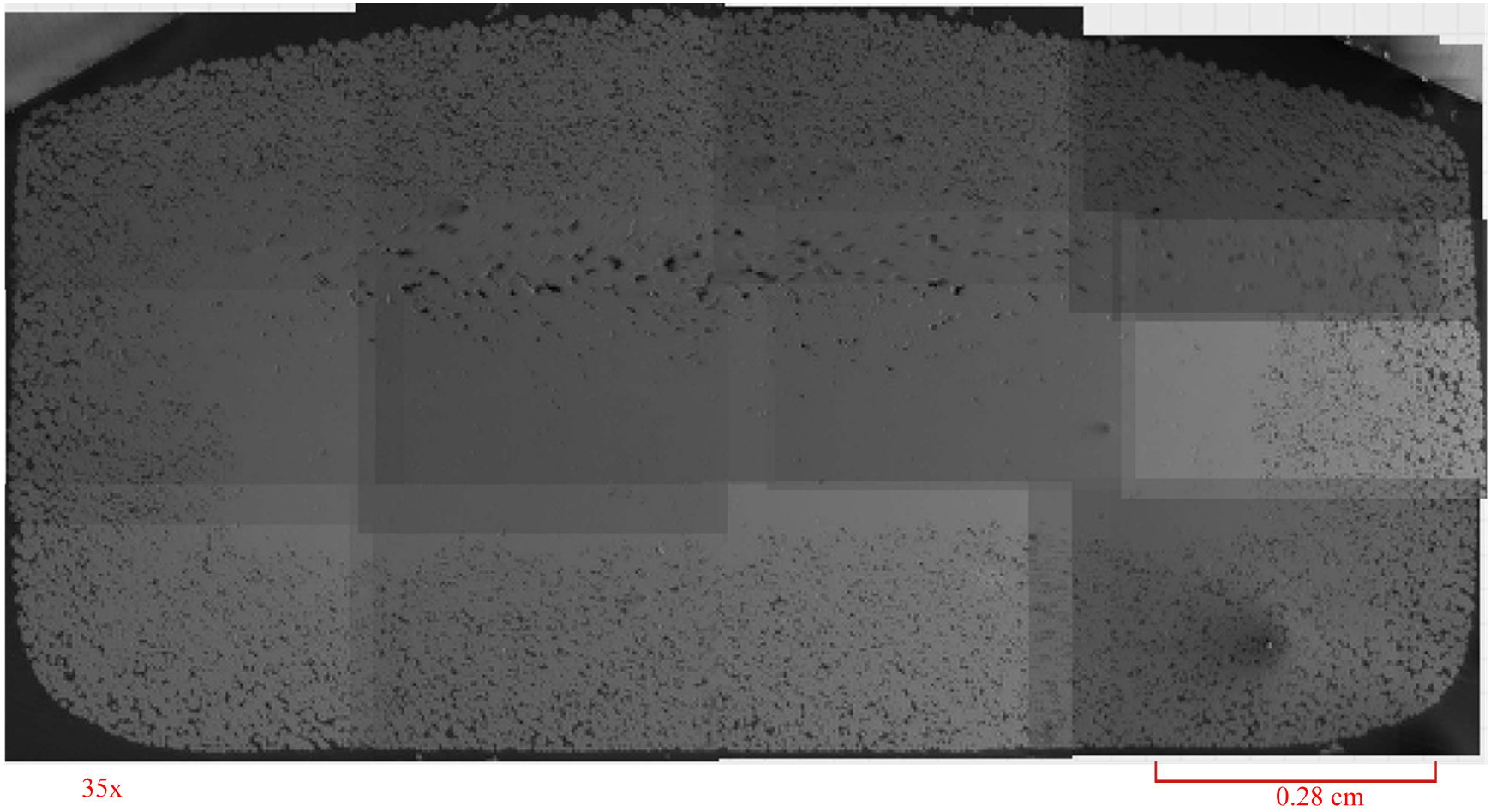

Figure 47: Pellet 3.2 Axial cross-section image mosaic sintered for 3 h.

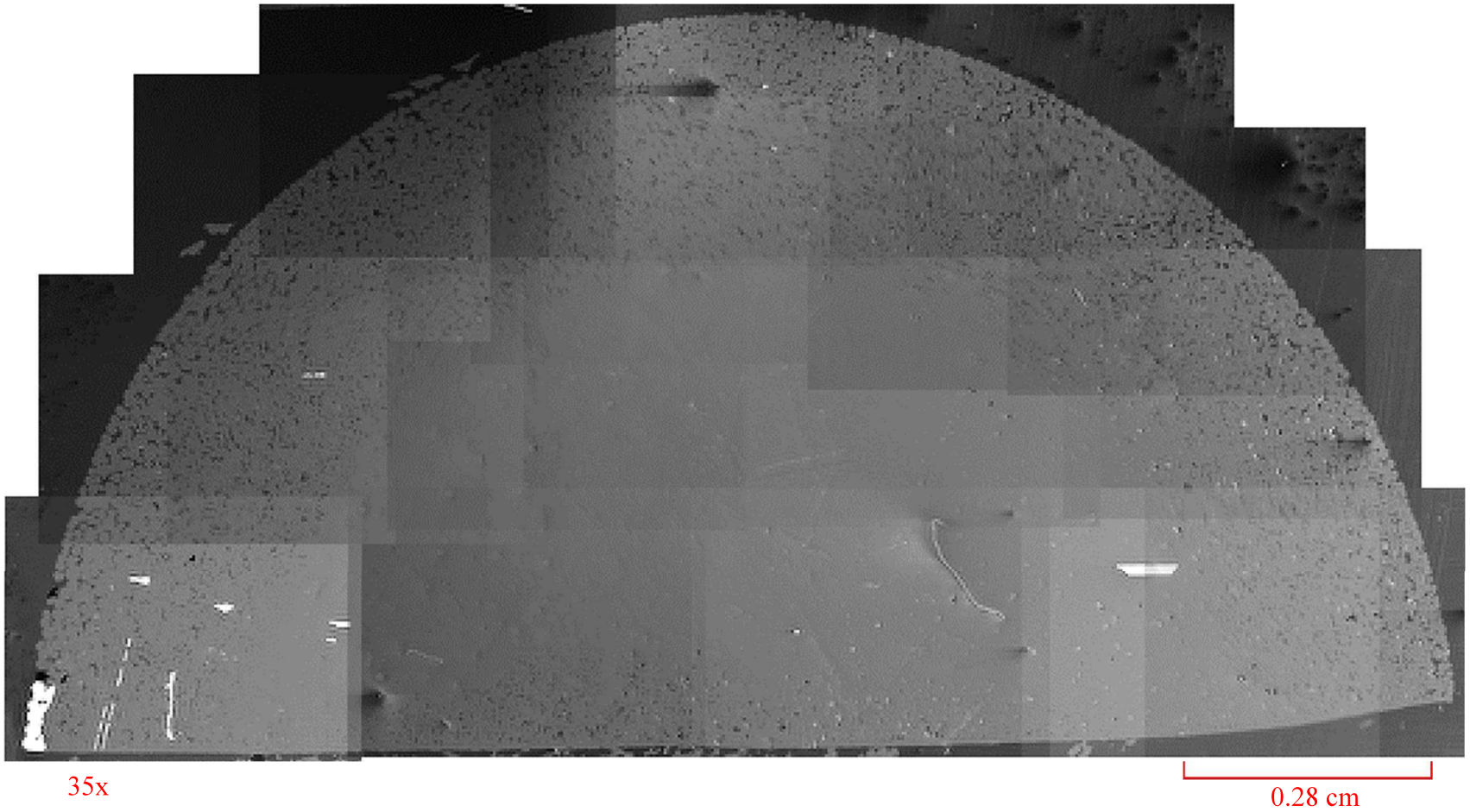

Figure 48: Pellet 3.2 Radial cross-section image mosaic sintered for 3 h.

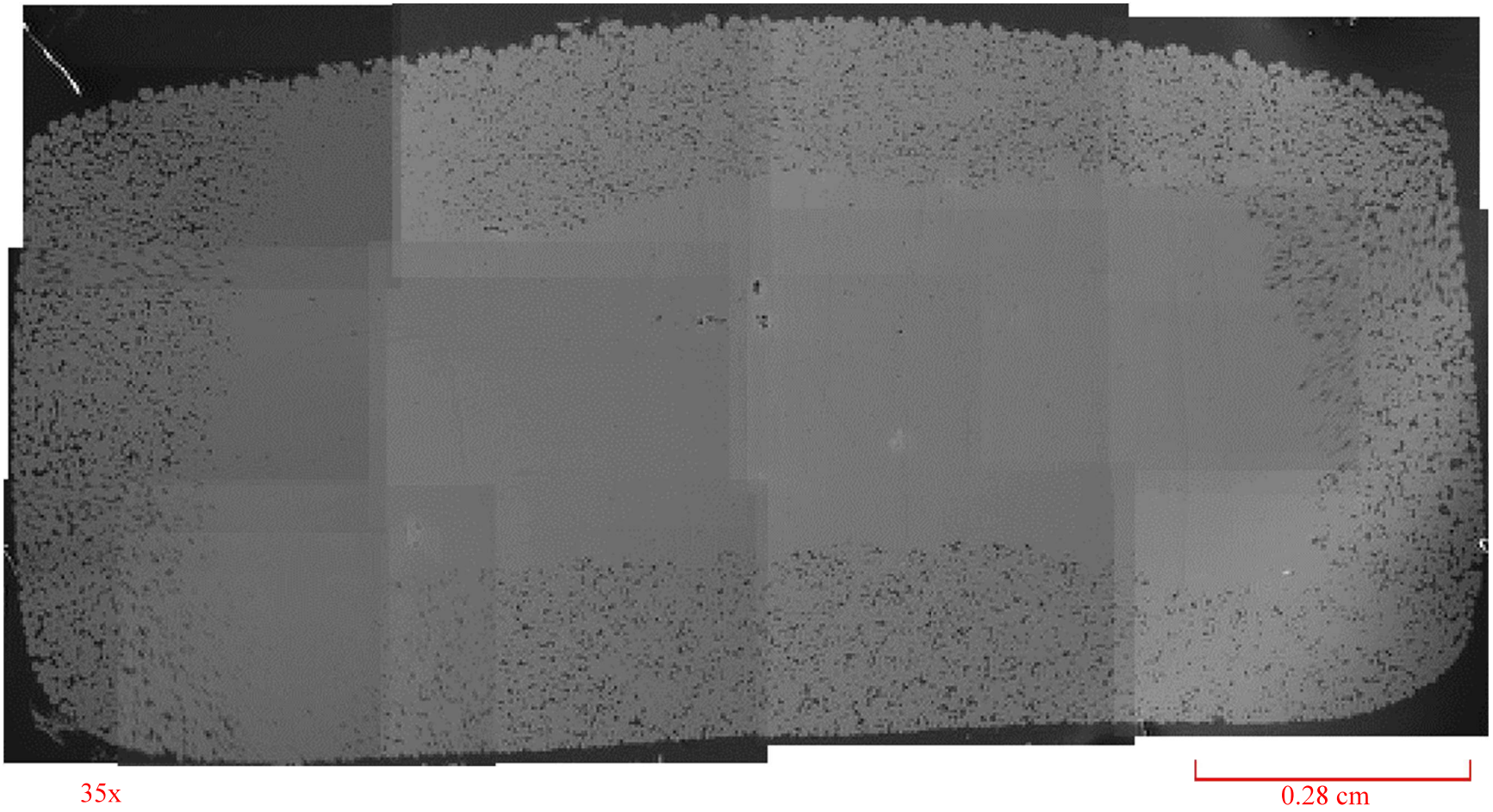

Figure 49: Pellet 4.1 Axial cross-section image mosaic sintered for 4 h.

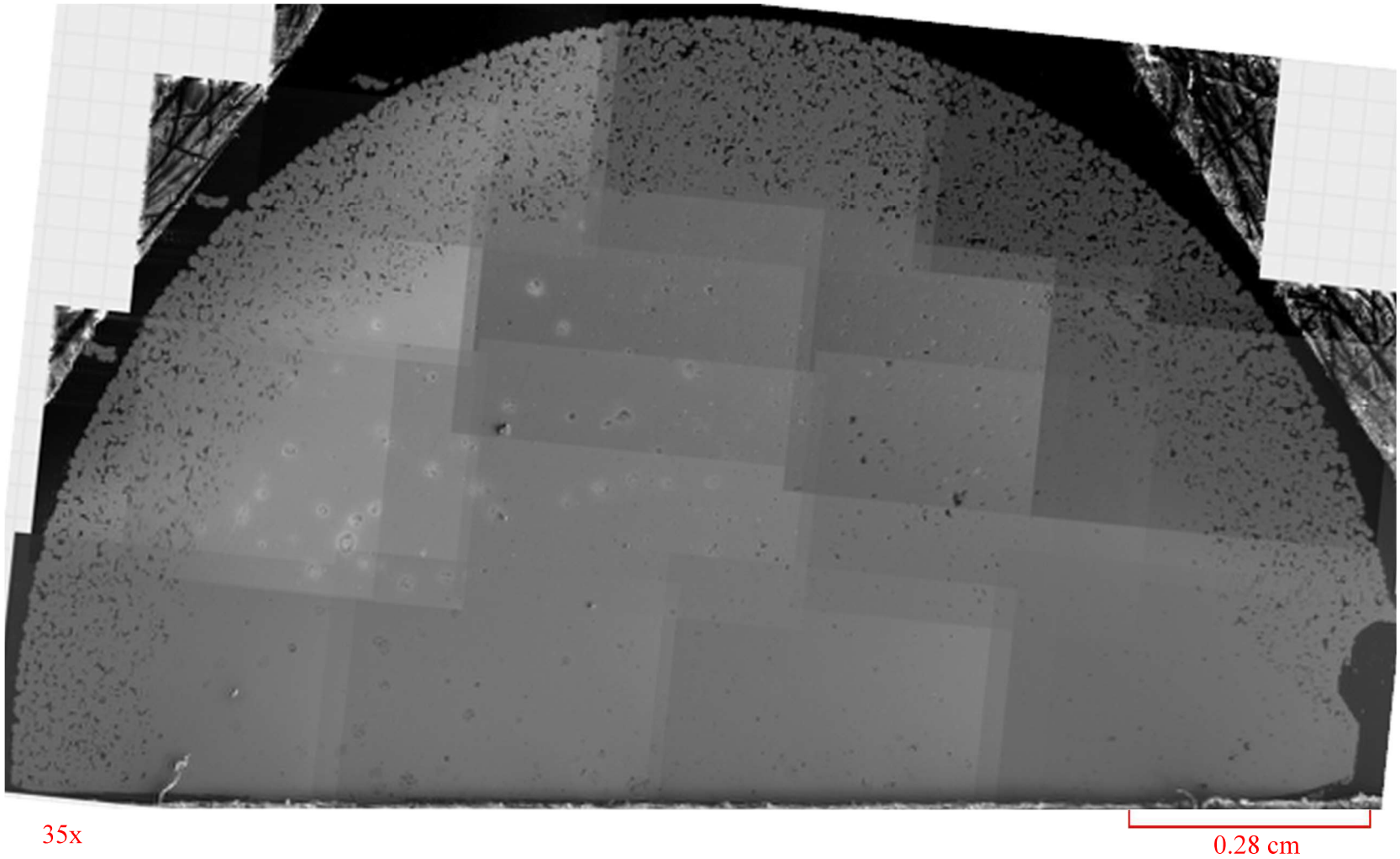

Figure 50: Pellet 4.1 Radial cross-section image mosaic sintered for 4 h.

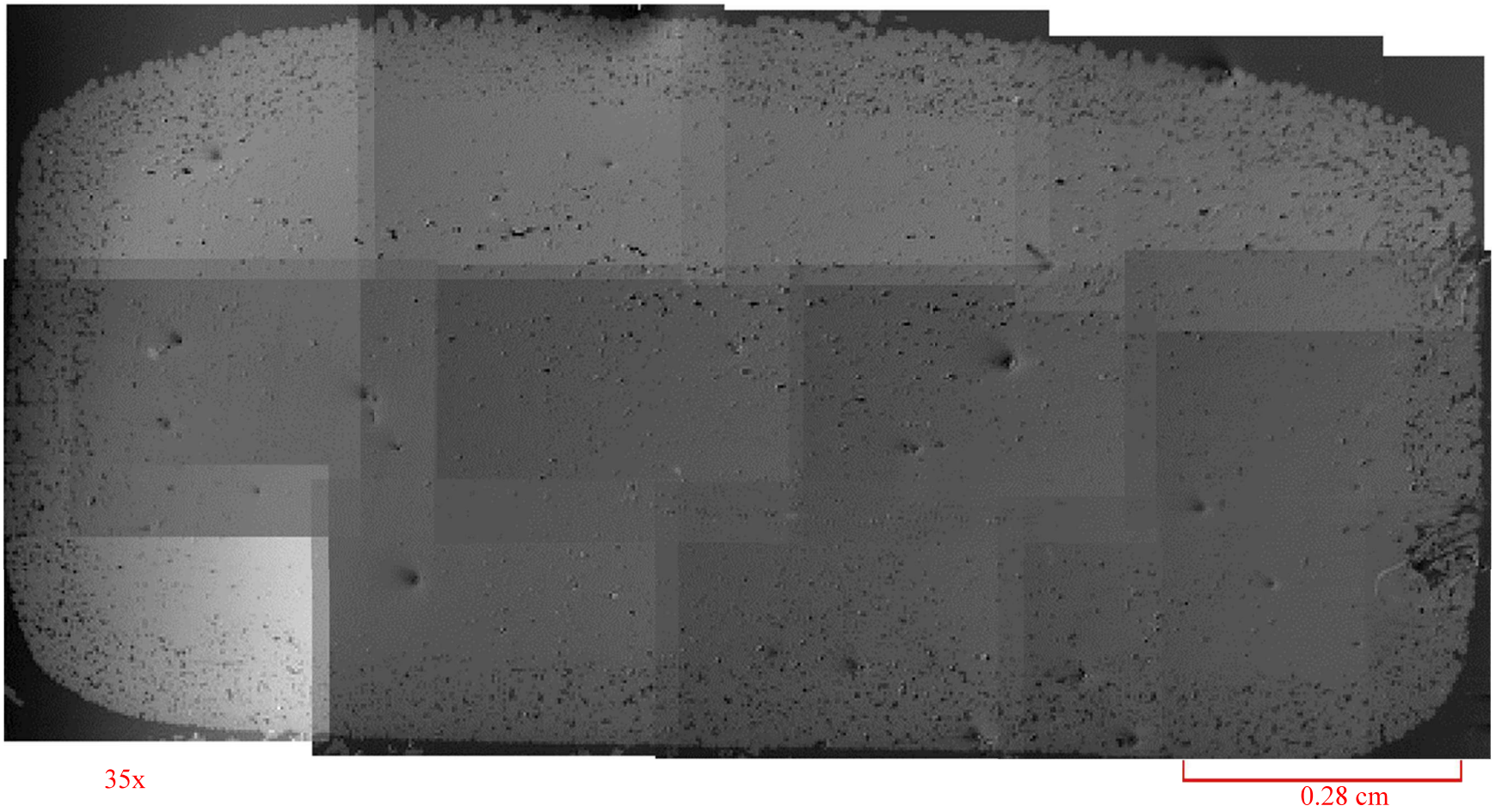

Figure 51: Pellet 4.2 Axial cross-section image mosaic sintered for 4 h.

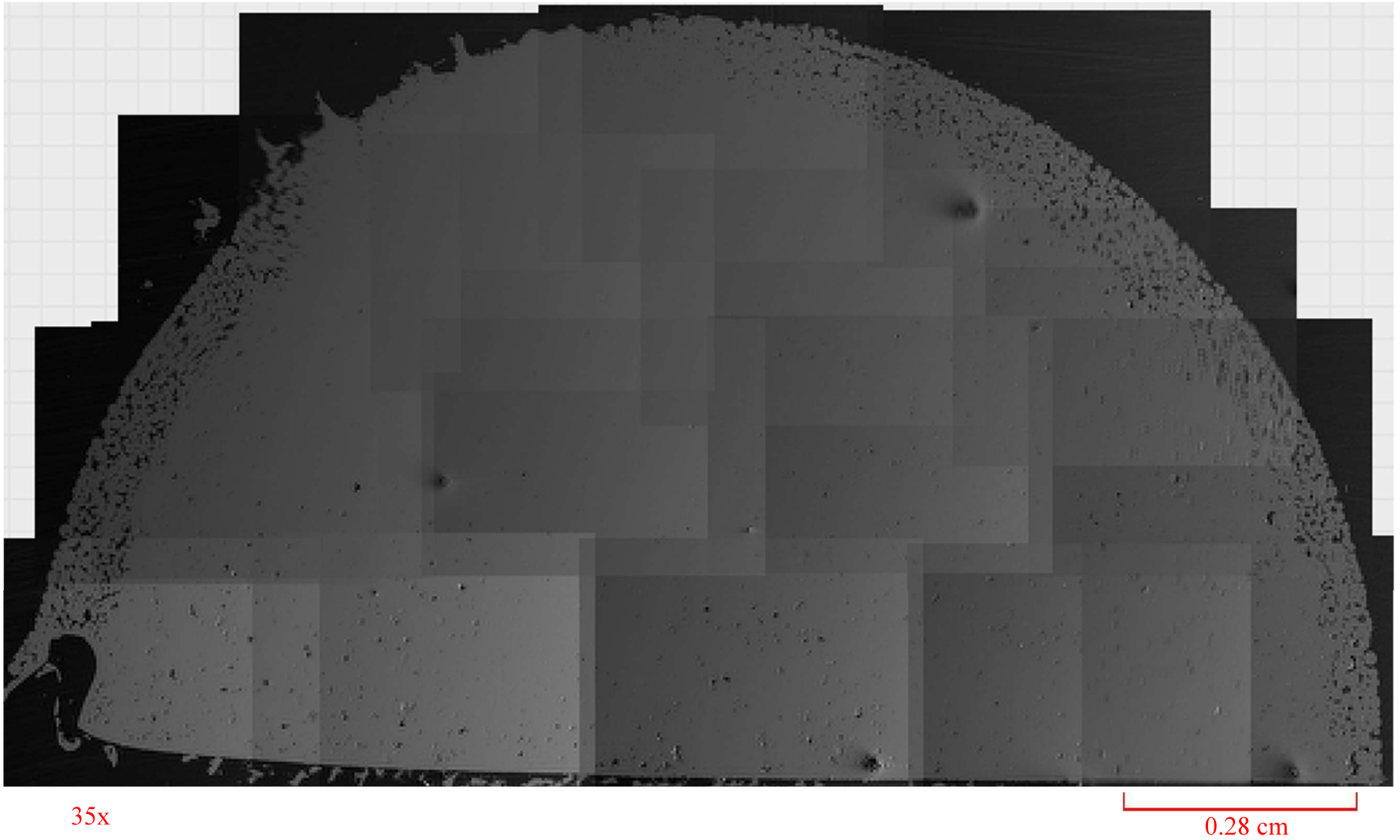

Figure 52: Pellet 4.2 Radial cross-section image mosaic sintered for 4 h.

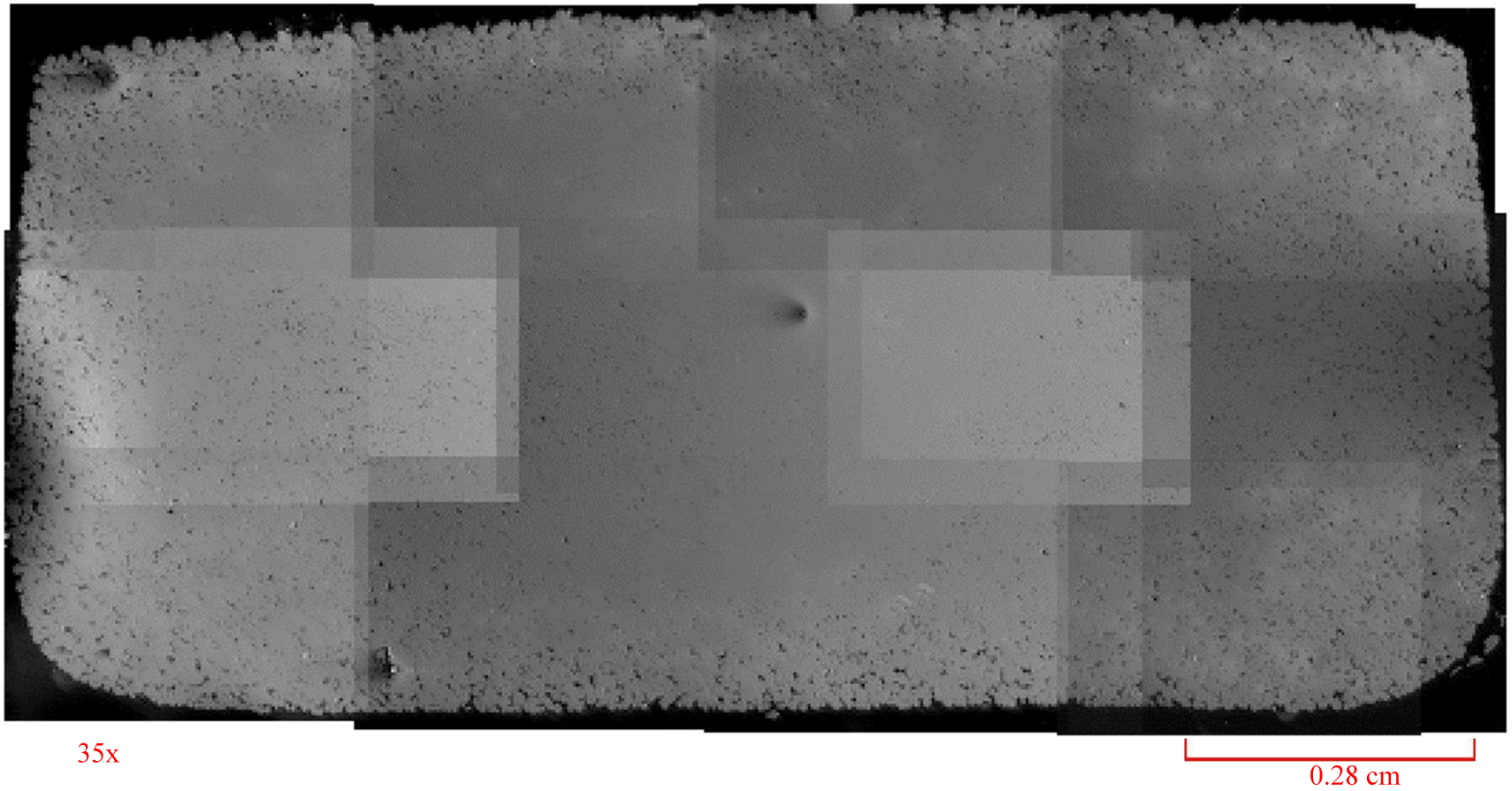

Figure 53: Pellet 6.1 Axial cross-section image mosaic sintered for 6 h.

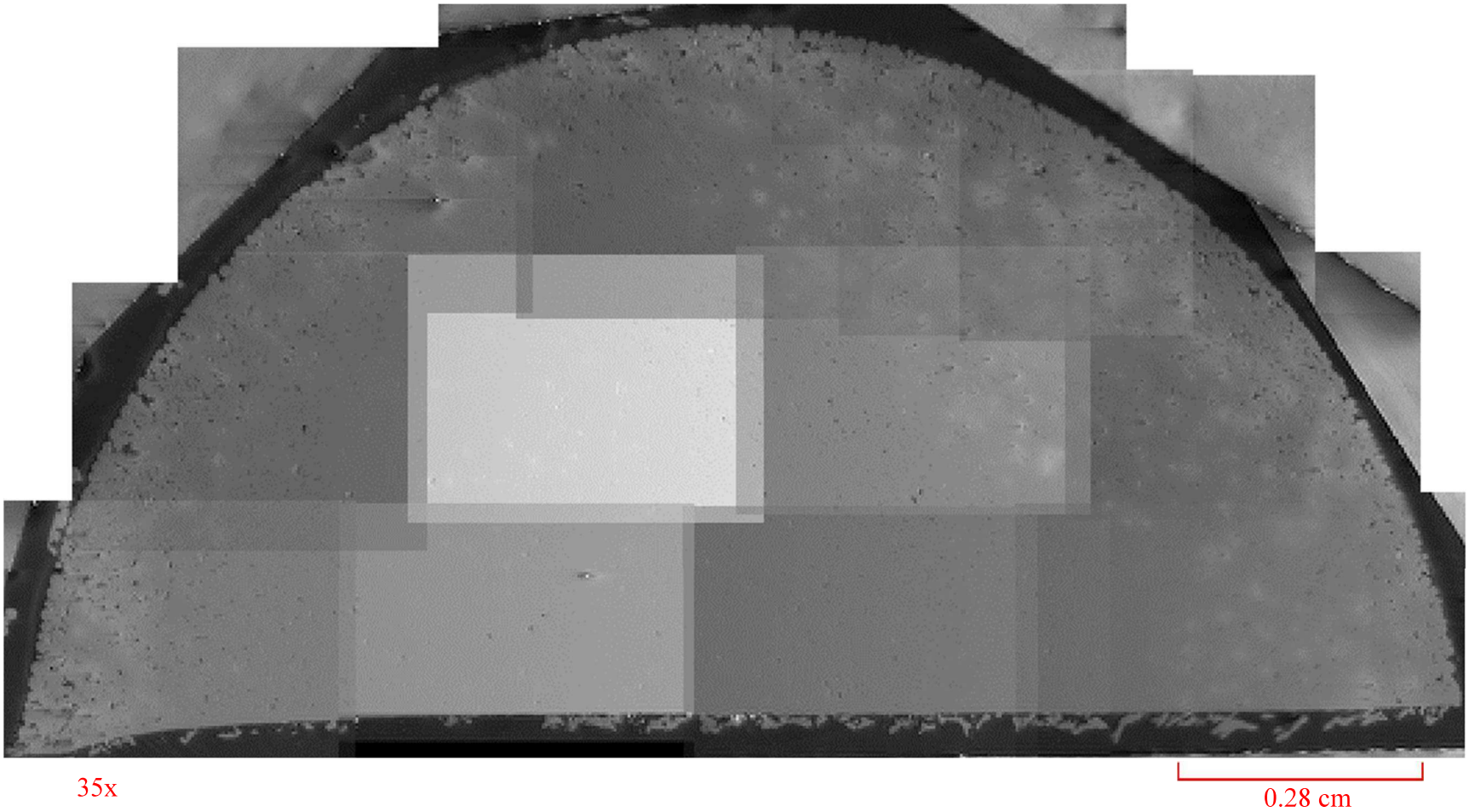

Figure 54: Pellet 6.1 Radial cross-section image mosaic sintered for 6 h.

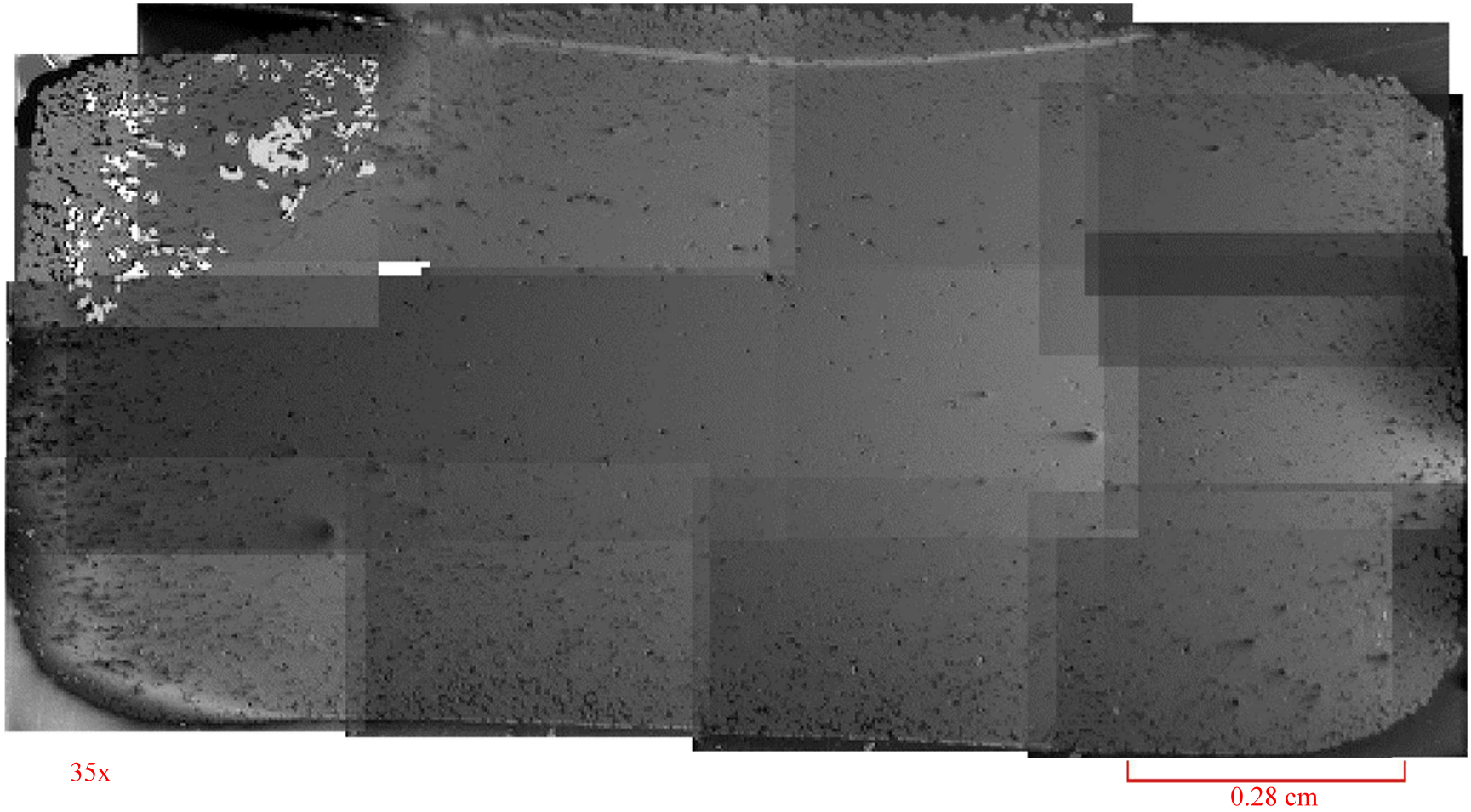

Figure 55: Pellet 6.2 Axial cross-section image mosaic sintered for 6 h.

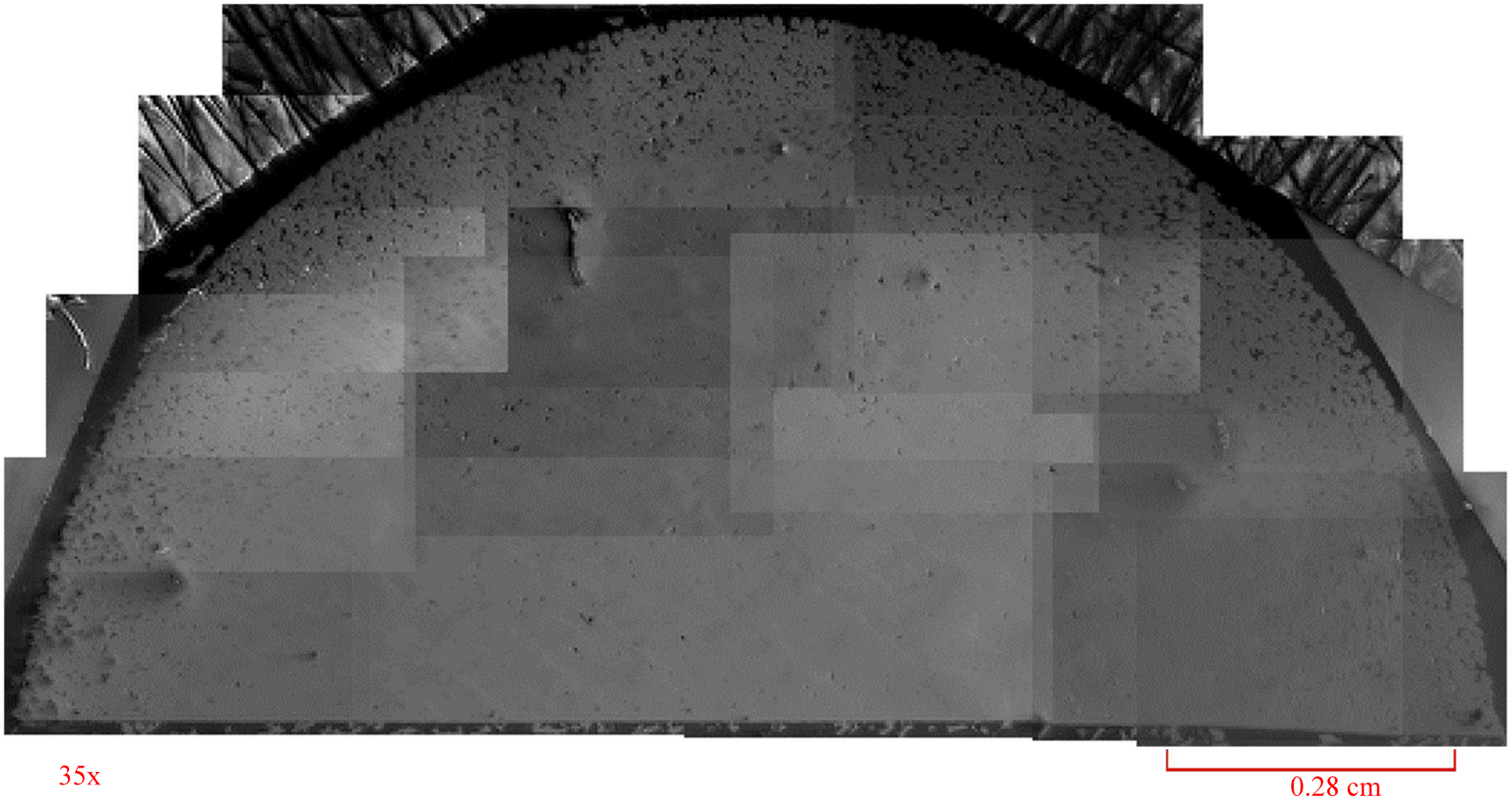

Figure 56: Pellet 6.2 Radial cross-section image mosaic sintered for 6 h.

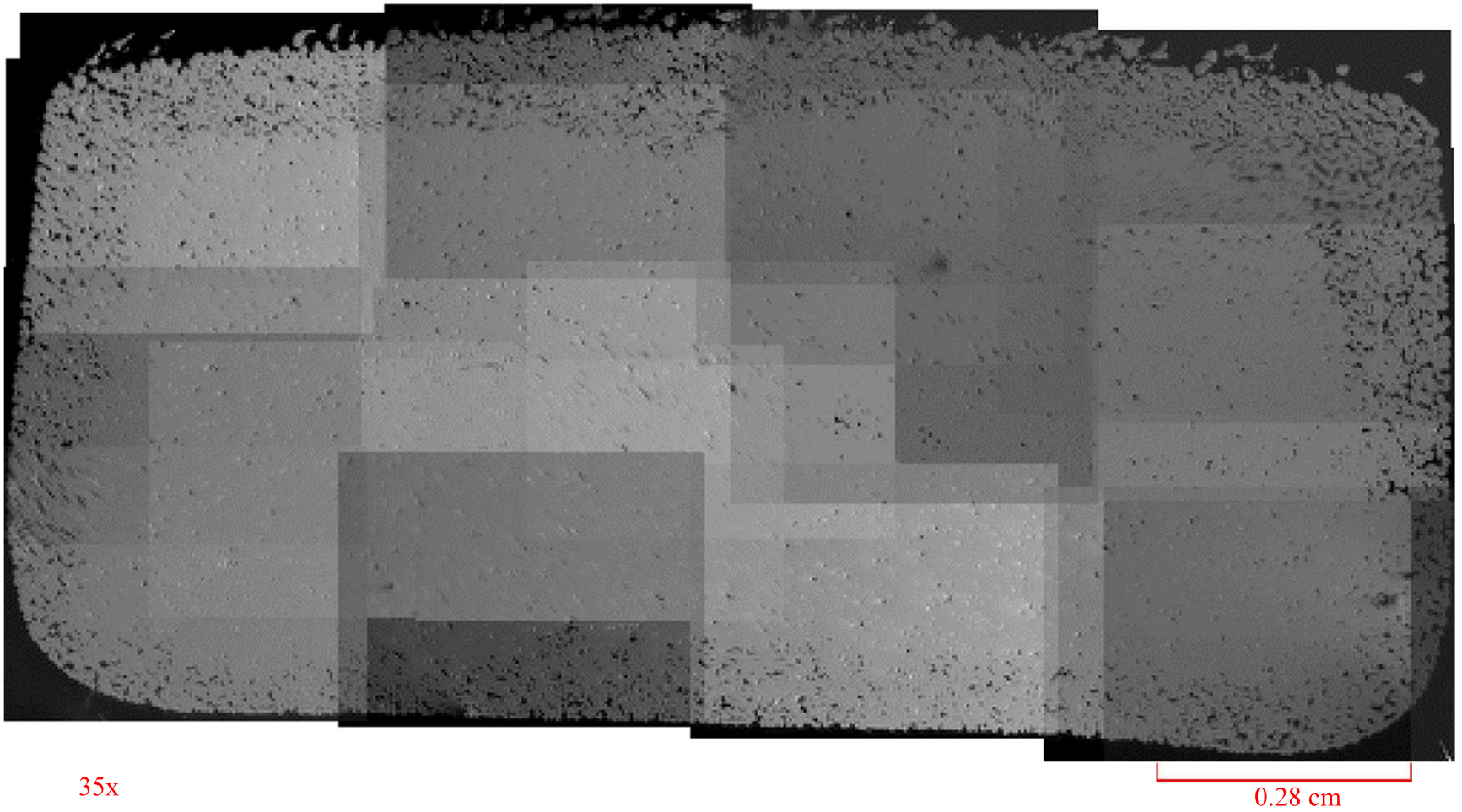

Figure 57: Pellet 12.1 Axial cross-section image mosaic sintered for 12 h.

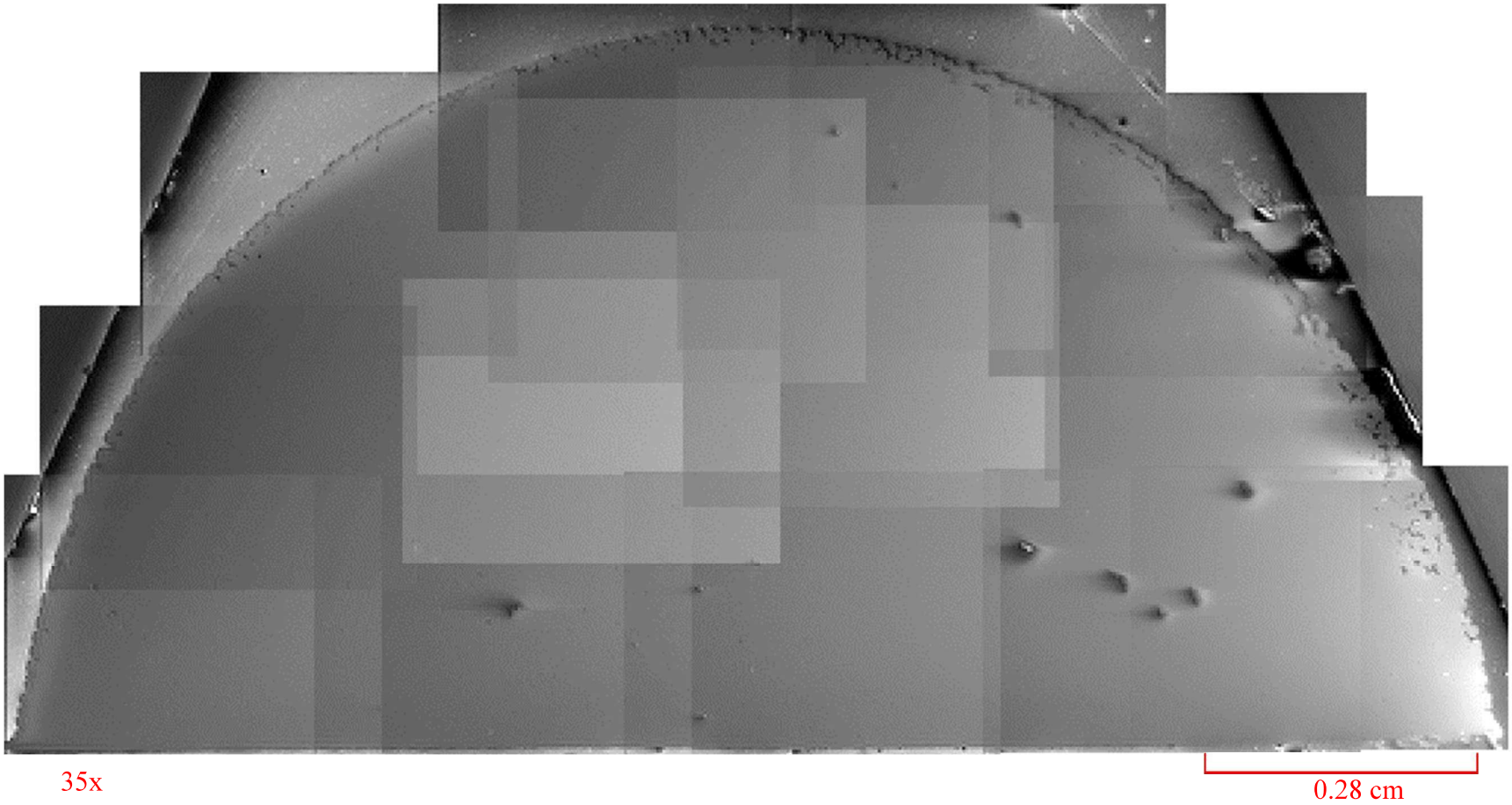

Figure 58: Pellet 12.1 Radial cross-section image mosaic sintered for 12 h.

CHAPTER 05

DATA ANALYSIS

The following tables illustrate axial and radial cross-sectional analysis, comparing dwell time and area of the cross-sections to porosity in the overall cross-section and the dense center region and porous rim within the cross-section. Tables 10 and 11 include the area porosity data of axial and radial cross-section calculated through ImageJ. The data shows results for the overall cross-section compared to the two region areas of interest DCR and PR within the OC-S, which together compose the overall porosity of the cross-section. DCR represents the dense central region, and PR represents the porous rim region of each sample. Areal and porosity calculations and porosity values were derived for each area of interest within the OC-S, and porosity was analyzed within its region boundaries and compared to the OC-S.

Table 10: Area and porosity calculations for axial cross-sections, derived from imageJ, including dense central region and porous rim porosity comparative values.

Pellet ID	OVERALL CROSS-SECTION (OC-S)			DENSE CENTER REGION (DCR)					POROUS RIM (PR)				
	Area (cm^2)	Porosity (cm^2)	Porosity (%)	Area (cm^2)	Area Percent of OC-S (%)	Porosity (cm^2)	Porosity Percent of OC-S Area (%)	Boundary Region Porosity (%)	Area (cm^2)	Area Percent of OC-S (%)	Porosity (cm^2)	Porosity Percent of OC-S Area (%)	Boundary Region Porosity (%)
1.1	0.62	0.07	11.34	0.26	42.24	0.01	1.73	4.09	0.36	57.76	0.06	9.61	1.73
1.2	0.62	0.05	7.67	0.31	49.40	0.01	1.52	3.08	0.31	50.60	0.04	6.15	1.52
2.1	0.59	0.02	3.73	0.42	71.97	0.01	0.89	1.23	0.16	28.03	0.02	2.84	0.89
2.2	0.58	0.05	8.20	0.37	63.93	0.01	1.73	2.70	0.21	36.07	0.04	6.47	1.73
3.1	0.57	0.04	6.59	0.42	73.61	0.00	0.87	1.18	0.15	26.39	0.03	5.72	0.87
3.2	0.58	0.05	9.26	0.23	39.34	0.01	0.94	2.38	0.35	60.66	0.05	8.33	0.94
4.1	0.54	0.04	6.61	0.22	41.12	0.00	0.08	0.20	0.32	58.88	0.04	6.53	0.08
4.2	0.59	0.03	4.95	0.39	66.72	0.01	1.49	2.23	0.20	33.28	0.02	3.46	1.49
6.1	0.59	0.02	3.09	0.30	49.93	0.00	0.61	1.23	0.30	50.07	0.01	2.48	0.61
6.2	0.59	0.04	6.08	0.40	67.90	0.01	1.28	1.89	0.19	32.10	0.03	4.80	1.28
12.1	0.54	0.03	4.98	0.37	67.86	0.00	0.74	1.09	0.17	32.14	0.02	4.24	0.74
12.2	NA	NA	NA	NA	NA	NA	NA	NA	NA	NA	NA	NA	NA

Table 11: Area and porosity calculations for radial cross-sections, derived from imageJ, including dense central region and porous rim porosity comparative values.

Pellet ID	OVERALL CROSS-SECTION (OC-S)			DENSE CENTER REGION (DCR)					POROUS RIM (PR)				
	Area (cm^2)	Porosity (cm^2)	Porosity (%)	Area (cm^2)	Area Percent of OC-S (%)	Porosity (cm^2)	Porosity Percent of OC-S (%)	Boundary Porosity (%)	Area (cm^2)	Area Percent of OC-S (%)	Porosity (cm^2)	Porosity Percent of OC-S (%)	Boundary Porosity (%)
1.1	0.52	0.03	6.08	0.23	43.07	0.01	2.10	4.88	0.30	56.93	0.02	3.97	6.98
1.2	0.49	0.03	5.80	0.34	69.10	0.00	0.85	1.22	0.15	30.90	0.02	4.95	16.03
2.1	0.51	0.02	2.93	0.48	94.27	0.00	0.65	0.69	0.03	5.73	0.01	2.28	39.90
2.2	0.69	0.02	3.45	0.43	62.86	0.01	0.95	1.50	0.26	37.14	0.02	2.50	6.74
3.1	0.56	0.01	2.39	0.45	80.70	0.00	0.40	0.49	0.11	19.30	0.01	1.99	10.31
3.2	0.97	0.03	3.09	0.21	22.18	0.00	0.08	0.36	0.75	77.82	0.03	3.01	3.87
4.1	0.61	0.02	3.85	0.36	58.92	0.00	0.32	0.54	0.25	41.08	0.02	3.53	8.60
4.2	0.60	0.01	2.35	0.52	86.32	0.00	0.49	0.57	0.08	13.68	0.01	1.86	13.56
6.1	0.46	0.01	2.40	0.40	85.28	0.01	2.37	2.78	0.07	14.72	0.00	0.04	0.24
6.2	0.46	0.02	4.21	0.32	70.11	0.00	0.75	1.08	0.14	29.89	0.02	3.45	11.56
12.1	0.44	0.00	0.89	0.43	96.04	0.00	0.04	0.04	0.02	3.96	0.00	0.85	21.43
12.2	NA	NA	NA	NA	NA	NA	NA	NA	NA	NA	NA	NA	NA

This chapter reviews the porosity results calculated through ImageJ for each cross-section from sintered pellets across the dwell time profile. Section 5.1 covers the evolution of copper morphology of the overall axial and radial cross-sections for pellets sintered at 1065°C. Detailed tables were provided to show area and porosity results for each pair of axial and radial cross-sections sintered at the varying dwell times between 1 h to 12 h, with the exception that only one axial and one radial cross-section was analyzed at the dwell time of 12 h due to equipment malfunction. This data was then summarized to later provide porosity percentage values for the average of each pair of cross-sections at their respective dwell times, relative to the overall aerial boundaries set for each cross-section. The trends observed in these data points resulted in a decreasing trend of porosity loss with increasing dwell time, and an overall loss of porosity of ~5% in both cross-sections. Porosity was further analyzed to show the behavior of a porosity gradient with higher observable porosity seen along a porous ring (PR) present at the edges of both axial and radial cross-sections at all dwell times in section 5.2 and seen above in tables 10 and 11. This porous region was analyzed in comparison to a dense central region along all cross-sections where porosity appeared minimal. Porosity gradient trends highlighted the observed direct correlation between the porous ring (PR) and the overall porosity of the axial cross-sections, while this was not the case for radial cross-sections. Section 5.3 summarizes the porosity behavior in pellet cross-sections. Section 5.4 concludes the overall goals of this study, along with methods to improve results for future reference.

5.1 Evolution of Copper Morphology at 1065°C

Density calculations from sintered unpacked powder pellets as mentioned in chapter 04 showed a relative increase in density with increasing sintering dwell time. However, porosity was further analyzed along the volume of structures with the analysis of pellet cross-sectional

SEM images and respective area fraction. SEM images along the central axial and radial cross-sections offered an overview of the evolution of porosity in the pellets with increasing dwell time. The area (cm^2) and porosity (cm^2) of the overall cross-section was a composite average sum of the area of each individual image analyzed, while porosity was compared to this value to calculate a porosity percentage per cross-section. Table 12 and 13 show the average area and porosity relative to overall cross-sectional area values analyzed from each average pair of pellet cross-sections per sintering dwell time.

In Table 12 area, porosity axial cross-sections of pellets are shown, while Table 13 shows the same data for radial cross-sections.

Table 12: Average axial cross-sectional area and porosity values per sintering dwell time.

Dwell Time (h)	Images analyzed	Area (cm^2)	Porosity (cm^2)	Porosity (%)
1	33	0.62	0.06	9.50
2	31	0.59	0.03	5.96
3	31	0.57	0.05	7.94
4	28	0.56	0.03	5.75
6	32	0.59	0.03	4.80
12*	20	0.54	0.03	4.99

Table 13: Average radial cross-sectional are and porosity values per sintering dwell time.

Dwell Time (h)	Images analyzed	Area (cm^2)	Porosity (cm^2)	Porosity (%)
1	33	0.51	0.03	5.94
2	32	0.60	0.02	3.23
3	35	0.76	0.02	2.83
4	34	0.92	0.02	2.03
6	31	0.46	0.02	3.30
12*	15	0.44	0.00	0.85

Area calculated for axial cross-sections show a decreasing trend as the sintering dwell time increases. This was likely due to the densification of Cu spheres in the pellet as the dwell

time increased. The area of radial cross-sections did not show a relative decreasing trend; however, this was expected due to these cross-sections being obtained after the pellet sample was already sliced once to produce the axial cross-section. The porosity results from these two cross-sectional planes were not enough to derive the overall porosity of the pellet volume. This would be an accurate derivation if more cross-sections were obtained from each pellet sample and analyzed with ImageJ. Current laboratory equipment limited the opportunity to do so, and the data from each axial and radial cross-section of pellets was separated and tabulated to understand the pellet densification with increasing sintering dwell time.

It should be noted that variance calculations were conducted for each cross-section by estimating the porosity threshold three times of at least one image per row of the composite cross-sectional image mesh. The three calculations included a standard calculation which showed the optimal observable porosity in regard to threshold, as well as a value for threshold slightly below and above this standard, which still resulted in an approximate of porosity in the image. These calculations were averaged for each cross-section and again for each dwell time. Variance values were averaged over every pair of pellets sintered for the same dwell time, and an overall average was calculated from the percentage of porosity above as well as bellow the standard porosity percentage values. Results are shown in table 14 and table 15 for the average axial and radial porosity variances, including the number of images analyzed to derive to these results. For axial cross-sections, porosity values above the standard value averaged a variance in porosity percent of less than ~0.59%, The average percentage of porosity below the standard value for all axial cross-sections resulted in an average variance of ~0.48%. The values were similar for radial cross-sections with the average percent of porosity above and below the standard value being ~ 0.53% and ~0.50% respectfully.

Table 14: Average variances calculated for axial cross-sectional images, based on calculations exceeding and underestimating the standard observable threshold value.

Dwell Time (h)	Number of Images Analyzed	Percentage of Porosity Above Standard Value (%)	Percentage of Porosity Below Standard Value (%)
1	13	0.34	0.67
2	14	0.92	0.27
3	13	0.69	0.63
4	10	0.64	0.59
6	9	0.62	0.40
12*	4	0.31	0.29
		AVG% ~ 0.59	AVG% ~0.48

Table 15: Average variances calculated for radial cross-sectional images, based on calculations exceeding and underestimating the standard observable threshold value.

Dwell Time (h)	Number of Images Analyzed	Percentage of Porosity Above Standard Porosity Value (%)	Percentage of Porosity Below Standard Porosity Value (%)
1	12	1.05	0.93
2	16	0.62	0.80
3	8	0.41	0.25
4	8	0.51	0.50
6	12	0.56	0.46
12*	4	0.05	0.05
		AVG% ~0.53	AVG% ~0.50

These average variance values were acceptable since they did not exceed standard observable porosity by over 1% or more and indicated that porosity was measured with a level of accuracy. These values are represented as the variance bars in the following figure 59, illustrating the porosity percent of the average dwell times in regard to the cross-section and dwell time.

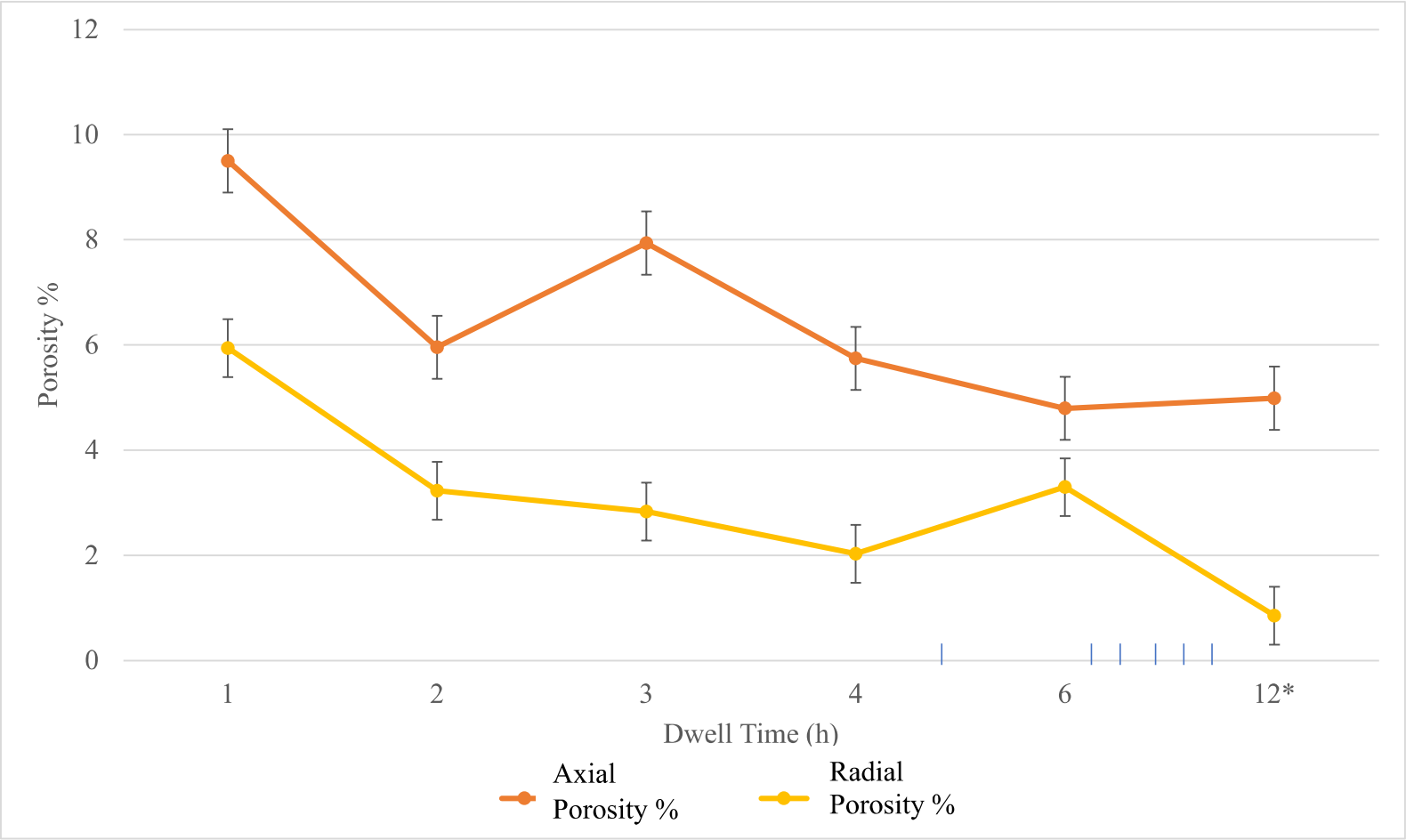

Figure 59: Porosity percentage of axial and radial cross-sections relative to dwell time.

Axial cross-section average porosity trends in figure 58 showed an initial porosity of ~10% at 1h of dwell time. Porosity percentage decreased most between 1 h to 2 h of dwell time, with a loss of ~4% in porosity. This declining trend was expected to continue through all the dwell times, but area fraction analysis results showed a rise in porosity at a dwell time of 3 h with a porosity percentage of ~8%. The decreasing porosity trend was more consistent between dwell times of 3 h (~ 8%) to 6 h (~5%), with an overall porosity percentage loss of ~3%. The singular pellet analyzed for porosity at a dwell time of 12 h resulted in a porosity percentage of ~5%, very close to the result of 6 h. Axial cross-sectional porosity trends resulted in a porosity percentage loss of ~5% from a sintering dwell time of 1 h to 12 h.

Radial cross-section porosity trends in figure 58 had a starting point of ~6% porosity at 1 h of dwell time, followed by a loss of ~3% at 2 h, the highest loss in porosity through the trend. A steady decrease in porosity was observed in the trend until a dwell time of 6 h, where porosity increased to just over 3%, and decreased to under 1% at a dwell time of 12 h. From the starting dwell time of 1 h (with a porosity percentage of ~6%) to 12 h (porosity percentage of ~1%), there was a total loss of 5% in porosity.

Both axial and radial cross sections showed an approximation of 5% porosity loss when comparing initial dwell time to final dwell time. The axial cross-section porosity trend had higher porosity data points than radial cross-sections, and both trends included a data point which showed an unexpected increase in porosity. This point happed at 3 h for axial cross-sections and 6 h for radial cross-sections. It should be noted that radial porosity percentages were relative to the approximate half of the total sample, due to the process of sample cutting, whereas the axial cross-section is whole. Both cross-sectional trends showed a decreasing porosity percentage trend overall.

Overall volumetric porosity and density behavior was be assumed to have be accurately represented in terms of porosity behavior through imageJ area fraction results considering that only two planes of each sample were analyzed. However, these results do provide a basic understanding for the density and porosity evolution of unpacked sintered copper pellets for temperatures close to copper's melting point. Accurate approximation of volumetric porosity could be increased through the area fraction porosity analysis of more than two cross-sections of a single pellet sample along other planes of the pellet beyond the central height and central width planes.

Porosity behavior in the previously mentioned pellet cross-sections was further analyzed to study the observed density migration and porosity gradient in the area fraction of all sintered samples.

5.2 Porosity Gradient: Inner Porosity, Outer Porosity

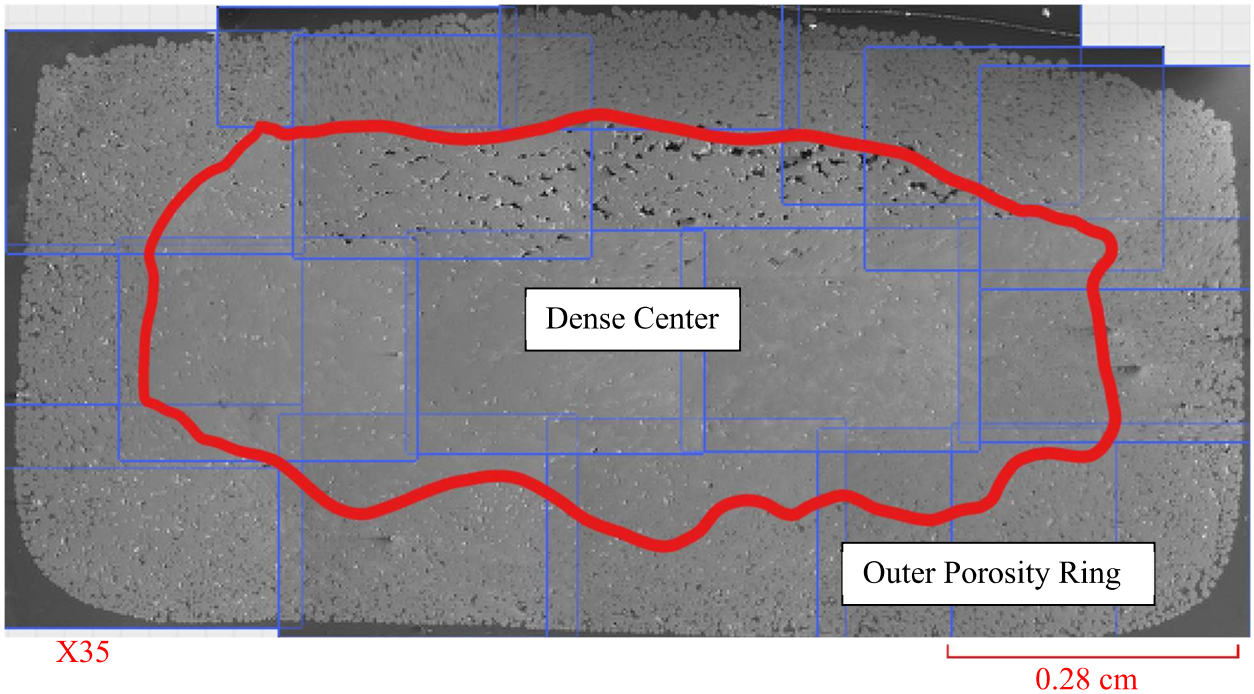

Figure 60: 1 h dwell axial mosaic stitched cross-section including the boundaries of each image (outlined in blue, and the boundary of the porosity gradient outlined in red.

All pellet cross-sections were observed to have a porous rim (PR) along the edges of pellets in both cross-sections. The porosity along this region was observed to be higher than the porosity at the center of all the pellets at all the sintered dwell times. This porosity gradient in the overall cross-section (OC-S) was studied further to establish how the PR would change in region areal size and porosity value with increasing sintering dwell time. This was done by tracing a boundary at which it was most visually observed that the porosity gradient was evident and the porous rim (PR) was separated from the dense central region (DCR). This gradient was traced with the use of straight lines connecting at several points, and enclosing the area selected within the images to encapsulate the dense central region area. The PR was the result of the subtraction of the selected DCR within the image mesh from the OC-S area boundaries. Depending on the porosity of the cross-section and the location of the image on the cross-section, some images contained area which included both the DCR and the PR, while some other images exclusively contained area on one or the other section of the porosity gradient in the cross-section.

With increasing sintering dwell times, the cross-sections were observed to develop a higher density at the DCR. The boundaries of the DCR and PR were observed to increase in size through the progression of dwell time from 1 h to 12 h in both axial and radial cross-sections. Porosity analyzed in these regions of the average axial and radial OC-S did show a decreasing trend with increasing dwell time when compared to the OC-S area measurement as well as within both regional boundaries (DCR and PR). The data from these observations is shown in tables 16 and 17.

Table 16: Average axial cross-sectional porosity measurements for the overall cross-section, dense center region, and porous ring.

	OVERALL CROSS-SECTION (OC-S)			DENSE CENTER REGION (DCR)					POROUS RIM (PR)				
Dwell Time (h)	Area (cm^2)	Porosity (cm^2)	Porosity %	Area (cm^2)	Area Percent of OC-S %	Porosity (cm^2)	Porosity Percent of OC-S Poprosity %	Boundary Porosity %	Area (cm^2)	Area Percent of OC-S %	Porosity (cm^2)	Porosity Percent of OC-S Porosity %	Boundary Porosity %
1	0.51	0.03	5.94	0.28	45.82	0.01	1.62	3.54	0.34	54.18	0.05	7.88	14.54
2	0.60	0.02	3.23	0.40	67.96	0.01	1.31	1.92	0.19	32.04	0.03	4.65	14.52
3	0.76	0.02	2.83	0.32	56.34	0.01	0.90	1.61	0.25	43.66	0.04	7.03	16.11
4	0.92	0.02	2.03	0.31	54.46	0.00	0.81	1.50	0.26	45.54	0.03	4.93	10.83
6	0.46	0.02	3.30	0.35	58.91	0.01	0.95	1.61	0.24	41.09	0.02	3.64	8.86
12*	0.44	0.00	0.89	0.37	67.86	0.00	0.74	1.09	0.17	32.14	0.02	4.24	13.18

.

Table 17: Average radial cross-sectional porosity measurements for the overall cross-section, dense center region, and porous ring.

	OVERALL CROSS-SECTION (OC-S)			DENSE CENTER REGION (DCR)					POROUS RIM (PR)				
Dwell Time (h)	Area (cm^2)	Porosity (cm^2)	Porosity %	Area (cm^2)	Area Percent of OC-S (%)	Porosity (cm^2)	Porosity Percent of OC-S (%)	Porosity Within Boundary (%)	Area (cm^2)	Area Percent of OC-S (%)	Porosity (cm^2)	Porosity Percent of OC-S (%)	Porosity Within Boundary (%)
1	0.51	0.03	5.94	0.28	55.73	0.01	1.49	2.68	0.23	44.27	0.02	4.45	10.05
2	0.60	0.02	3.23	0.47	77.83	0.00	0.82	1.05	0.13	22.17	0.01	2.41	10.87
3	0.76	0.02	2.83	0.33	43.65	0.00	0.20	0.45	0.43	56.35	0.02	2.70	4.68
4	0.92	0.02	2.03	0.44	47.50	0.00	0.27	0.56	0.49	52.50	0.02	1.76	9.83
6	0.46	0.02	3.30	0.36	77.77	0.01	1.57	2.02	0.10	22.23	0.01	1.73	7.77
12*	0.44	0.00	0.89	0.43	96.04	0.00	0.04	0.04	0.02	3.96	0.00	0.85	21.43

The porosity results though the analysis of DCR and PR boundaries in average axial and radial cross-sections concluded that these regions increased in size relative to OC-S area and overall sintering temperature increase, with the exception of dwell times of 2 h in the axial cross-sections and 3h – 4 h of the radial cross-sections. Porosity in average axial cross-sections DCR relative to the OC-S general porosity decreased steadily with increasing dwell time, with values of 3 h, 4 h and 6 h dwell times maintaining similar results. Porosity in the PR boundary consisted of most of the porosity calculated for the axial OC-S. The average radial cross-section porosity values resulted in more complex behavior compared to the previously mentioned axial cross-sections. The PR boundary region was also observed to contain most of the OC-S for radial cross-sections, with the exception of the cross-sections dwelled for 6 h. These calculations suggested that the average porosity of the DCR was correlated to the overall porosity of the cross-sections for this dwell time. The porosity of the DCR and PR were compared to the area of the OC-S in figure 61, for average porosity of axial cross-sections and figure 62, for average radial cross-sections. Variances in image porosity were also calculated for the images analyzed in the two regions of interest within the OC-S area.

Tables 18 and 19 include the porosity percentage variances for images calculated in the DCR of the axial and radial cross-sections, respectfully. These calculations indicated that variances above and below the standard porosity percentage values decreased compared to OC-S results. This was likely due to the DCR not including complex porosity and diminishing the threshold variances from these areas. Porosity percentage values above and below the average standard values for both cross-sections averaged value

between 0.30% and 0.36%, respectfully, concluding an approximate porosity variance within ± 0.40% for the porosity calculated for average axial cross-sections. Similarly, average radial cross-sections resulted in an average of ~0.17% porosity above the standard porosity value, and ~0.15% bellow the standard porosity value.

Table 18: Axial porosity percentage values above and below the standard value calculated through imageJ.

Dwell Time (h)	Number of Images Analyzed	Percentage of porosity above standard value %	Percentage of porosity above standard value %
1	13	0.35	0.57
2	14	0.29	0.19
3	13	0.38	0.36
4	10	0.11	0.10
6	9	0.31	0.25
12*	4	0.34	0.10
		AVG % ~0.30	AVG% ~0.36

Table 19: Radial porosity percentage values above and below the standard value of calculated through imageJ.

Dwell Time (h)	Number of Images Analyzed	Percentage of porosity above standard value %	Percentage of porosity above standard value %
1	13	0.25	0.16
2	14	0.25	0.29
3	13	0.07	0.05
4	10	0.14	0.13
6	9	0.30	0.24
12*	4	0.02	0.01
		AVG % ~0.17	AVG% ~0.15

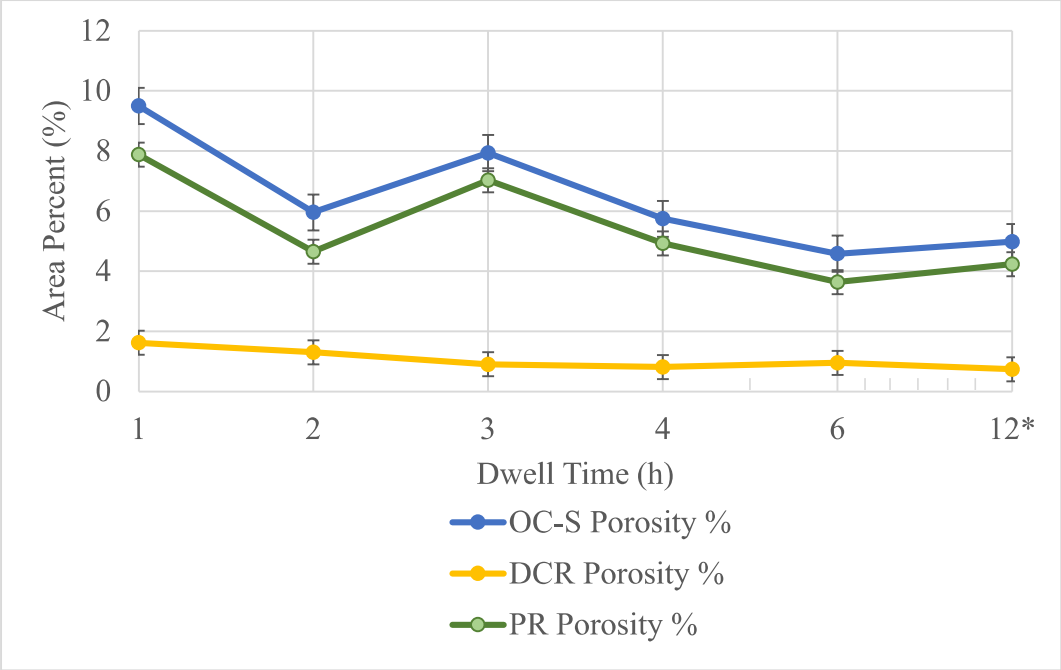

Figure 61: Axial OC-S, DCR and PR porosity percentage relative to overall area, as a function of dwell time.

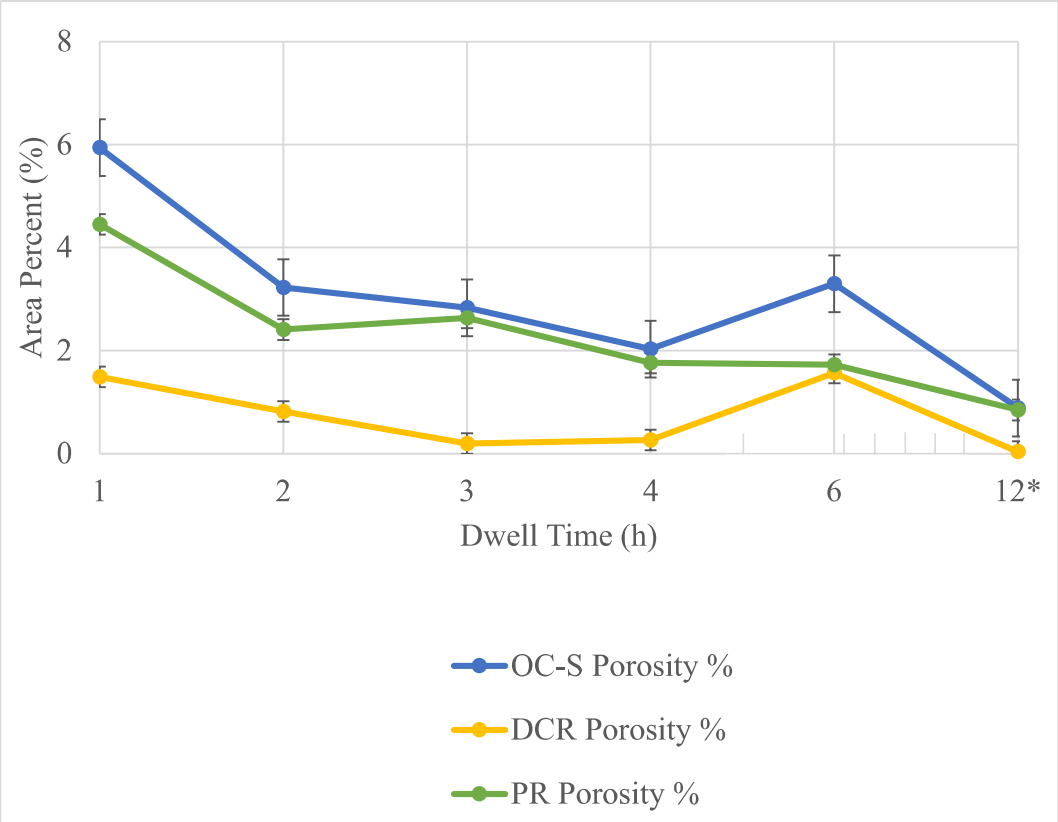

Figure 62: Radial OC-S, DCR and PR porosity percentage relative to overall area, as a function of dwell time.

Axial cross-sections and radial cross-sections include OC-S porosity values and trends as described in figure 61 and figure 62 respectfully; hence porosity trends are similar, with the difference that axial porosity gradient behavior showed the PR porosity to have the same trend as the overall cross-section porosity at all dwell times, implying that the porosity of the overall axial cross-section was mainly represented by the porosity at the edges of the cross-section. The porosity of PR trend reflected a difference of approximately -2% for every average dwell time cross-section. Porosity of the dense central region reflected a small contribution to the overall porosity in the axial cross-section ranging from ~2% porosity at 1 h of dwell time to ~1% porosity at 12* h of dwell time. The dense center of the axial cross-sections showed an overall small change in porosity with increasing dwell times, going from ~1.60% to ~0.75%.

Figure 62 porosity percentage trends for radial cross-sections varied from the axial cross-sectional trends observed due to the behavior of porosity of the PR. PR porosity percentages showed similarities to both overall cross-sectional porosity and the porosity percentage of the dense central region at varying dwell time points. From 1 h to 2 h, PR had porosity percentages of approximately -1.5% to -1% compared to the overall cross-sectional porosity. At 3 h, PR is very similar to the value of the overall porosity percentage, with a difference of less than -.20% and -.27% at 4 h. At a dwell time of 6 h, PR % resulted in a value nearly identical to DCR porosity percentage and reversing this behavior at a dwell time of 12* h

The boundary area of DCR and PR were compared to the OC-S area in axial and radial cross-sections to characterize how the size of each boundary region changed with increasing dwell time. This comparison is shown in figure 63 (axial cross-sections) and figure 64 (radial cross-sections).

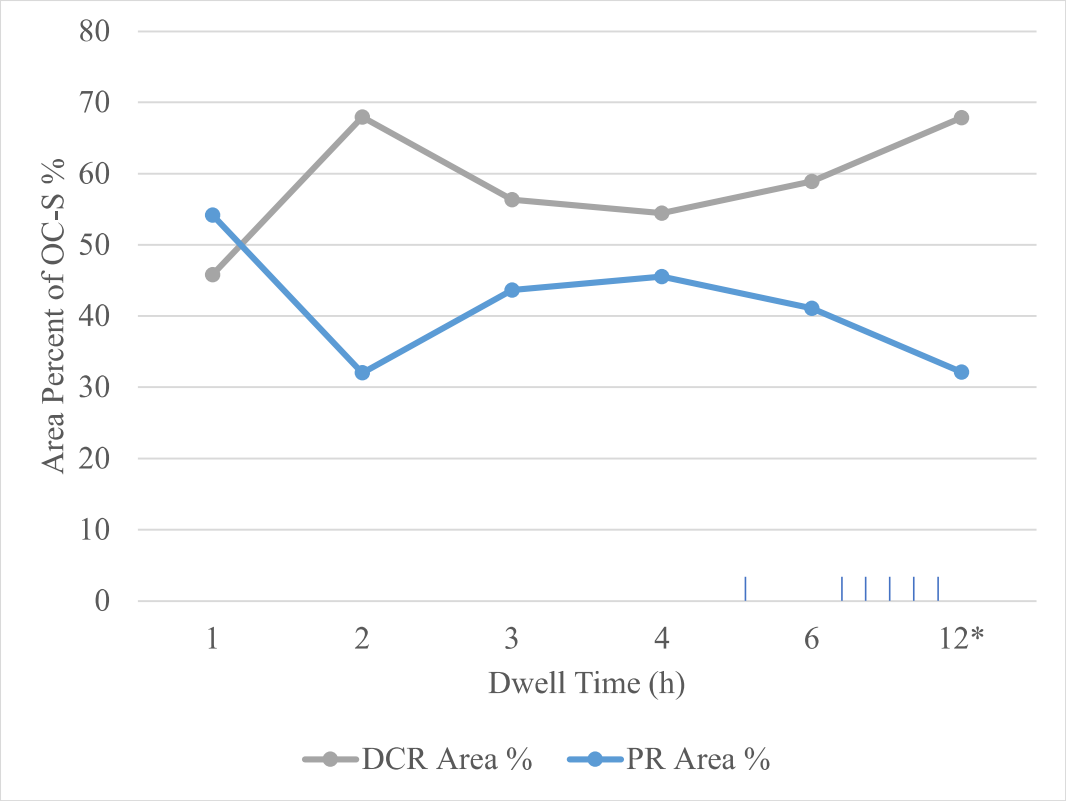

Figure 63: DCR and PR boundary area percent of axial OC-S area as a function of dwell time.

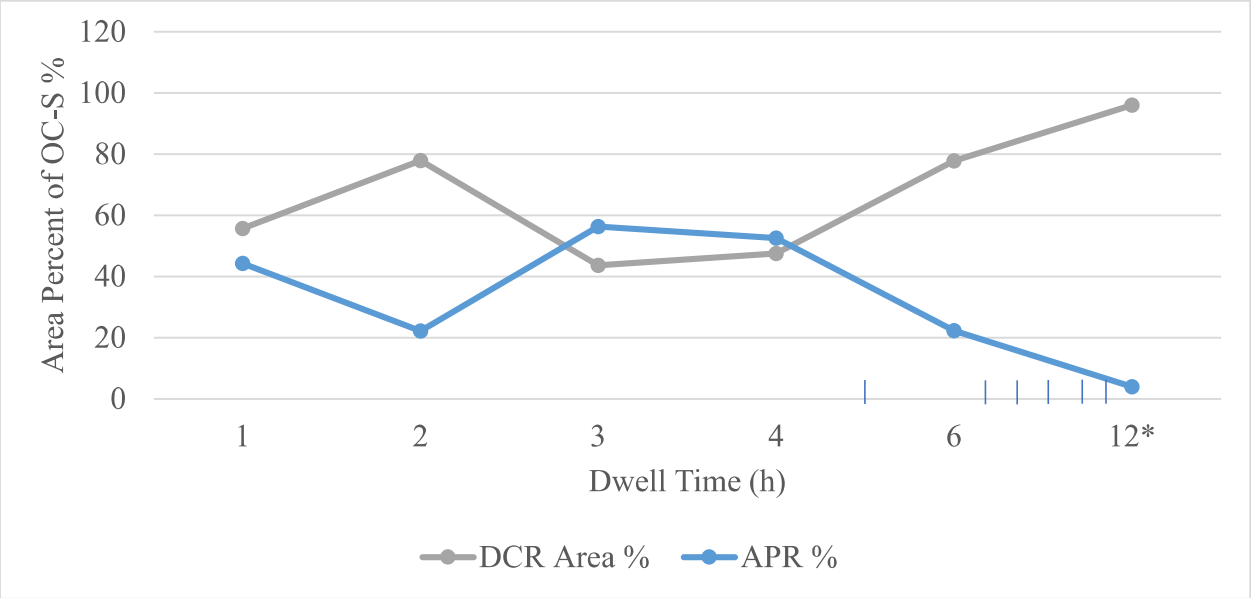

Figure 64: DCR and PR boundary area percent of radial OC-S area as a function of dwell time.

DCR and PR area percent relative to the OC-S of both axial and radial cross-sections showed that while area percentages of DCR increased with increasing dwell time, the area percent behavior for pellets dwelled for 2 h was higher than that of 3 h. At 3 h, DCR area % decreased and maintained similar values at 4 h of dwell time. After 3 h of dwell time, DCR area % in both cross-sections resembled a an approximate linear increase, with axial DCR area % at ~70% of OC-S and 12 h, and radial DCR area % at ~100% of OC-S. The area percentages of both cross-sections appeared to show that the results for dwell time of 2 h was higher than expected. This was linked to experimental environment and temperature gradients in the furnace while sintering. The PR area % for both cross-sections was a direct inverse of DCR area, showing mirror results in behavior such that as one region increases in size, the other decreases. These regions became more manageable to define while conducting image analysis for pellet cross-sections with sintering dwell times at 4 h or above.

With the DCR and PR evolution in size within the OC-S, the porosity of these two regions was also reviewed independently.

Porosity at both regions of interest within OC-S of axial and radial cross-sections, DCR and PR, was also analyzed relative to the area within the respective boundaries. This analysis displayed the evolution of porosity in the DCR and PR as a function of increasing dwell time for both cross-sections (figure 65 and figure 66).

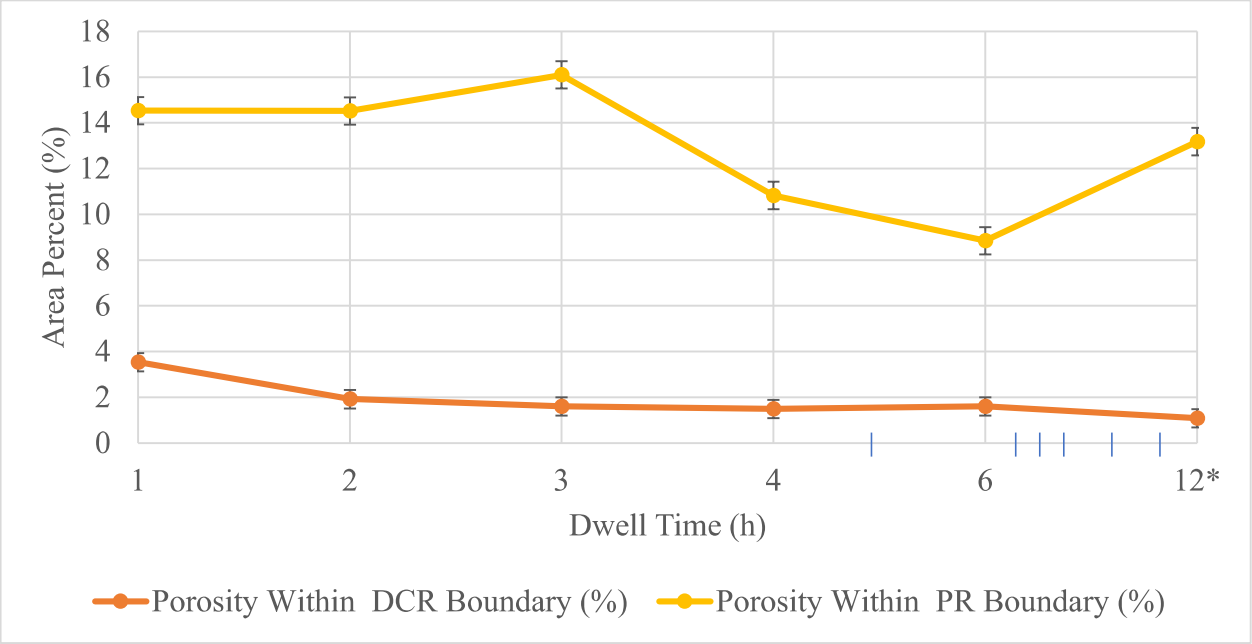

Figure 65: Axial porosity percent relative to region boundary area.

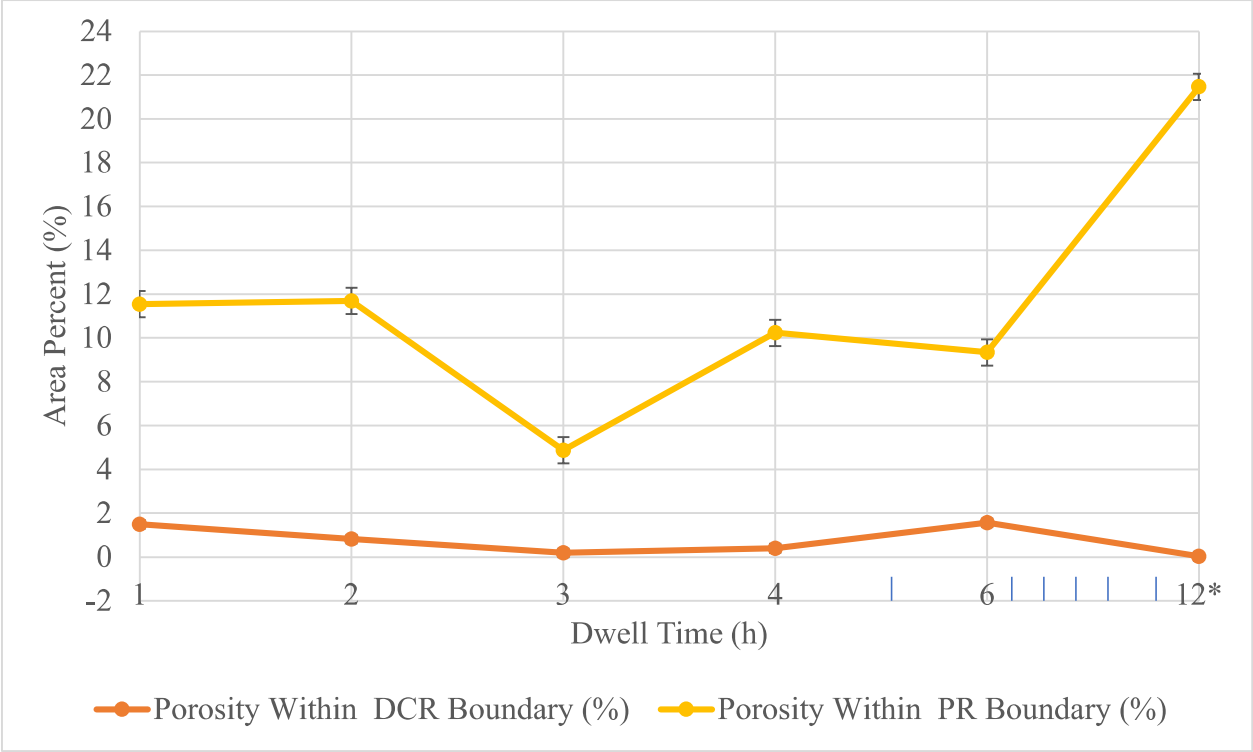

Figure 66: Radial porosity percent relative to region boundary area.

The porosity percent relative to DCR and PR boundaries in the axial cross-sections showed a relative decrease in porosity. The porosity decrease appeared more linear for the DCR with a decrease in porosity from ~4% to ~1%, while the PR had more porosity in the interval of dwell times between 1h and 3 h with a porosity of ~14% to ~16%, then decreasing from 4 h to 6 h, and increasing up to ~14% porosity for 12 h of dwell time.

Porosity percentages within the radial DCR and PR boundaries were less consistent compared to results from the axial boundaries. For these cross-sections, porosity percentages appeared to increase in the PR boundary, with an overall increase from ~12% porosity at 1 h to ~22% at 12 h. This boundary displayed a different behavior compared to that in the axial PR, where in the radial PR porosity percentage decreases from 2 h to 3 h, and then increases at 4 h of sintering dwell time, followed by s small decrease in porosity percentage before increasing to the higher percentage at 12 h. Porosity percentage in the DCR boundary displayed no significant

change, with porosity percentages maintaining values between <1% and ~2% throughout the sintering dwell times.

It was noted that most of the porosity for both cross-sections was along the edges due to the method of tracing and creating the boundaries for each cross-section. Boundaries at the outer edges of the cross-sections were created by connecting the top of a sphere to the top of another nearest sphere, and the space in between was porosity. The porosity percentages relative to the boundaries in both cross-sections varies depending on the size of the boundary, and the size of the boundary is a rough estimation in this study due to the method of defining the boundaries and the complex porosity that some cross-sections displayed where it was difficult to separate the porosity at the DCR from the PR.

5.3 Observations from Process Development

Sintering of unpacked Cu powder pellets was further characterized through the area fraction analysis of axial and radial cross-sections. The porosity and density behavior of these cross-sections was summarized, tabulated and graphed to better illustrate changes as sintering dwell was increased. Further observations were recognized as pellets were initially theorized to densify homogeneously through the sintering temperature profile from 1 h to 12 h, but this was not the case due to a porosity gradient within the pellets. This gradient was examined to analyze how the porous ring on the edges of the cross-sections compared to overall porosity. More consistent results were found in the average porosity values for axial cross-sections in both the porosity behavior and the size of the dense areas in the cross-sections with increasing dwell time.

5.4 Conclusions

The methods and procedures used for this study enabled the achievement analyzing the porosity evolution of unpacked sintered Cu powered pellets through a set of methods. Pellets were produced with the most optimal materials and methods available to begin experiments with a high level of porosity and increase this characteristic through various sintering dwell times at a temperature close to Cu's melting point. Porosity and density were characterized for each pellet through two methods of measurement, and later compared. A third method was incorporated to better analyze the porosity within the pellet samples through area fraction of pellet cross-sections, and this was achieved through ImageJ analysis, leading to the comparison and observation of porosity decrease with increasing sintering dwell time.

Modifications to equipment and materials used would be necessary for further result enhancement in areas such as sintering, pellet slicing, polishing and SEM image capture. A sintering setup could be improved through a more controlled atmosphere with less exposure to the air outside the system, thus further diminishing oxidation of Cu sphere pellets. An automatic temperature setup furnace would also be of interest to assure more temperature precision and less need for user monitoring. Having enough room for multiple pellets to be sintered at the same time and having more than one thermocouple to monitor the temperature gradients in the sintering atmosphere would be advantageous in conducting an experimental mesh of data and more accurate results. Pellet slicing would be enabled through the use of a more precise saw to cut pellet samples at a more specific location. And the SEM image capture would be enhanced through the use of a more updated microscope, taking into account the porous cross-sectional surfaces that would be analyzed, and using a sputter coater that would coat these surfaces more evenly to increase electron reflection and higher image contrast, even in highly porous areas.

In chapter 4 it was assessed that the average change in density of SGD % T.D. as ~59% (1 h dwell time) to ~70% (12 h dwell time), and AIMD % T.D. as ~65% (1 h dwell time) to ~75% (12 h dwell time). Overall trends however, appeared more inconsistent for SGD values compared to AIMD. This was due to the more complex cylindrical shape of the sintered pellets on behalf of the volumetric density gradient happening during the process of sintering. All pellets showed a curved top surface as this surface was the only one not constricted by nearby alumina surfaces. This resulted in an approximate volumetric calculation which did not account for curved surfaces. AIMD measurements only accounted for mass values between the solid Cu and the pores and these measurements proved to be more accurate in determining porosity and density values of the pellets. But this could also be improved with the use of gas pycnometers to increase the precision of porosity in the pellets without having to take three types of mass measurements and handling the liquid substance. This method could also take into account the more complex porosity within the pellet volume, as gases are capable of being inserted in smaller spaces with more ease compared to liquids.

Image analysis results seen in chapter 5 certainly helped see the sintered pellet samples in a more profound manner by observing how the density expanded through the samples with increasing dwell time. While this portion of the study analysis rejected the initial hypothesis that pellets would densify uniformly across the volumetric space, it became evident that analyzing the progressing dense center and porous ring would be of importance for third parties in the future to account for this in computer models. Porosity trends were tabulated and graphed with the average cross-sectional porosity analyzed through a mesh of images on imageJ for each pair of cross-sections as each dwell time. Both trends for the average cross-sectional porosity of axial and radial trends showed a similar decrease in porosity of around ~5% by the end of a 12 h dwell

time. With higher than expected values at 12 h for the axial cross-sectional trend, and also at 6 h for radial cross-sectional trends. Overall porosity values through the analysis of area fraction could be enhanced by analyzing more than one axial and radial cross-section for each sample. This could be time consuming as the pellet dimensions were relatively large compared to the magnification used to capture images, which was already the lower magnification that could be used on these pellets with the SEM. But enhancements could be done by sintering pellets with smaller dimensions. There would however be a limit as to how small the pellets could be taking into consideration the size of spheres. Another factor to take into consideration when altering the pellet overall size or geometry would be the process of densification. It is expected that pellets will continue maintaining a DCR and PR under the conditions applied in this study, while only altering the height or diameter of the pellets. The surrounding containment of the powder in which it is sintered is also theorized to contribute to the porosity gradient in the pellets, and thus a variable to consider for future analysis of this characteristic would be to sinter loose packed Cu spheres in a container made of solid Cu, or other metals with a higher melting point.

It would be of interest to computer modelers to be able to observe the porosity changes in several cross-sections at lower temperatures and longer dwell times to be compared to the rate of densification and porosity changes in this study. With Cu being a single phase non-radioactive metal, and the results of the sintering profile provided in this study, computer modeling can be achieved to pave a path for computations of pellet densification prior to incorporating the more complex properties of U-10Zr.

REFERENCES

[1] “INL develops safer, more efficient nuclear fuel for next-gen reactors.” (2009) Retrieved from https://phys.org/news/2009-11-inl-safer-efficient-nuclear-fuel.html.

[2] "Metals And Alloys." Courses.Chem.Psu.Edu, 2017, http://courses.chem.psu.edu/chem112/materials/metals.html.

[3] "Metals Structure." Depts.Washington.Edu, 2017, https://depts.washington.edu/matseed/mse_resources/Webpage/Metals/metalstructure.htm.

[4] "NRC: Backgrounder On High Burnup Spent Fuel." Nrc.Gov, 2015, http://www.nrc.gov/reading-rm/doc-collections/fact-sheets/bg-high-burnup-spent-fuel.html.

[5] “Primary Metallic Crystalline Structures”. Retrieved from https://www.ndeed.org/Physics/Materials/Structure/metallic_structures.xhtml

[6] "Sintering In The Powder Metallurgy Process." Powder Metallurgy Review, 2017, http://www.pm-review.com/introduction-to-powder-metallurgy/sintering-in-the-powdermetallurgy-process/.

[7] Alekseev, P.N., Bobrov, E.A., Chibinyaev, A.V. et al. Phys. Atom. Nuclei (2015) 78: 1264. https://doi.org/10.1134/S1063778815110034.

[8] Alexander, B., & Balluffi, R. (1957). The mechanism of sintering of copper. Acta Metallurgica, 5(11), 666-677. doi: 10.1016/0001-6160(57)90113-x.

[9] Al-Qureshi, H.A. et al. "Analyses Of The Fundamental Parameters Of Cold Die Compaction Of Powder Metallurgy." Journal Of Materials Processing Technology, vol 199, no. 1-3, 2008, pp. 417-424. Elsevier BV, doi:10.1016/j.jmatprotec.2007.08.030.

[10] Al-Qureshi, H.A. et al. "On The Mechanics Of Cold Die Compaction For Powder Metallurgy." Journal Of Materials Processing Technology, vol 166, no. 1, 2005, pp. 135143. Elsevier BV, doi:10.1016/j.jmatprotec.2004.08.009.

[11] Berry, Bruce, "Numerical Simulation of Metallic Uranium Sintering" (2017). Theses and Dissertations. 1904. http://scholarworks.uark.edu/etd/1904.

[12] Briscoe, B.J., and S.L. Rough. "The Effects Of Wall Friction In Powder Compaction." Colloids And Surfaces A: Physicochemical And Engineering Aspects, vol 137, no. 1-3, 1998, pp. 103-116. Elsevier BV, doi:10.1016/s0927-7757(97)00210-0.

[13] Callister, W. D., & Rethwisch, D. G. (2008). Fundamentals of materials science and engineering: An integrated approach. Hoboken, NJ: John Wiley & Sons.

[14] Chen, Xiaolin. "Particle Packing, Compaction And Sintering In Powder Metallurgy." University Of Alberta, Department Of Chemical And Materials Engineering, 1998.

[15] F. Wakai, M. Yoshida, Y. Shinoda, and T. Akatsu, “Coarsening and grain growth in sintering of two particles of different sizes,” Acta Materialia, vol. 53, no. 5, pp. 1361–1371, 2005

[16] Fedors, R.F., and R.F. Landel. "An Empirical Method Of Estimating The Void Fraction In Mixtures Of Uniform Particles Of Different Size." Powder Technology, vol 23, no. 2, 1979, pp. 225-231. Elsevier BV, doi:10.1016/0032-5910(79)87011-4.

[17] German, R. (1994). Powder metallurgy science. Princeton, NJ: Metal Powder Industries Fed.

[18] German, R. M. "Prediction Of Sintered Density For Bimodal Powder Mixtures." Metallurgical Transactions A, vol 23, no. 5, 1992, pp. 1455-1465. Springer Nature, doi:10.1007/bf02647329.

[19] German, R. M. (1996). Sintering theory and practice. New York: John Wiley & Sons.

[20] Hart, Clifford S., and S. M. McDeavitt. A Study of the Morphology of Porosity in Sintered Uranium-zirconium Alloys as a Function of Sintering Time. MS Thesis. Texas A&M University. 2019.

[21] Hofmann, H., & Bowen, P. Powder Technology, Part II: Compaction. Retrieved from https://ltp.epfl.ch/files/content/sites/ltp/files/shared/Teaching/Master/06PowderTechnology/Compaction.pdf.

[22] IAEA (International Atomic Energy Agency). “Impact of High Burnup Uranium Oxide and Mixed Uranium– Plutonium Oxide Water Reactor Fuel on Spent Fuel Management”. https://www-pub.iaea.org/MTCD/Publications/PDF/Pub1490_web.pdf.

[23] Kang, S.J. (2005). Sintering: Densification, Grain Growth & Microstructure. Elsevier Butterworth-Heinemann, ISBN 9780750663854, Oxford, U.K. 255 pages.

[24] Lame, O., Bellet, D., Di Michiel, M & Bouvard, D. (2003). In situ microtography investigation of metal powder compacts during sintering. Nuclear Instruments and Methods in Physics Research B, Vol.200, (January 2003), pp287-294, ISSN 0168-583X.

[25] M.A. Chowdhury, D.M. Nuruzzamana , A.H. Miaa , M.L. Rahaman,"Friction Coefficient Of Different Material Pairs Under Different Normal Loads And Sliding Velocities." Tribology In Industry, vol 34, no. 1, 2012, pp. 18-23. http://www.tribology.fink.rs/journals/2012/2012-1/3.pdf.

[26] Manzel, R, and C.T Walker. "EPMA And SEM Of Fuel Samples From PWR Rods With An Average Burn-Up Of Around 100 Mwd/Kghm." Journal Of Nuclear Materials, vol 301, no. 2-3, 2002, pp. 170-182. Elsevier BV, doi:10.1016/s0022-3115(01)00753-x.

[27] Mathews, Christopher. "Fission Gas Bubble Behavior In Uranium Carbide." Oregon State University, 2015.

[28] McDeavitt, Sean, Shao, Lin, Tsvetkov, Pavel, Wirth, Brian, & Kennedy, Rory (Apr

2014). Fuel Performance Experiments and Modeling: Fission Gas Bubble Nucleation and Growth in Alloy Nuclear Fuels (DOE/NEUP--09-816). United States

[29] Nor, S.S.M. et al. "The Effect Of Lubrication In Reducing Net Friction In Warm Powder Compaction Process." Journal Of Materials Processing Technology, vol 207, no. 1-3, 2008, pp. 118-124. Elsevier BV, doi:10.1016/j.jmatprotec.2007.12.081.

[30] P. Moore, B. Beeler, C. Deo, M. I. Baskes, M. A. Okuniewski, "Structure And Properties Of An Aluminium-Lithium-Manganese-Zirconium Alloy For High Temperature Applications." Metal Powder Report, vol 47, no. 6, 1992, p. 49. Elsevier BV, doi:10.1016/0026-0657(92)91426-k.

[31] Selig, Stanley G., and Darrel A. Doman. "A Review Of Finite Element Simulations Of Metal Powder Die Compaction." Journal Of Machinery Manufacturing And Automation, vol 3, no. 2, 2014, pp. 32-40.

[32] University of Cambridge Dissemination of IT for the Promotion of Materials Science. (n.d.). Copper in Motors. Retrieved October 15, 2021, from https://www.doitpoms.ac.uk/tlplib/recycling-metals/copper_motors.php.

APPENDIX A

Alfa Aesar

Certificate of analysis

Product No.:	42623
Product:	Copper powder, spherical, -100+325 mesh, 99.9% (metals basis)
Lot No.:	Z06E014

Ag	< 20	Al	< 20	C	40
Fe	20	Ni	< 20	O_2	4950
Pb	< 20	Si	40	Sn	< 20
Zn	< 20				

Values given in ppm unless otherwise noted

This document has been electronically generated and does not require a signature.

Order our products online **www.alfa.com**

ThermoFisher SCIENTIFIC

APPENDIX B

Alfa Aesar

Certificate of analysis

Product No.:	42623
Product:	Copper powder, spherical, -100+325 mesh, 99.9% (metals basis)
Lot No.:	T06D091

Ag	< 20	Al	< 20	C	20
Fe	< 20	Ni	< 20	O_2	3457
Pb	< 20	Si	20	Sn	< 20
Zn	< 20				

Values given in ppm unless otherwise noted

This document has been electronically generated and does not require a signature.

Order our products online **www.alfa.com**

ThermoFisher SCIENTIFIC